TECHNICKÁ UNIVERZITA V LIBERCI
Fakulta mechatroniky, informatiky
a mezioborových studií

ADVANCED TIME AVERAGE DIGITAL HOLOGRAPHY BY MEANS OF FREQUENCY AND PHASE MODULATION

PhD dissertation

Study program: P3901 Applied Sciences Engineering
Field of study: 3901V055 Applied Sciences Engineering

Author: **Ing. Pavel Psota**
Supervisor: prof. Ing. Václav Kopecký, CSc.
Tutor: Ing. Vít Lédl, Ph.D.

Liberec 2015

Declaration

I hereby certify that I have been informed the Act 121/2000, the Copyright Act of the Czech Republic, namely § 60 - Schoolwork, applies to my PhD dissertation in full scope.

I acknowledge that the Technical University of Liberec (TUL) does not infringe my copyrights by using my PhD dissertation for TUL's internal purposes.

I am aware of my obligation to inform TUL on having used or licensed to use my PhD dissertation; in such a case TUL may require compensation of costs spent on creating the work at up to their actual amount.

I have written my PhD dissertation myself using literature listed therein and consulting it with my dissertation supervisor and my tutor.

Concurrently I confirm that the printed version of my PhD dissertation is coincident with an electronic version, inserted into the IS STAG.

Date:

Signature:

Acknowledgement

I want to thank prof. Ing. Václav Kopecký, CSc. for supervising my work and for building a productive and stimulating environment that is always indispensable for progress. I am very grateful to Ing. Vít Lédl, Ph.D. I sincerely appreciate all his visions, ideas and discussions contributing to my scientific as well as personal growth. I thank all my close colleagues in laboratory. Such a group of various personalities has been a constant source of good advice, collaboration and mainly friendship and fun. Last but not least I would like to thank my recently increased family for a great support, infinite patience and daily recharging of my energy.

Annotation

This dissertation introduces some developments in the field of time average digital holography widely using as a tool for vibration analysis. The work deals with the most significant drawbacks of the method: limited measurement range and quantitative analysis of the measured Bessel fringe patterns. Different frequency modulation of an object wave and a reference wave in experimental arrangements results in temporally harmonic variation of intensity values of a digital hologram. This feature expresses a relative phase difference between the both waves and therefore any of phase-shifting algorithms can be applied in order to directly calculate a complex field in the hologram plane. This leads on the one hand to improvement of lateral resolution within the reconstructed surface of the object. On the other hand the signal-to-noise ratio is increased. When frequency of the reference wave is in addition modulated by an integer multiple of frequency at which the object oscillates, the measurement range of the method can be shifted either to smaller or to larger vibration amplitudes. The threshold of the smallest measurable amplitude is experimentally established to be under 0.1 nm while the largest measured amplitude is about 10 μm. Phase modulation of the reference wave is used to obtain a sequence of phase modulated fringe patterns (reconstructed fields). Such fringe patterns can be combined by means of phase shifting algorithms and amplitudes of vibrations can be straightforwardly computed. This approach calculates the amplitude values independently in every single pixel. The both frequency and phase modulation are realized by proper control of Bragg cells.

Keywords: Vibration analysis, digital holography, time average holography, frequency modulation, phase modulation, very small amplitudes, vibration amplitude distribution.

Anotace

Tato práce rozvijí digitálně holografickou metodu časového středování, která patří mezi důležité nástroje v oblasti analýzy vibrací. Vývoj se zaměřuje na největší slabiny této metody, které jsou její omezený měřicí rozsah a kvantifikace amplitud vibrací z rekonstruovaných polí. Rozdílná frekvenční modulace referenční a objektové vlny holografického uspořádání způsobuje harmonicky se vyvíjející interferenční pole digitálního hologramu. Tato časová proměnnost je určena relativní fázovou změnou mezi oběma vlnami. Toho lze využít pro přímý výpočet komplexního pole v rovině hologramu pomocí některého z rodiny „phase-shifting“ algoritmů. Výsledkem je dosažení lepšího prostorového rozlišení uvnitř měřené oblasti a zvýšení poměru signál-šum. Je-li dále referenční vlna modulována frekvencí odpovídající násobku frekvence měřeného objektu, lze posouvat měřicí rozsah metody do hodnot velmi malých i velkých amplitud vibrací. Prahová hodnota měřitelnosti pro malé amplitudy vibrací byla experimentálně stanovena pod 0.1 nm. Na druhé straně lze metodu modifikovat i pro měření amplitud vibrací kolem cca 10 µm. Kromě frekvenční modulace je možné do metody zakomponovat i modulaci fáze jedné z vln holografického uspořádání. Tímto způsobem získáme sekvenci fázově posunutých interferenčních struktur, které lze opět pomocí „phase-shifting“ algoritmů využít pro výpočet rozložení amplitud vibrací nezávisle v každém bodě povrchu. Frekvenční i fázová modulace je realizována pomocí Braggových cel.

Klíčová slova: Analýza vibrací, digitální holografie, holografie časového středování, frekvenční modulace, fázová modulace, velmi malé amplitudy vibrací, rozložení amplitud vibrací.

Contents

Introduction

Measurement of vibrations is an integral task to engineering [1]. Vibration analysis is on the one hand used to ascertain operation of a vast spectrum of components, which should oscillate, like loudspeakers, ultrasonic or piezoelectric transducers, etc., and on the other hand to check the behavior of components, which have natural frequencies within the range of operating frequencies. This helps to prevent the components of fatigue failure or to detect their noise-generating parts or areas. Obviously, contactless measurement methods which do not affect the vibrations itself are demanded. In many practical cases, the knowledge of vibration amplitudes in a single point of the surface is not sufficient but a distribution of amplitudes over the whole surface can only provide the complete information.

On the market, there is a broad portfolio of vibration measurement devices, which are usually based on the Doppler phenomenon [2]–[5], correlation analysis [2], speckle ESPI (Electronic Speckle Pattern Interferometry) [3], [4], and others. These methods are mostly single-point methods or their measuring capabilities in terms of maximal vibration amplitudes or frequency range are limited. Thus, a great attention must be paid to parameters of a device when choosing one for a certain application. Another suitable tool for analyzing vibrations in the whole surface is holographic interferometry, which has no limit in vibration frequency. Holographic interferometry is comprising of two basic principles: holography and interferometry.

In 1948 Gabor discovered holography as a lensless process for image formation by reconstructed wavefronts [5]. The breakthrough of holography was initiated by the development of the laser providing a powerful source of coherent light at the beginning of 60s. The drawback of Gabor's inline arrangement related to twin image was addressed by the off-axis technique introduced by Leith and Upatnieks [6]. Denisyuk combined the ideas of Gabor and Lippmann, which led to the invention of the thick reflection hologram [7]. At the end of 60s there was a working method for recording and reconstruction of complete wave fields. Besides the impressive display of three-dimensional scenes exhibiting effects like depth and parallax, holography found many applications in the field of synthetic holograms [8]–[10] or holographic data storage [11]. Perhaps the most important application of holography is a measurement technique called holographic interferometry [12], [13]. The early applications ranged from the first measurement of vibration modes [12], [13], over deformation measurement [14],

[15], contour measurement[16], [17], to the determination of refractive index changes [18]–[20].

The wet chemical processing of the holographic recording media showed their inherent drawbacks. The first attempt to capture a hologram by a digital sensor dates back in 1967 when Goodman and Lawrence [21] recorded a wave field with use of a vidicon. The output of the vidicon was sampled in a 256×256 array, and quantized to eight grey levels. This was the very beginning of digital holography. Since this date, digital holography has been developing [22], although its boom came with the wide spread discovery of modern cameras using CCD or CMOS. Recording and numerical reconstruction of digital holograms were introduced by Schnars and Jueptner [23]. The most significant impact of digital holography I find in the branch of digital holographic interferometry (DHI) [24]–[26] and digital holographic microscopy (DHM) [27]–[30].

This dissertation is aimed to a development of the holographic method in the field of vibration analysis. The pioneering work in this manner was done by Powell and Stetson [12], [13] in 1965. They shew, that the image of holographically recorded oscillating object exhibits a system of interference fringes, which map contours of constant vibration amplitude. The method was named time average holographic interferometry (TAHI), which, in this basic configuration, is suitable for measurement of vibration amplitudes starting from hundreds of nanometers up to few microns. In 1967 Goodman [31] and Aleksoff [32] took the first step in extension of time average holographic interferometry measurement range by means of frequency modulation (FM). The detectable smallest amplitude with frequency modulated TAHI (FMTAHI) was estimated in 1976 by Ueda et al. [33] to be $2.7 \times 10^{-4}\,\lambda$.

Similarly to holography itself, TAHI has significantly changed after arrival of the digital era. Picard et al. [34] performed time averaged holography with a digital CCD camera. That was the beginning of using time average digital holography (TADH). Heterodyne technique realized by acusto-optical modulators was introduced by Clerc et al. [35]. Further, Joud et al. [36] employed acusto-optical modulators in TADH for large amplitudes measurement while Psota et al. [37] applied frequency modulation by means of Bragg cells for measurement of very small amplitudes. Later on the method with ultimate sensitivity was experimentally verified by Lédl et al. [38]. Other configurations with great sensitivity was presented by Verrier [39].

One of the most important tasks in time-average holography (TAHI or TADH) is to quantitatively determine the amplitude distribution from the fringe pattern modulated by Bessel function. Numerical analysis of cosine fringes (exhibiting in other interferometric techniques) allows for the determination of interference phases even between the fringe intensity maxima and minima with high accuracy. A lot effort has been put to automate the evaluation of cosine fringes coming from holographic interferometry, but not a great work has been done to automate Bessel fringe patterns resulting from the time average technique. The interference phase (directly connected to the required amplitude of vibration) is most often determined by searching for intensity maxima and minima followed by manual fringe counting and interpolation of values between the fringes. Nevertheless, modern digital cameras provide the advantage of very uniform and repeatable response, and they can be considered as radiometric detectors. This can be exploited for a normalization of the reconstructed intensity if two digital holograms (one in vibrating and one in steady state) are captured. The normalized intensity field can be directly inverted to the vibration amplitude distribution since the relation between intensity and amplitude is known. The direct inversion approach was applied by Borzsa [40] and Psota et al. in [37]. However, due to not monotonous behavior of the Bessel function, the procedure cannot still be fully automatic. Vikram [41] and Psota et al. [42] have also used recurrence relation of the Bessel function in order to calculate an amplitude distribution from intensity distributions modulated by different orders of Bessel function. A least square solution of overdetermined systems consisting of differently modulated intensity maps was proposed by Psota et al. in [43]. However, none of the method is simultaneously full-field, robust, accurate and fully automated.

Stetson and Brohinski [44] placed a PZT mirror in the reference arm of a holographic arrangements in order to alter its phase and shift the Bessel fringes. This inspired Psota et al. [45] to use Bragg cells in experimental arrangements in for modulation of the both phase and frequency of the reference wave. This invention resulted in the method with quantitative measurement of amplitudes of vibrations independently in every single pixel in the extended dynamic range. This method simultaneously addresses two main drawbacks of TADH:

- Extension of the measurement range;
- User friendly, fully automated and quick retrieval of amplitudes independently in every single pixel;

without excessive hardware demands. Moreover, together with complete automatic control and data processing, the method introduces a complete solution for full-field, contactless vibration analysis with unique accuracy and lateral resolution.

This dissertation describes the physical nature of the method, experimentally verifies the theoretical claims, searches for limits of the method, discusses possible sources of distortions and quantifies them. Last but not least introduces some results of applied engineering tasks like piezoelectric transformer vibration modes visualization [37], [46]–[50] or measurement of a glass shell in the noise suppression experiment [51]–[55].

The dissertation is organized into four main chapters. The first two chapters can be summed up as a theoretical part, where some basic and generally-known principles are defined for subsequent use in the text. The last two chapters describe author´s selected contributions in the field of TADH.

Chapter 1 presents the physical prerequisites of digital holography, starting with the wave theory of light, describing effects such as interference, polarization, coherence and diffraction.

Chapter 2 presents the techniques of how to record holograms on a digital sensor. In other words it shows how to solve the problem imposed by the limited resolution of these detectors. Then the chapter introduces the reconstruction of the recorded optical wave field by the numerical reconstruction. Finally, the basic principle of vibration analysis by TADH is introduced.

In Chapter 3 the advantages resulting from Bragg cells employment are described and experimentally verified. Namely it is lateral resolution and signal to noise ratio (SNR) improvement, extension of dynamic range and retrieval of vibration amplitudes. Moreover, error and uncertainty analysis is performed.

Chapter 4 is devoted to experimental results of the developed method. Particularly it is mode visualization of ring and disc piezoelectric transformers and measurement of amplitudes of vibration generated by a glass shell within a noise suppression experimental study.

Motivation

This dissertation presents a novel approach in the field of time average digital holography. The research group (whose member is also the author) working in Laboratory of Optical Metrology (LOM) at the Technical University of Liberec (TUL) have been dealing with holography or digital holography for more than 10 years. During the master study program the author wrote algorithms for processing of digital holograms like numerical reconstruction of digital holograms, phase filtering or measurand retrieval especially for deformation measurement. He was the leader in establishment digital holography as a standard tool in LOM. The research and development course in LOM is usually initiated by demands of external research groups either from academic or industry sphere. A vast spectrum of various measurement techniques for many diverse quantities (vibrations, deformation, displacement, shape, refractive index, temperature, holographic PIV (Particle Image Velocimetry), DHM (Digital Holographic Microscopy), etc.) has been developed. This was also the reason why researches of LOM put an effort to study methods of vibration analysis. The first demand was to measure amplitudes of vibration of oscillating piezoelectric transformers in their whole surface. It is known, that the vibration amplitudes in this case are very small and therefore cannot be measured by common TADH or TAHI. It was therefore necessary to develop a new method, which is sensitive even for very small vibration amplitudes. The method was based on frequency modulation of reference wave by means of Bragg cells. Disadvantage of the developed method was its upper limit (approximately 80 nm) of measurable amplitudes due to presence of ambiguities in the reconstructed intensity field for larger vibration amplitudes. This drawback became evident in another measurement challenge, which was measurement of a glass shell in a study of acoustic noise suppression by active control. Apparently the better suppression of noise requires larger measurement range of the method when comparing the both states: with and without suppression. The amplitude of vibration can differ about more than four orders. Since it was also required to measure and process a big amount of data (measured at different frequencies and at different settings of the active circuit for the noise suppression) it was unavoidable to come up with new, automatic and quick data processing technique. There had been no available solution fulfilling the criteria and therefore author (based on previous developments of other teams) started the uneasy task of even a better method development.

1 Theory behind Digital Holography

1.1 Wave equation

In the nineteenth century Maxwell showed that light was an electromagnetic (EM) wave and all forms of electromagnetic radiations are governed by the same laws of electromagnetics. Electromagnetic radiation propagates in the form of waves consisting of two related vector fields: namely the electric field $\boldsymbol{E}(\boldsymbol{r},t)$ and the magnetic field $\boldsymbol{H}(\boldsymbol{r},t)$, that are the functions of position $\boldsymbol{r}$ and time t. Therefore, in order to generally describe light propagation in a medium, whether free space or a material, it is in general necessary to know six scalar functions. These functions are not completely independent since the vectors of electric and magnetic fields must satisfy a set of coupled equations known as Maxwell´s equations [56], [57]. Maxwell´s equations could have different forms, for the purpose:

$$\nabla \times \boldsymbol{H} = \varepsilon_0 \frac{\partial \boldsymbol{E}}{\partial t}, \tag{1.1}$$

$$\nabla \times \boldsymbol{E} = -\mu_0 \frac{\partial \boldsymbol{H}}{\partial t}, \tag{1.2}$$

$$\nabla . \boldsymbol{E} = 0, \tag{1.3}$$

$$\nabla . \boldsymbol{H} = 0, \tag{1.4}$$

describe electromagnetic field in free space. In (1.1)-(1.4), $(\nabla \times)$ holds for an operator of curl, $(\nabla .)$ is an operator of divergence, $\boldsymbol{E},\boldsymbol{H}$ are vectors of intensity of electric resp. magnetic field, $\mu_0 = 4\pi \times 10^{-7} Hm^{-1}$ is a free space permeability and finally $\varepsilon_0 = 8{,}85 \times 10^{-12} Fm^{-1}$ is a free space permittivity.

Since an electromagnetic field tends to polarize any medium it permeates, producing an instantaneous distribution of electric and magnetic dipoles, for the description of the electromagnetic field in a material medium it is necessary to define two additional vector fields: the electric flux $\boldsymbol{D}$, magnetic flux $\boldsymbol{B}$, respectively. The relation between the electric flux $\boldsymbol{D}$ and the electric field $\boldsymbol{E}$ depends on electric properties of the medium. Similarly, the relation between the magnetic flux $\boldsymbol{B}$ and the magnetic field $\boldsymbol{H}$ depends on magnetic properties of the medium. Constitutive relations

$$\boldsymbol{D} = \varepsilon_0 \boldsymbol{E} + \boldsymbol{P}, \tag{1.5}$$

$$\boldsymbol{B} = \mu_0 \boldsymbol{H} + \boldsymbol{M} \tag{1.6}$$

define these relations in which $\boldsymbol{P}$ is the polarization density and $\boldsymbol{M}$ is the magnetization density. Maxwell's equations in a medium (no free electric charges or currents), involving vector fields $\boldsymbol{E}, \boldsymbol{H}, \boldsymbol{D}, \boldsymbol{B}$, are expressed as

$$\nabla \times \boldsymbol{H} = \varepsilon_0 \frac{\partial \boldsymbol{D}}{\partial t}, \tag{1.7}$$

$$\nabla \times \boldsymbol{E} = -\mu_0 \frac{\partial \boldsymbol{B}}{\partial t}, \tag{1.8}$$

$$\nabla . \boldsymbol{D} = 0, \tag{1.9}$$

$$\nabla . \boldsymbol{B} = 0. \tag{1.10}$$

The nature of the dielectric medium is exhibited by so called medium equation defining the relation between the polarization density $\boldsymbol{P}$ and the electric field $\boldsymbol{E}$. The medium equation defines properties of the medium e.g. linearity, dispersivity, homogeneity or isotropy. Within the scope of this work one can restrict to a light propagating in free space where $\boldsymbol{P} = \boldsymbol{M} = \boldsymbol{0}$ and therefore relations (1.1)-(1.4) are recovered.

Using vector identity $\nabla \times (\nabla \times \boldsymbol{E}) = \nabla . (\nabla . \boldsymbol{E}) - \nabla^2 \boldsymbol{E}$ and the Maxwell´s equations (1.1)-(1.4) one can derive wave equations:

$$\nabla^2 \boldsymbol{E}(\boldsymbol{r}, t) - \frac{1}{c^2} \frac{\partial^2 \boldsymbol{E}(\boldsymbol{r}, \boldsymbol{t})}{\partial t^2} = 0, \tag{1.11}$$

$$\nabla^2 \boldsymbol{H}(\boldsymbol{r}, t) - \frac{1}{c^2} \frac{\partial^2 \boldsymbol{H}(\boldsymbol{r}, t)}{\partial t^2} = 0, \tag{1.12}$$

where $c = \sqrt{\frac{1}{\mu_0 \varepsilon_0}} = 299\,792\,458\, ms^{-1}$ is the speed of light and $\nabla^2 = \frac{\partial^2}{\partial x^2} + \frac{\partial^2}{\partial y^2} + \frac{\partial^2}{\partial z^2}$ is the Laplace operator. Although we have obtained a wave equation for the electric field $\boldsymbol{E}$ and another for the magnetic field $\boldsymbol{H}$, the solution of both equations are not independent, because the electric and magnetic fields are related through Maxwell's equations. Therefore each of these two vectorial wave equations can be separated on three scalar wave equations, expressed as:

$$\nabla^2 u(\boldsymbol{r},t) - \frac{1}{c^2}\frac{\partial^2 u(\boldsymbol{r},t)}{\partial t^2} = 0, \qquad (1.13)$$

where the scalar variable $u(\boldsymbol{r},t)$ may represent each of the six Cartesian components of either the electric or magnetic fields.

Obviously, the EM waves transport energy. The Poynting vector $\boldsymbol{S}$:

$$\boldsymbol{S} = \boldsymbol{E} \times \boldsymbol{H} \qquad (1.14)$$

defines the flux of energy carried by the EM wave. The intensity I of the EM wave is then defined as the amount of energy passing through the unit area per time. Mathematically the intensity is defined as the Poynting vector modulus averaged over time:

$$I = \langle |\boldsymbol{S}| \rangle. \qquad (1.15)$$

The fact of using an averaged value instead of an instant value to define the intensity of an EM wave is because no detector is able to follow fast changes of intensity due to the very high frequency of light.

1.2 Monochromatic waves

The time dependence of $\boldsymbol{E}$ and $\boldsymbol{H}$ within the wave equations (1.11), (1.12) evinces very often the harmonic variation. Then harmonic functions are considered as a solution of the wave equation. All components of the electric and magnetic fields are harmonic functions of time of the same angular frequency ω. In a general form, the electric and magnetic fields associated with a monochromatic wave can be expressed as:

$$\boldsymbol{E}(\boldsymbol{r},t) = \boldsymbol{E_0}(\boldsymbol{r})cos(\omega t + \varphi(\boldsymbol{r})), \qquad (1.16)$$

$$\boldsymbol{H}(\boldsymbol{r},t) = \boldsymbol{H_0}(\boldsymbol{r})cos(\omega t + \varphi(\boldsymbol{r})), \qquad (1.17)$$

where the amplitudes of fields $\boldsymbol{E_0}(\boldsymbol{r})$ and $\boldsymbol{H_0}(\boldsymbol{r})$ as well as the initial phase $\varphi(\boldsymbol{r})$ depend on the position $\boldsymbol{r}$, but the time dependence is carried out only in the cosine argument through ωt. When dealing with monochromatic waves, it is usually easier to write down the monochromatic fields using complex notation[1] ($j = \sqrt{-1}$):

[1] Complex numbers are denoted by a dot above a letter.

$$\boldsymbol{E}(\boldsymbol{r},t) = Re\{\dot{\boldsymbol{E}}(\boldsymbol{r})exp(j\omega t)\}, \tag{1.18}$$

$$\boldsymbol{H}(\boldsymbol{r},t) = Re\{\dot{\boldsymbol{H}}(\boldsymbol{r})exp(j\omega t)\}, \tag{1.19}$$

where $\dot{\boldsymbol{E}}(\boldsymbol{r})$ and $\dot{\boldsymbol{H}}(\boldsymbol{r})$ denote the complex amplitudes of the electric and magnetic fields, respectively. The angular frequency ω that characterizes the monochromatic wave is related to the frequency f and the period T by:

$$\omega = 2\pi f = \frac{2\pi}{T}. \tag{1.20}$$

In the case of monochromatic waves, Maxwell's equations (1.1)-(1.4) (using the complex fields amplitudes $\dot{\boldsymbol{E}}$ and $\dot{\boldsymbol{H}}$) are simplified by substituting $d/dt = j\omega$:

$$\nabla \times \dot{\boldsymbol{H}} = j\varepsilon_0\omega\dot{\boldsymbol{E}}, \tag{1.21}$$

$$\nabla \times \dot{\boldsymbol{E}} = -j\mu_0\omega\dot{\boldsymbol{H}}, \tag{1.22}$$

$$\nabla.\dot{\boldsymbol{E}} = 0, \tag{1.23}$$

$$\nabla.\dot{\boldsymbol{H}} = 0, \tag{1.24}$$

Now, if we substitute the monochromatic waves (1.18) and (1.19) in the wave equation (1.13), we obtain a new wave equation valid only for monochromatic waves known as the Helmholtz equation:

$$\nabla^2 U(\boldsymbol{r}) + k^2 U(\boldsymbol{r}) = 0, \tag{1.25}$$

Function $U(\boldsymbol{r})$ represents each of the six Cartesian components of the $\dot{\boldsymbol{E}}(\boldsymbol{r})$ and $\dot{\boldsymbol{H}}(\boldsymbol{r})$ vectors in (1.18) and (1.19), and wavenumber $k = \omega/c$.

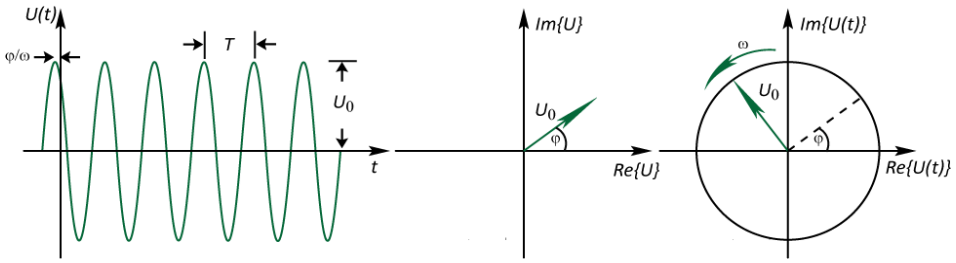

Figure 1.1: Representations of a monochromatic wave at a fixed position r: (left) the wave function $U(t)$ is a harmonic function of time; (middle) the complex amplitude $U(r)$ is a fixed phasor; (right) the complex wave function $U(t)$ is a phasor rotating with angular velocity ω.

The average of the Poynting vector as a function of the complex fields amplitudes for monochromatic waves takes the form:

$$\langle \boldsymbol{S} \rangle = \langle Re\{\dot{\boldsymbol{E}}(\boldsymbol{r})exp(j\omega t)\} \times Re\{\dot{\boldsymbol{H}}(\boldsymbol{r})exp(j\omega t)\}\rangle = Re\{\dot{\boldsymbol{S}}\}, \qquad (1.26)$$

where $\dot{\boldsymbol{S}}$, called the complex Poynting vector, has been defined as:

$$\dot{\boldsymbol{S}} = \frac{1}{2}\dot{\boldsymbol{E}} \times \dot{\boldsymbol{H}}^*, \qquad (1.27)$$

In this way, the intensity carried by a monochromatic EM wave should be expressed as:

$$I = \left|Re\{\dot{\boldsymbol{S}}\}\right| \qquad (1.28)$$

1.3 Monochromatic plane waves

The temporal dependence of EM fields has already been established in terms of monochromatic waves. The solution for the spatial dependence, determined by the complex amplitudes $\dot{\boldsymbol{E}}(\boldsymbol{r})$ and $\dot{\boldsymbol{H}}(\boldsymbol{r})$, can be obtained by solving the Helmholtz equation (1.25). One of the easiest solutions for this equation, and also the most frequently used solution in optics, is a plane wave. The plane wave is characterized by its wavevector $\boldsymbol{k}$, and the mathematical expressions for the complex amplitudes are:

$$\dot{\boldsymbol{E}}(\boldsymbol{r}) = \boldsymbol{E_0}exp(-j\boldsymbol{kr}), \qquad (1.29)$$

$$\dot{\boldsymbol{H}}(\boldsymbol{r}) = \boldsymbol{H_0}exp(-j\boldsymbol{kr}), \qquad (1.30)$$

where the magnitudes $\boldsymbol{E_0}$ and $\boldsymbol{H_0}$ are now constant vectors. Each of the Cartesian components of the complex amplitudes $\dot{\boldsymbol{E}}(\boldsymbol{r})$ and $\dot{\boldsymbol{H}}(\boldsymbol{r})$ will satisfy the Helmholtz equation.

Obviously, the solution given by the electric and magnetic complex amplitudes (1.29), (1.30) must satisfy Maxwell's equations. After substitution of the complex amplitudes (1.29), (1.30) to Maxwell´s equations (1.21), (1.22), the following relations are obtained:

$$\boldsymbol{k} \times \boldsymbol{H_0} = -\omega\varepsilon_0\boldsymbol{E_0}, \qquad (1.31)$$

$$\boldsymbol{k} \times \boldsymbol{E_0} = \omega \mu_0 \boldsymbol{H_0}. \qquad (1.32)$$

These two formulae are valid only for plane monochromatic waves and establish the relationship between the electric field $\boldsymbol{E}$, the magnetic field $\boldsymbol{H}$ and the wavevector $\mathbf{k}$. From equation (1.31) it is obvious that the electric field is perpendicular to the magnetic field and the wavevector. In the same way, the relation (1.32) establishes that the magnetic field $\boldsymbol{H}$ is perpendicular to $\boldsymbol{E}$ and $\mathbf{k}$. Therefore, one can conclude that $\boldsymbol{k}$, $\boldsymbol{E}$ and $\boldsymbol{H}$ are mutually orthogonal, and because $\boldsymbol{E}$ and $\boldsymbol{H}$ lie on a plane normal to the propagation direction defined by $\boldsymbol{k}$, such wave in called a transverse EM wave.

When dealing with monochromatic plane EM waves, it is useful to characterize it by its radiation wavelength λ, defined as a distance between two nearest points with equal phase of vibration. The wavelength is therefore expressed by:

$$\lambda = cT = \frac{c}{f} = \frac{2\pi}{k}. \qquad (1.33)$$

Visible light (VIS) is then an EM wave of such a wavelength that is visible to the human eye. VIS is short interval of the vast electromagnetic spectrum, see Figure 1.2.

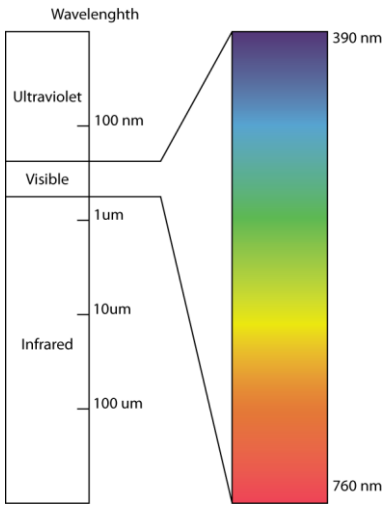

Figure 1.2: Electromagnetic spectrum with highlighted interval of visible wavelengths and its corresponding colors.

When an EM wave passes from one medium to another its frequency remains unchanged, but its phase velocity is modified due to its dependence on the refractive index. The wavelength associated with the EM wave is usually referred to the wavelength of that radiation propagating through free space.

1.4 Polarization of electromagnetic waves

A property associated with a transversal wave is its polarization that is related to the closed curve described by the tip of the electric (or magnetic) field vector at a fixed point $r = r_0$ in the space.

In order to analyze the polarization character of an EM plane wave, let us assume (without loss of generality) that the EM wave propagates along the z-axis. In this case we have:

$$\boldsymbol{k} = k\boldsymbol{e_3}, \tag{1.34}$$

where $\boldsymbol{e_1}, \boldsymbol{e_2}, \boldsymbol{e_3}$ are the unit vectors along the x, y and z-axis respectively. For simplicity one can also consider an electric field varying along the x-axis:

$$\boldsymbol{E} = E_0 cos(\omega t - kz)\boldsymbol{e_1}, \tag{1.35}$$

$$\boldsymbol{H} = H_0 cos(\omega t - kz)\boldsymbol{e_2}. \tag{1.36}$$

The wave described by equations (1.35) and (1.36) is linearly polarized (or more specifically, linearly x-polarized) because the electric field vector $\boldsymbol{E}$ is always along one direction (x direction in this case).

Let consider now a linearly y-polarized wave with an addition phase of $+\pi/2$ described by:

$$\boldsymbol{E} = E_0 cos\left(\omega t - kz + \frac{\pi}{2}\right)\boldsymbol{e_2} = E_0 sin(\omega t - kz)\boldsymbol{e_2}, \tag{1.37}$$

$$\boldsymbol{H} = H_0 cos\left(\omega t - kz + \frac{\pi}{2}\right)\boldsymbol{e_1} = H_0 sin(\omega t - kz)\boldsymbol{e_1}. \tag{1.38}$$

Since Maxwell's equations are linear, a linear combination of several solutions will also be a solution. In particular, the sum of plane waves described in (1.35) and (1.36) and those described by(1.37) and (1.38) will give a solution of the wave equation:

$$\boldsymbol{E} = E_0[cos(\omega t - kz)\boldsymbol{e_1} - sin(\omega t - kz)\boldsymbol{e_2}], \tag{1.39}$$

$$\boldsymbol{H} = H_0[cos(\omega t - kz)\boldsymbol{e_1} + sin(\omega t - kz)\boldsymbol{e_2}]. \tag{1.40}$$

In order to examine the polarization character of this new wave, one can study the curve described by the tip of the electric field vector at a fixed plane (e.g. z = 0). At this position, the time dependence of the fields is:

$$\boldsymbol{E_x} = E_0 cos(\omega t) \quad and \quad \boldsymbol{E_y} = -E_0 sin(\omega t), \tag{1.41}$$

$$\boldsymbol{H_x} = H_0 sin(\omega t) \quad and \quad \boldsymbol{H_y} = H_0 cos(\omega t), \tag{1.42}$$

The modulus of the electric field vector is therefore:

$$\boldsymbol{E^2} = \boldsymbol{E_x}^{\boldsymbol{2}} + \boldsymbol{E_y}^{\boldsymbol{2}} \tag{1.43}$$

and for the magnetic field holds:

$$\boldsymbol{H^2} = \boldsymbol{H_x}^{\boldsymbol{2}} + \boldsymbol{H_y}^{\boldsymbol{2}}, \tag{1.44}$$

which indicates that, at a fixed plane, the tip of the electric field vector (and the magnetic field vector) describes a circle. That is why this wave is called circularly polarized. While looking at the wave along the propagation direction, one can observe that the electric field vector rotates contra-clockwise, and therefore it is a left-hand circularly polarized wave.

If two mutually perpendicular linearly polarized waves with the same propagation direction and frequency but with different amplitudes and relative phases are superposed (e.g. at z = 0), we obtain:

$$\boldsymbol{E_x} = E_{01} cos(\omega t - \theta_1) \; and \; \boldsymbol{E_y} = -E_{02} cos(\omega t - \theta_2). \tag{1.45}$$

For such a wave, the relation between the Cartesian components of the electric field is:

$$\left(\frac{\boldsymbol{E_x}}{E_{01}}\right)^{\boldsymbol{2}} + \left(\frac{\boldsymbol{E_y}}{E_{02}}\right)^{\boldsymbol{2}} - 2\frac{\boldsymbol{E_x}}{E_{01}}\frac{\boldsymbol{E_y}}{E_{02}} cos(\theta_2 - \theta_1) = sin^2(\theta_2 - \theta_1). \tag{1.46}$$

This equation represents an ellipse and thus describes an elliptically polarized wave. In general, the principal axis of the ellipse will be tilted with respect to the x and y axis. In particular, for $\theta_2 - \theta_1 = \frac{\pi}{2}, \frac{3\pi}{2}, \ldots$, the major and minor axis of the ellipse will lie along the x and y axis. In this case, if in addition the amplitude of the components are equal $E_{01} = E_{02}$, then the ellipse will degenerate into a circle. For relative phase of $\theta_2 - \theta_1 = 0, \pi, 2\pi, \ldots$, the ellipse will become a straight line, with:

$$\boldsymbol{E_x} = \mp \frac{E_{02}}{E_{01}} \boldsymbol{E_y}, \tag{1.47}$$

which represents once again a linearly polarized wave.

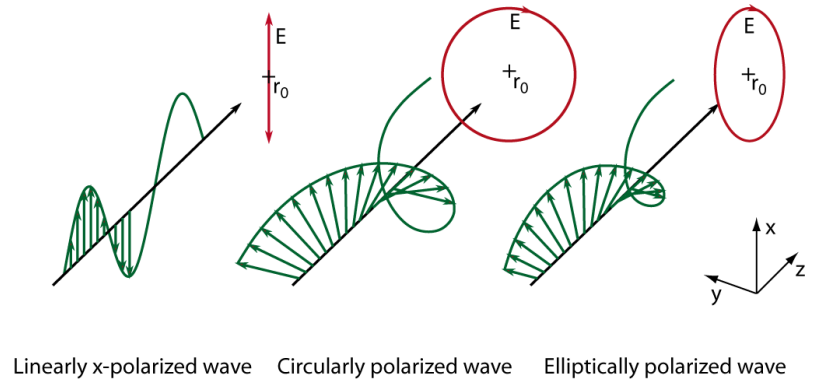

Linearly x-polarized wave Circularly polarized wave Elliptically polarized wave

Figure 1.3: Polarization of light wave.

1.5 Interference

The superposition of two or more waves in space causes an effect of interference. Amplitude of the resulting wave depends on relative phases of the interfering waves. The interfering waves must be coherent as will be clarified in the next chapter. Otherwise the interference pattern changes very quickly with the time and the result is just the mean value of intensity. The second condition is the same polarization direction of the both interfering waves.

The resulting wave function is described by a sum of each single wave. Such a basic principle of superposition results from the linearity of the wave equation (1.13). In the case of monochromatic waves with the same frequencies the principle of superposition for complex amplitudes is still valid. It conforms to the linearity of Helmholtz equation. If we consider two monochromatic waves with complex amplitudes $U_1(\boldsymbol{r})$, $U_2(\boldsymbol{r})$, the resulting wave is also monochromatic (with the same frequency) and its complex amplitude is:

$$U(\boldsymbol{r}) = U_1(\boldsymbol{r}) + U_2(\boldsymbol{r}). \tag{1.48}$$

Intensities of interfering waves are $I_1 = |U_1|^2$ resp. $I_2 = |U_2|^2$ and the resulting intensity is:

$$\begin{aligned} I(\boldsymbol{r}) = |U(\boldsymbol{r})|^2 &= |U_1(\boldsymbol{r}) + U_2(\boldsymbol{r})|^2 = \\ &= |U_1(\boldsymbol{r})|^2 + |U_2(\boldsymbol{r})|^2 + U_1(\boldsymbol{r})U_2{}^*(\boldsymbol{r}) + U_1{}^*(\boldsymbol{r})U_2(\boldsymbol{r}). \end{aligned} \tag{1.49}$$

Using $U_1 = \sqrt{I_1}e^{j\varphi_1}$ and $U_2 = \sqrt{I_2}e^{j\varphi_2}$, where φ_1, φ_2 are corresponding wave phases, the detectable intensity follows an equation:

$$I = I_1 + I_2 + 2\sqrt{I_1 I_2}cos\varphi, \qquad (1.50)$$

where $\varphi = \varphi_2 - \varphi_1$. This relation (1.50), called interference equation, can also be interpreted geometrically as the phasor diagram, which demonstrates that the magnitude of the phasor U is sensitive to the phase difference φ, not only to the magnitudes of the constituent phasors U_1, U_2, see Figure 1.4.

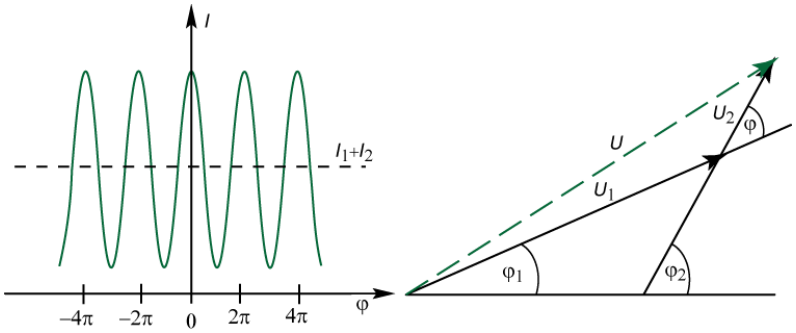

Figure 1.4: Interference of two waves: (left) relation of total intensity I on the phase difference φ; (right) phasor diagram for the superposition of two waves U_1, U_2 and phase difference $\varphi = \varphi_2 - \varphi_1$.

The interference equation (1.50) shows that the superposition of two waves does not correspond to sum of their intensities due to the appearance of the component $2\sqrt{I_1 I_2}cos\varphi$. This term can be positive or negative and influences the brightness of certain parts of interference pattern.

The visibility

$$V = \frac{I_{max} - I_{min}}{I_{max} + I_{min}} \qquad (1.51)$$

is a quantity which acts as a measure for the contrast of an interference pattern. Intensity values I_{max} and I_{min} are two neighboring intensity maxima and minima. The values I_{max} and I_{min} can be calculated by substituting $\varphi = 0$, $\varphi = \pi$ into (1.50). In the case of ideal monochromatic source, the visibility is then

$$V = \frac{2\sqrt{I_1 I_2}}{I_1 + I_2}. \qquad (1.52)$$

If two parallel polarized waves of the same intensity $I_1 = I_2$ interfere, one observes the maximal contrast of $V = 1$. For example, if the ratio of the intensities of interfering waves is 9:1, the contrast becomes 0.6.

1.6 Coherence

Generally the resulting intensity of two different sources, e. g. two electric light bulbs directed on a screen, is additive. Instead of dark and bright fringes as expected by interference equation (1.50) only a uniform brightness according to the sum of the individual intensities can be observed. In order to generate an interference pattern the phases of the individual waves must be correlated in a special way. This correlation property is called coherence and describes the ability of light to "visibly" interfere. The two aspects of coherence are temporal and spatial coherence. The temporal coherence describes the correlation of a wave with itself at different instants of time. A temporal coherence function is introduced for a quantitative description of the temporal coherence. It is defined as the autocorrelation function of a stationary complex random function

$$G(\tau) = \langle U^*(t)U(t+\tau)\rangle = \lim_{T\to\infty}\frac{1}{2T}\int_{-T}^{T} U^*(t)U(t+\tau)dt. \qquad (1.53)$$

It is easy to show that the intensity $I = G(0)$ is equal to $G(\tau)$ if $\tau = 0$. The temporal coherence function $G(\tau)$ carries information about both the intensity $I = G(0)$ and the degree of correlation (coherence) of stationary light. A measure of coherence that is insensitive to the intensity is provided by the normalized autocorrelation function:

$$g(\tau) = \frac{G(\tau)}{G(0)} = \frac{\langle U^*(t)U(t+\tau)\rangle}{\langle U^*(t)U(t)\rangle}, \qquad (1.54)$$

which is called the complex degree of temporal coherence. Its absolute value must follow condition

$$0 \le |g(\tau)| \le 1. \qquad (1.55)$$

When considering a finite coherence length the interference equation (1.50) has to be replaced by

$$I = I_1 + I_2 + 2\sqrt{I_1 I_2}|g(\tau)|cos\varphi \qquad (1.56)$$

and the visibility of the interference pattern becomes:

$$V = \frac{2\sqrt{I_1 I_2}}{I_1 + I_2}|g(\tau)|. \qquad (1.57)$$

For two partial waves with the same intensities $I_1 = I_2$, the visibility is equal to the complex degree of temporal coherence $V = |g(\tau)|$. For ideally monochromatic light or, likewise, light with infinite coherence length the complex degree of

temporal coherence becomes unity: $|g(\tau)| = 1$, while for completely incoherent light is zero $|g(\tau)| = 0$. Values of the complex degree of temporal coherence for partially coherent light fall in interval $0 < |g(\tau)| < 1$. As an example, the complex degree of temporal coherence of electric light bulbs is very close to zero what explains why uniform brightness is observed instead of dark and bright fringes as expected by interference (1.50).

Spatial coherence depicts the mutual correlation of different parts of the same wavefront. If points of the extended light source are superimposed on the screen, it may happen that one source point generates an interference maximum at a certain point on the screen, while another source point generates a minimum at the same screen point. In general the contributions from all source points compensate themselves and therefore the contrast of interference pattern vanishes.

In contrast to the temporal coherence, the spatial coherence depends not only on properties of the light source, but also on the geometry of the interferometer. To consider the spatial coherence, the autocorrelation function defined in (1.53) is extended in order to get the cross correlation function also called mutual coherence function at spatial vectors r_1, r_2:

$$G(\boldsymbol{r_1}, \boldsymbol{r_2}, \tau) = \langle U^*(\boldsymbol{r_2}, t) U(\boldsymbol{r_1}, t+\tau) \rangle = \\ = \lim_{T\to\infty} \frac{1}{2T} \int_{-T}^{T} U^*(\boldsymbol{r_2}, t) U(\boldsymbol{r_1}, t+\tau) dt, \qquad (1.58)$$

Its normalized version forms a complex degree of coherence

$$g(\boldsymbol{r_1}, \boldsymbol{r_2}\tau) = \frac{G(\boldsymbol{r_1}, \boldsymbol{r_2}, \tau)}{\sqrt{G(\boldsymbol{r_1}, \boldsymbol{r_1}, 0) G(\boldsymbol{r_2}, \boldsymbol{r_2}, 0)}}, \qquad (1.59)$$

where $G(\boldsymbol{r_1}, \boldsymbol{r_1}, 0)$ is the intensity at $\boldsymbol{r_1}$ and $G(\boldsymbol{r_2}, \boldsymbol{r_2}, 0)$ is the intensity at $\boldsymbol{r_2}$. The complex degree of coherence describes the degree of correlation between the light field at $\boldsymbol{r_1}$ at time t with the light field at $\boldsymbol{r_2}$ at time $t + \tau$.

1.7 Diffraction

When an optical wave is transmitted through an aperture in an opaque screen and propagates some distance in free space, its intensity distribution is called a diffraction pattern. If light waves were propagated as rays, the diffraction pattern would be a shadow of the aperture. Due to the wave nature of light, the diffraction pattern may deviate from the aperture shadow, depending on the distance between the aperture and screen, the wavelength, and the dimensions of the aperture.

There exist two basic approaches how to solve such a diffraction task:

- Rigorous methods [58] – come from laws of Physics and follow the nature of the electrodynamic boundary conditions. They consider the opaque screen with defined properties such as perfect or partial conductivity. Consequently, the field in front of the aperture is also affected.
- Approximate methods [58] – include scalar approach and assume that the impinging wave is transmitted without change at points within the aperture, but is reduced to zero at points on the back side of the opaque part of the screen.

Problems solved by rigorous methods are limited due to the computational complexity. For most of optical tasks (including digital holography) the use of rigorous approach is not necessary. Therefore, we will only concentrate on approximate methods; however, for some special optical problems or some radio frequency tasks the use of a rigorous method is unavoidable.

In order to set up relevant approximations, we have to define some constrains where the approximations are still valid. The main approximation is implementation of the scalar theory. Wave equation defined in (1.13) is valid for homogeneous medium. In inhomogeneous medium, where the permittivity $\varepsilon(\boldsymbol{r})$ is a function of position $\mathbf{r}$, it is no longer possible to represent all components by one function. It follows that the validity of the scalar approximation for the case of diffraction on the aperture depends on the size of the contribution from the edges of the aperture, where the medium is supposed to be inhomogeneous. The scalar approximation can therefore be used if:

- the aperture is much greater than the wavelength of diffracted light
- the observation plane is in a sufficient distance from the aperture

The first scalar diffraction theory introduced by Fresnel in 1818 made a breakthrough in understanding of light. In 1882 Kirchhoff figured out mathematically more consistent diffraction theory. The Kirchhoff's theory was then improved by Sommerfeld in 1894; however, in the paraxial area all the theories provide more-or-less the same results.

In next paragraphs, the basic idea of the Kirchhoff approach is introduced. For detailed analysis, see [58]. Let us consider the situation outlined in Figure 1.5. An aperture is illuminated by a light source O and the wave amplitude $U(P)$ is observed at the point P. To discuss the influence of this light propagating through the aperture, we assume a domain S consisting of three regions S1, S2, and S3.

We need to integrate the contribution from a small area dS over the domains S1, S2, and S3.

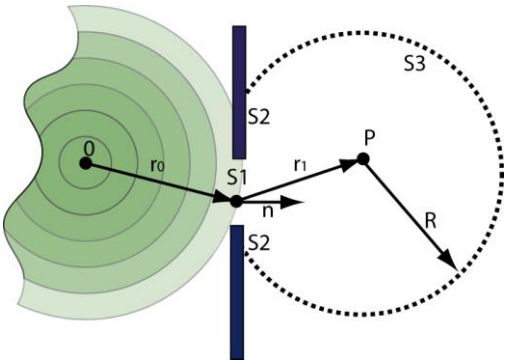

Figure 1.5: Geometry for Kirchhoff approach.

This domain S is enclosed by a screen S2 (there is no contribution from this area, because the light amplitude does not exist there), a semi-sphere S3 with the observation point P at the center (there is also no contribution due to the Sommerfeld radiation condition), and the aperture S1 which dominates the wave $U(P)$ at the point P. If we skip sophisticated discussion, the next equation called the Kirchhoff diffraction formula is obtained using wave number k and incident wave amplitude U_0:

$$U(P) = \frac{jU_0}{2\lambda} \iint_{S1} \frac{exp[-jk(r_0 + r_1)]}{r_0 r_1} (cos(r_1, \boldsymbol{n}) + cos(r_0, \boldsymbol{n}))dS. \qquad (1.60)$$

The part $j/2\lambda\,(cos(r_1, \boldsymbol{n}) + cos(r_0, \boldsymbol{n}))$ is usually called the inclination factor with the unit normal vector $\boldsymbol{n}$ to the surface of the aperture.

In the Kirchhoff theory (and all other approximation methods) there are some mathematical inconsistencies. For instance, one of the Kirchhoff´s boundary condition supposes the field value U and its first derivative to be equal to zero behind the opaque screen. It is in breach with the Green formula conditions defining the wave field U and its first and second derivatives to be single-valued and continuous within and on the domain S. However, the difference between Kirchhoff method and rigorous methods has only an impact when the observation plane is very close (few wavelengths) to the aperture. Otherwise the solution of the Kirchhoff (or Sommerfeld) solution does not considerably differ from rigorous methods.

The diffraction integral can be further simplified. If the light source is located far from the screen, $cos(r_0, \boldsymbol{n}) = 1$. In addition, if the observation point is far from the screen, the angle $cos(r_1, \boldsymbol{n})$ becomes nearly zero and the inclination factor is

approximately j/λ. Considering distances appearing in interferometric setups, these simplifications are perfectly relevant. This means that the complex amplitude is given by the following expression:

$$U(P) = \frac{jU_0}{\lambda} \iint_{S1} \frac{exp[-jk(r_0 + r_1)]}{r_0 r_1} dS, \qquad (1.61)$$

However, except a limited number of cases, it is still difficult or even impossible to solve the formula explicitly due to the integral term in the expression (1.61). In order to get an "easy to solve" description of diffraction, a further approximation must be introduced.

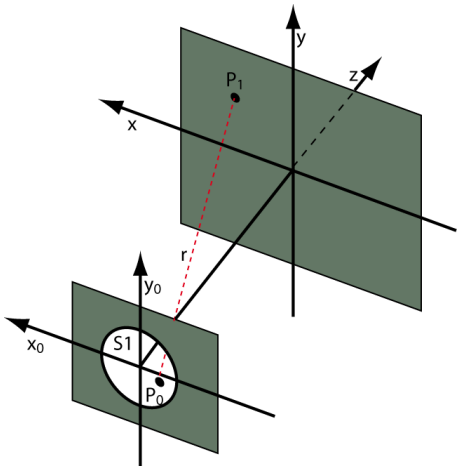

Figure 1.6: Coordinates in aperture and observation planes.

Let the aperture S1 be illuminated by the parallel uniformed beam from the source; then, points (x_0, y_0) within the aperture S1 play the role of a light sources which produce the diffracted pattern on the observing screen. The point $P_0(x_0, y_0, 0)$ is located on the aperture plane, while the observing point $P_1(x, y, z)$ is located on the screen, see Figure 1.6. The distance $|P_0\, P_1|$ is expressed by r and the complex amplitude $U(P_1)$ is calculated by[1]:

$$U(P_1) = \frac{j}{\lambda} \iint_{S1} h(x_0, y_0, 0) \frac{exp[-jkr]}{r} dx_0 dy_0, \qquad (1.62)$$

where $r = \sqrt{(x_0 - x)^2 + (y_0 - y)^2 + z^2}$. However, this r makes the integration difficult. The Taylor series decomposition:

[1] $h(x_0, y_0, 0)$ represents transmittance function. In this case $h(x_0, y_0, 0) = 1$ if $h(x_0, y_0, 0) \in S1$ otherwise $h(x_0, y_0, 0) = 0$. In general, $h(x_0, y_0, 0)$ can be any number including complex numbers.

$$r = \sqrt{(x_0 - x)^2 + (y_0 - y)^2 + z^2} \sim z + \frac{1}{2z}[(x_0 - x)^2 + (y_0 - y)^2] - \frac{1}{8z}[(x_0 - x)^2 + (y_0 - y)^2]^2 + \cdots \quad (1.63)$$

can be used to avoid the square root in (1.62). Omitting the third and higher terms of this expansion, the diffraction integral in arbitrary point on the screen becomes:

$$U(x,y,z) = \frac{j}{z\lambda} exp\left(-\frac{j\pi}{\lambda z}[x^2 + y^2]\right) \times \times \iint_{-\infty}^{\infty} h(x_0, y_0, 0)\, exp\left(-\frac{j\pi}{\lambda z}[{x_0}^2 + {y_0}^2]\right) \times \times exp\left(-j2\pi[x_0 \frac{x}{\lambda z} + y_0 \frac{y}{\lambda z}]\right) dx_0 dy_0. \quad (1.64)$$

This approximation is known as the Fresnel approximation. The error caused by the omitting of the higher terms of the Taylor series is small if the third term meets condition:

$$\frac{1}{8} kz \left(\frac{x^2 + y^2}{z^2}\right)^2 \ll \frac{\pi}{2}. \quad (1.65)$$

The value $\pi/2$ is limiting value when the omitted term causes sign change of the complex field $U(x,y,z)$. Considering $\left(\frac{x^2+y^2}{z^2}\right) = tan^2(r_1, \boldsymbol{n})$ the condition holds:

$$tan^4(r_1, \boldsymbol{n}) < \frac{2\lambda}{z}. \quad (1.66)$$

It follows that the Fresnel approximation can be relevantly used in the paraxial area.

One can go even further and put $exp\left(-\frac{j\pi}{\lambda z}[{x_0}^2 + {y_0}^2]\right) \approx 1$ in (1.64). The diffraction formula:

$$U(x,y,z) = \frac{j}{z\lambda} exp\left(-\frac{j\pi}{\lambda z}[x^2 + y^2]\right) \times \times \iint_{-\infty}^{\infty} exp\left(-j2\pi[x_0 \frac{x}{\lambda z} + y_0 \frac{y}{\lambda z}]\right) dx_0 dy_0 \quad (1.67)$$

is called the Fraunhofer approximation. The condition for the Fraunhofer approximation is $\frac{j\pi}{\lambda z}[{x_0}^2 + {y_0}^2] \ll \frac{\pi}{2}$ from the same reason as in case of the Fresnel approximation.

From the physical point of view, the Fresnel approximation replaces the spherical waves describing the point source light propagation by waves with parabolic wavefronts, while the Fraunhofer approximation uses even plane wavefronts.

Figure 1.7 shows how the space behind the aperture is divided according to the validity of different approximations.

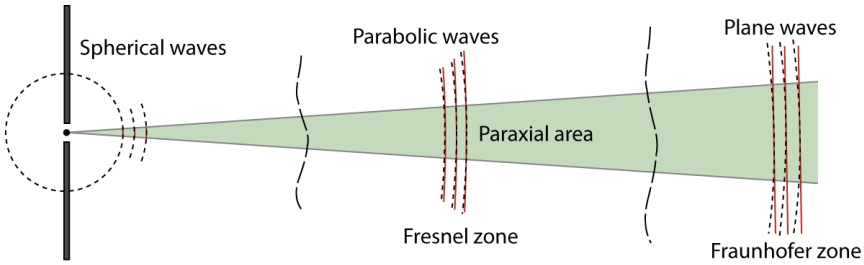

Figure 1.7: Fresnel and Fraunhofer zones.

2 Holography

2.1 Principles of Holography

Holography involves recording and reconstruction of optical waves [59], [60]. Optical wave carries information about its amplitude and phase; however, only the amplitude information can be retrieved by optical detectors (human eye, photographic film, CCD, CMOS, etc.) as detected intensity. Information about phase of the wave is lost during the recording process. Nevertheless, the phase indicates a directionality of optical waves, thus determines the effects like depth and parallax of the observing scene. Due to lack of "phase-sensitive" detectors, it is necessary to code the phase information into the amplitude information, which can be detected.

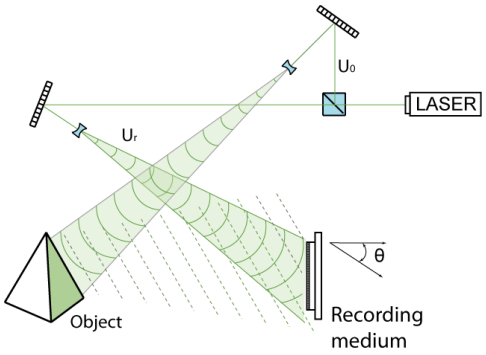

Figure 2.1: Off-axis experimental arrangements for recording of a hologram. Recording medium can be e.g. silver halide holographic plate or digital sensor. The reference and the object wave are generated by the same laser source due to coherence requirements.

Such a code is based on combination of the original wave - the object wave U_0 with a known reference wave U_r and recording their interference pattern[1]. The interference pattern is very sensitive to phase difference of the interfering waves, see (1.50). The intensity of the sum of the two waves is recorded, forming a transmittance h. This transmittance (called a hologram) is described by interference formula:

$$h \approx |U_o + U_r|^2 = |U_o|^2 + |U_r|^2 + U_o U_r^* + U_o^* U_r. \qquad (2.1)$$

The hologram h carries coded information about the intensity (amplitude) and phase of the object wave U_o. This procedure is called "recording." An experimental arrangement for recording of a hologram is outlined in Figure 2.1.

[1] Coherence and polarization conditions must be fulfilled.

The second step in holography is reconstruction of the hologram. To decode the information from the hologram and reconstruct the object wave, the reference wave U_r must again illuminate the hologram. The result is a wave with complex amplitude:

$$U = hU_r \approx U_r(I_r + I_0) + I_r U_0 + {U_r}^2 {U_0}^*. \qquad (2.2)$$

The term $I_r U_0$ is the original wave multiplied by the intensity of the reference wave I_r. If I_r is uniform this term constitutes the desired reconstructed wave. The term ${U_r}^2 {U_0}^*$ is a conjugated version of the original wave modulated by ${U_r}^2$ and the term $U_r(I_r + I_0)$ represents the reference wave, modulated by the sum of the intensities of the reference I_r and the object I_0 wave.

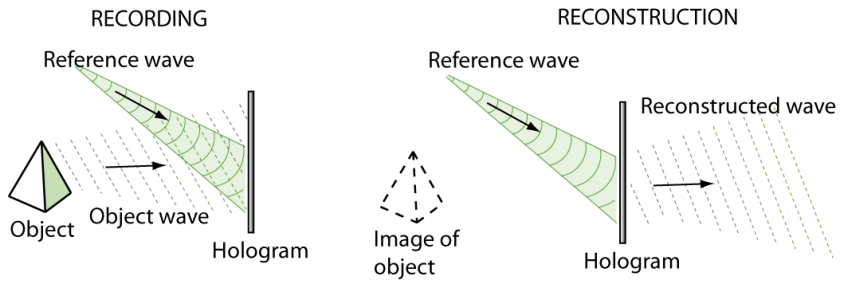

Figure 2.2: Principle scheme of a hologram recording and its reconstruction.

In Gabor´s original work, the hologram was recorded when the object wave and the reference wave were parallel. Such a type of the recording is called the inline holography. In this case, the four components of (2.2) propagate along the same direction and cannot be observed separately. The idea with off-axis holography is to introduce an angle ϑ between the directions of propagation of the object wave and the reference wave. Therefore, the different terms of the interference propagate along separated directions during the reconstruction. When the reference wave is tilted in x directions, the reconstructed complex amplitude becomes:

$$U \approx U_r(I_r + I_0) + I_r\, exp(-jkx\, sin(\vartheta))\, U_0 + {U_r}^2\, exp(jkx\, sin(\vartheta))\, {U_0}^*. \qquad (2.3)$$

The phase factor $exp(-jkx\, sin(\vartheta))$ in the second term, which produces the virtual image, indicates that the wave is deflected with an angle $-\vartheta$ with respect to the direction of the illuminating wave U_r. The opposite phase factor appears in the third term, meaning that the wave producing the real image is deflected with an angle ϑ. The zero order of diffraction propagates in the same direction as U_r. In

other words, the off-axis geometry spatially separates the different orders of diffraction, allowing an individual observation of each term. The recording and reconstruction procedures are schematized in Figure 2.2.

2.2 Recording of digital hologram

The aim of digital holography is to record holograms, which are later stored in a computer memory and can be reconstructed numerically afterwards. The digital recording medium is usually CCD or CMOS camera. The basic principle of digital hologram recording is the same as in the conventional holography. Only the recording medium is different. The hologram is a microscopic interference pattern generated by the coherent superposition of an object and a reference wave as was mentioned in the previous chapter.

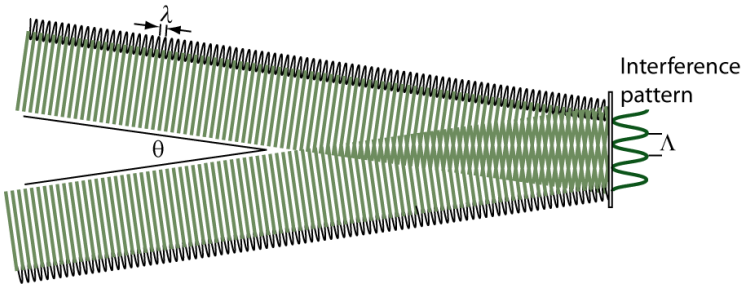

Figure 2.3: Interference of two plane waves at angle θ.

The spatial frequency $1/\Lambda$ of such interference pattern is defined by the angle θ between these two waves (see Figure 2.3):

$$\Lambda = \frac{\lambda}{sin\theta}. \tag{2.4}$$

A sampling of the interference pattern constituting the hologram must follow the sampling theorem. The sampling theorem requires that the spatial period Λ must be sampled with more than two pixels:

$$\Lambda > 2\Delta\xi, \tag{2.5}$$

where $\Delta\xi$ is the pixel size. For small values of angle θ we can put $sin\theta \approx \theta$. Hence, the limit value for the angle θ_{max}, which is the maximum angle formed by the reference and the object wave when the sampling theorem is followed, can be determined as:

$$\theta_{max} \approx \frac{\lambda}{2\Delta\xi}. \tag{2.6}$$

Naturally, the sampling theorem must also be followed for conventional holography. However, the resolution of digital cameras is much lower when compared to analog recording media and therefore it is more difficult to fulfil the conditions of sampling theorem.

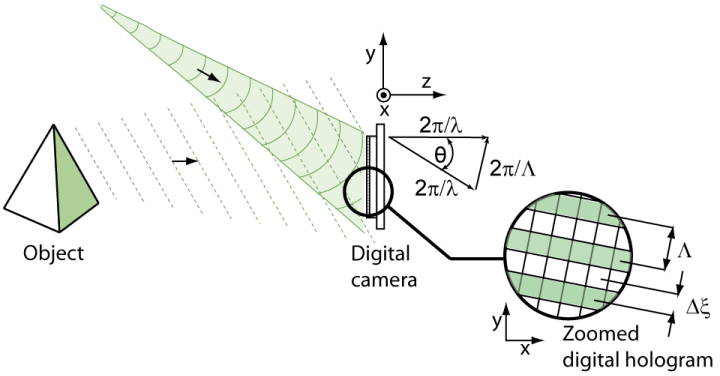

Figure 2.4: Recording of a digital hologram in off-axis arrangements. The pixelated digital sensor naturally samples the microinterference patterns. The boundary situation when the hologram fulfills the sampling criterion is outlined in the zoomed image.

Let us consider geometry shown in Figure 2.5. The object has a width d_0 along the x direction symmetrically to the optical axis, and the reference wave propagates along the optical axis and impinges orthogonally onto the sensor. The maximum object width d_0 for a given distance d is calculated according to:

$$tan\theta = \frac{\frac{d_0}{2} + \frac{N\Delta\xi}{2}}{d}, \tag{2.7}$$

where N denotes number of pixels of the digital sensor in x direction. Using the condition for the maximum angle θ_{max} (2.6) the equation (2.7) becomes[1]:

$$\frac{\lambda}{2\Delta\xi} = \frac{\frac{d_0}{2} + \frac{N\Delta\xi}{2}}{d} \tag{2.8}$$

and hence we obtain condition:

$$d_0 < \frac{\lambda d}{\Delta\xi} - N\Delta\xi, \tag{2.9}$$

which describes the limit for a maximal width d_0 of the object with respect to the distance d in order to fulfil the sampling theorem.

In practical applications one has to often record large objects. Holographical recording of large objects can fail to meet the condition (2.9). In this case,

[1] Approximation $\tan\theta \approx \theta$ was used for small angles.

the wave field scattered from the surface of object must be reduced by the use of a negative lens, see Figure 2.5.

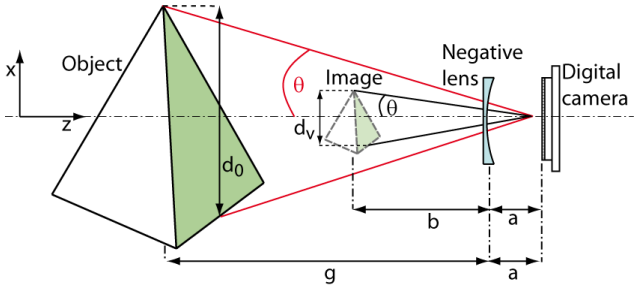

Figure 2.5: Reduction of an imaging angle by using a negative lens.

After the placement of appropriate negative lens in the experimental arrangements, the scattered object wave field seems to come from the small virtual image of the object of width d_v instead of the large object having width d_0. Using the lens formula $\frac{1}{f}=\frac{1}{g}-\frac{1}{b}$, magnification formula $Z=\frac{d_v}{d_0}=\frac{f}{g-f}$ and the geometry $tan\theta=\frac{d_v}{2(a+b)}$ we can derive the term for distance between the lens and the sensor:

$$a=\frac{fg}{g-f}-\frac{fd_0}{(g-f)2tan\theta}. \qquad (2.10)$$

The distance between the digital camera and the small virtual image of the object is $d=a+b$ instead of the original distance $d=a+g$. It can be seen, $\theta_{reduced} \ll \theta_{lensless}$ thererofe it is much easier to fulfill the sampling theorem.

2.3 Reconstruction of digital holograms

The reconstruction in the conventional holography requires illumination of the hologram by a reference wave. In digital holography this process is modeled numerically. A digital hologram h is multiplied by a conjugated reference wave Ur^*, which results in numerical representation of a wave field in hologram plane (with coordinates notation ξ,η). This wave field is then numerically propagated in a free space according to laws of diffraction and the resulting complex field is calculated in a certain reconstruction distance d – where is the image plane (x,y).

Plane or spherical wave is usually used as a reference wave when capturing the digital hologram [61]. This fact must be taken into consideration when choosing appropriate reference wave for reconstruction. A plane wave having

amplitude A and impinging the digital camera at angles θ_1, θ_2 with respect to the normal of the digital sensor is described by expression :

$$Ur^* = Aexp\frac{j2\pi}{\lambda}(sin\theta_1\xi + sin\theta_2\eta). \qquad (2.11)$$

Spherical wave which is generated by a source point at distance d_{Sph} from the image plane is expressed by formula:

$$Ur^* = Ae^{\frac{j2\pi d_{Sph}}{\lambda}}e^{\frac{j\pi}{\lambda d}(\xi^2+\eta^2)}. \qquad (2.12)$$

In order to calculate complex amplitude U at image plane (x,y) we start from Kirchhoff integral (1.62):

$$U(x,y) = \frac{1}{j\lambda}\iint h(\xi,\eta)Ur^*(\xi,\eta)\frac{exp(jkr)}{r}d\xi d\eta, \qquad (2.13)$$

where $r = \sqrt{d^2+(\xi-x)^2+(\eta-y)^2} = d\sqrt{1+\frac{(\xi-x)^2+(\eta-y)^2}{d^2}}$. We focus on two basic solutions of the Kirchhoff diffraction integral: Fresnel approximation (sometimes called Fresnel transformation) and convolution approach.

The Fresnel approximation omits third and higher terms of the Taylor series of function r in (2.13) in the same manner as described in chapter 1.7. The Fresnel transformation reconstructs the complex amplitude in image by expression:

$$\begin{aligned} U(x,y,d) = \frac{j}{d\lambda}exp\left(-\frac{j\pi}{\lambda d}[x^2+y^2]\right)\times \\ \times\iint_{-\infty}^{\infty} h(\xi,\eta)\,Ur^*(\xi,\eta)exp\left(-\frac{j\pi}{\lambda d}[\xi^2+\eta^2]\right)\times \\ \times exp\left(-j2\pi[\xi\frac{x}{\lambda d}+\eta\frac{y}{\lambda d}]\right)d\xi d\eta. \end{aligned} \qquad (2.14)$$

Since the reconstruction is performed numerically, we need a discrete version of the formula (2.14). The sampling of the hologram plane is naturally determined by pixel extensions of the digital sensor $\Delta\xi \times \Delta\eta$ and number of pixels $N \times M$:

$$\xi = k\Delta\xi \;\; where \;\; 1 < k < N \;\; and \;\; \eta = l\Delta\eta \;\; where \;\; 1 < l < M. \qquad (2.15)$$

Image plane is also sampled having the same number of elements:

$$x = n\Delta x \;\; where \;\; 1 < n < N \;\; and \;\; y = m\Delta y \;\; where \;\; 1 < m < M. \qquad (2.16)$$

Substituting (2.15) and (2.16) into (2.14) one obtains discrete version of the reconstruction formula by Fresnel transform:

$$U(n\Delta x, m\Delta y) = \frac{j}{d\lambda} exp\left(-\frac{j\pi}{\lambda d}[(n\Delta x)^2 + (m\Delta y)^2]\right) \times \\ \times \sum_{n=1}^{N}\sum_{m=1}^{M} h(k\Delta\xi, l\Delta\eta)\, Ur^*(k\Delta\xi, l\Delta\eta) \times \\ \times exp\left(-\frac{j\pi}{\lambda d}[(k\Delta\xi)^2 + (l\Delta\eta)^2]\right) \times \\ \times exp\left(-j2\pi\left(\frac{kn}{N} + \frac{lm}{M}\right)\right) d\xi d\eta. \tag{2.17}$$

Image plane pixel extensions $\Delta x, \Delta y$ are given by the size of the frame $N\Delta\xi \times M\Delta\eta$, the distance d and the wavelength λ by equations:

$$\Delta x = \frac{\lambda d}{N\Delta\xi} \quad and \quad \Delta y = \frac{\lambda d}{M\Delta\eta}. \tag{2.18}$$

The Fresnel transform can be effectively calculated with the use of FFT algorithm (Fast Fourier Transform). If we take a look at the last term in the formula (2.17) one can recognize the expression of Fourier transform. Therefore, the formula (2.17) can be rewritten as:

$$U(n\Delta x, m\Delta y) = \frac{j}{d\lambda} exp\left(-\frac{j\pi}{\lambda d}[(n\Delta x)^2 + (m\Delta y)^2]\right) \times \\ \times \mathcal{F}^{-1}\left\{h(k\Delta\xi, l\Delta\eta) Ur^*(k\Delta\xi, l\Delta\eta) exp\left(-\frac{j\pi}{\lambda d}[(k\Delta\xi)^2 + (l\Delta\eta)^2]\right)\right\}, \tag{2.19}$$

where $\mathcal{F}^{-1}$ denotes the inverse discrete Fourier transform.

The convolution approach is another way of the digital hologram reconstruction. The Kirchhoff integral (2.13) can be viewed as a superposition integral:

$$U(x,y) = \iint h(\xi,\eta) Ur^*(\xi,\eta) g(x-\xi, y-\eta)\, d\xi d\eta \tag{2.20}$$

with the impulse response

$$g(x,y) = \frac{1}{j\lambda} \frac{exp\left(jk\sqrt{d^2 + x^2 + y^2}\right)}{\sqrt{d^2 + x^2 + y^2}}. \tag{2.21}$$

Free space, in which the diffracted wave propagates, is space-invariant $g(x, y, \xi, \eta) = g(x - \xi, y - \eta)$ and therefore the superposition integral can be regarded as a convolution. Applying convolution theorem, the reconstruction formula can be written in the form:

$$U(x,y) = (hUr^*) * g = \mathcal{F}^{-1}\{\mathcal{F}(hUr^*)\mathcal{F}(g)\}. \tag{2.22}$$

The reconstruction process described by (2.22) involves three Fourier transforms. The individual Fourier transforms can be carried out using the FFT-algorithm (Fast Fourier Transform).

The discrete version of impulse response is

$$g(n,m) = \\ = \frac{1}{j\lambda}\frac{exp\left(j\frac{2\pi}{\lambda}\sqrt{d^2+(n-N/2)^2\Delta\xi^2+(m-M/2)^2\Delta\eta^2}\right)}{\sqrt{d^2+(n-N/2)^2\Delta\xi^2+(m-M/2)^2\Delta\eta^2}}. \quad (2.23)$$

The shift of the coordinates about $N/2$ respectively $M/2$ is introduced due to symmetry reasons. The Fourier transform $G(k,l)$ of impulse response $g(n,m)$ is transfer function of the linear system. Transfer function $G(k,l)$ can be calculated and expressed analytically as

$$G(k,l) = exp\left(j\frac{2\pi d}{\lambda}\sqrt{1-\frac{\lambda^2\left(\frac{k+N^2\Delta\xi^2}{2d\lambda}\right)^2}{N^2\Delta\xi^2}+\frac{\lambda^2\left(\frac{l+M^2\Delta\eta^2}{2d\lambda}\right)^2}{M^2\Delta\eta^2}}\right), \quad (2.24)$$

which saves one Fourier transform for complex field calculation within reconstruction:

$$U(x,y) = \mathcal{F}^{-1}\{\mathcal{F}(hUr^*)G\}. \quad (2.25)$$

The pixel extensions in image plane reconstructed by the convolution approach are equal to that of the hologram:

$$\Delta x = \Delta\xi \quad and \quad \Delta y = \Delta\eta. \quad (2.26)$$

The resolution (2.26) of the reconstructed images in image plane differs from that of the Fresnel transform (2.18). At first sight it seems to be possible to achieve a higher resolution with the convolution approach if the pixel extensions $\Delta\xi \times \Delta\eta$ are small enough. On closer examination one recognizes that the resolution calculated by (2.26) is only a numerical value. The physical resolution in image plane is determined by the diffraction limit. Considering the digital camera sensor as an aperture of the optical system $N\Delta\xi \times M\Delta\eta$, the diffraction limit (Airy disc diameter) defined by this rectangle aperture corresponds to the resolution of the Fresnel transformation (2.18). It follows that Fresnel transformation can be regarded as the "automatically scaling" algorithm, setting the resolution of the image reconstructed by a discrete Fresnel transform always to the physical limit.

Image plane resolution computed by the both convolution approach and Fresnel transform is fixed; however, sometimes it is desired to have the possibility to vary it. For that we can introduce a numerical lens [26] with focal length

$$f = \left(1/d + 1/\dot{d}\right)^{-1} \tag{2.27}$$

in the reconstruction process. In (2.27) the reconstruction distance $\dot{d}$ is $\dot{d} = dM$, where M stands for the magnification factor. Now we can define a lens transmission function

$$L(\xi, \eta) = exp\left[\frac{j\pi}{\lambda}\left(1/d + 1/\dot{d}\right)(\xi^2 + \eta^2)\right] \tag{2.28}$$

and modified the formula (2.22) to be:

$$U(x, y) = \mathcal{F}^{-1}\{\mathcal{F}(L\ h\ Ur^*)\mathcal{F}(g)\}. \tag{2.29}$$

We should note, that the reconstruction distance $\dot{d}$ instead of d must be applied in the reconstruction process. A magnification of $M = 1$ obviously corresponds to image resolution $\Delta x = \Delta\xi$ resp. $\Delta y = \Delta\eta$.

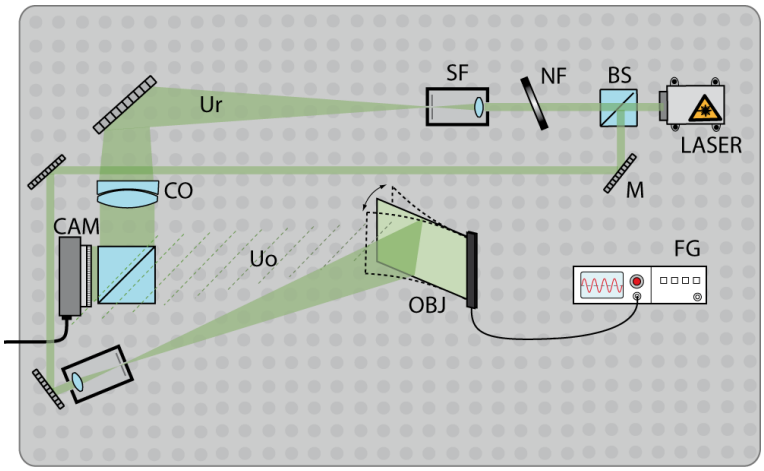

Figure 2.6: Principal scheme of a holographic interferometer employing components: BS - beam splitter, NF - neutral density filter, SF - spatial filter, CO - collimating objective, OBJ - object, FG - arbitrary waveform generator, CAM - digital camera, M - mirror, *Ur* denotes reference wave while *Uo* stands for object wave.

The result of reconstruction process $U(n\Delta x, m\Delta y)$ is a numerical representation of a complex optical wave field in the image plane. Hence, intensity $I(n\Delta x, m\Delta y)$ and phase $\varphi(n\Delta x, m\Delta y)$ distributions can be computed as:

$$I(n\Delta x, m\Delta y) = |U(n\Delta x, m\Delta y)|^2, \tag{2.30}$$

$$\varphi(n\Delta x, m\Delta y) = arctan\frac{Im\{U(n\Delta x, m\Delta y)\}}{Re\{U(n\Delta x, m\Delta y)\}}, \tag{2.31}$$

respectively. The possibility of the direct phase calculation is a real advantage comparing to the optical reconstruction in the conventional holography, where only the intensity distribution is available. At first sight it seems that the phase calculation has no importance, because for rough object surfaces it varies stochastically. However, the phase calculation brings real advantage when it comes to applications in double exposure digital holographic interferometry [25], [62].

An example of off-axis digital holography is provided in Figure 2.6. The object - a steady beam cantilever - is $d = 0.6\,m$ apart from the sensor of AVT Stingray digital camera with parameters $N = M = 2048\,pix$ and $\Delta\xi = \Delta\eta = 3.45\,\mu m$. Light of wavelength $\lambda = 532nm$ was emitted by Nd:YAG laser. Digital hologram, as a result of interference between the reference plane wave and the object wave scattered from the object, is shown in Figure 2.7 (left). Field of intensity distribution calculated by Fresnel transform has a width of $N\Delta x = \frac{\lambda d}{\Delta\xi} = 92.5\,mm$. On closer examination of reconstruction equation (2.2) we can distinguish three different wave fields originating behind the hologram plane. The reconstructed wave field includes information about the object wave (real image) $I_r U_0$ as well as about its conjugated wave (virtual image) ${U_r}^2 {U_0}^*$ and reference wave (d.c.-term) $U_r(I_r + I_0)$, see Figure 2.7 (right).

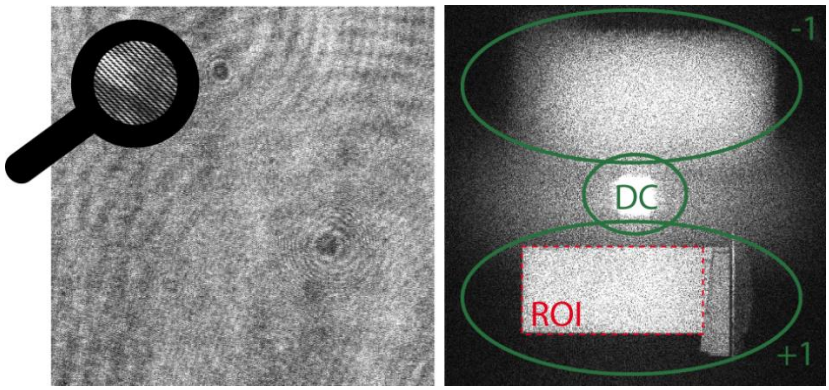

Figure 2.7: (left) Captured digital hologram with zoomed micro interference structure; (right) reconstructed intensity distribution by Fresnel transformation. Green ellipses denote different reconstructed diffraction orders and the dashed red rectangle delineates the region of interest (ROI) – surface of the cantilever.

The real image corresponds to a wavefront converging to a sharp image, while the virtual image belongs to a divergent wavefront that seems to be not in focus. However the virtual image can also be reconstructed. Here the non-conjugated reference wave must be used. This can be done by the numerical calculation of

the field in the plane $z = -d$ which corresponds to the object plane. For more detailed information about the virtual image reconstruction, see [25].
Another component, which can be seen in the intensity distribution image as a bright central square, is a d.c.-term. It is much brighter than the reconstructed real or virtual images. The physical meaning of the bright central square is a representation of the zero-order diffraction of the reference wave (whereas real and virtual image represents the first or the minus first diffraction order). The bright square can be regarded as the undiffracted part of the reference wave or (from the calculation point of view) the d.c. - term of the Fresnel hologram. A mutual location of these components is given by the holographic setup, specifically, by angle of the reference and the object wave as introduced in (2.3). If the angle is too small, the real image in Fourier domain is overlapped by the virtual image or by the d.c.-term. To suppress the overlapping components we can change the holographic setup in order to have all the components in frequency domain well separated. Alternatively it is possible to use some numerical filters [63] or phase shifting technique [64].

2.4 Time Average Digital Holography

Time average digital holography is used to measure the vibration amplitudes of diffusely reflecting objects harmonically oscillating with an angular frequency ω. The displacement vector of the object point R can be written as:

$$\boldsymbol{d}(R,t) = \boldsymbol{d}(R)\, sin\big(\omega t + \psi_0(R)\big). \qquad (2.32)$$

It is important to know the connection between the phase change $\Omega(R)$ of the scattered wave from object and the geometrical displacement $\boldsymbol{d}(R)$ of each surface point R, which influences the optical path difference $\delta(R)$. This is the difference between the paths from the source point S of the illuminating wavefront over the surface point R to the observation point B before and after change of the deformation state. The phase of the object wave $\Omega(R)$ is related to this path difference as:

$$\Omega(R) = \frac{2\pi}{\lambda}\delta(R). \qquad (2.33)$$

Consider illumination point S and observation point B (see Figure 2.8). If the object is deformed by oscillations, the surface point R moves from a position

R_1 to a new position R_2. This change of position is called the displacement vector $d = R_2 - R_1$. Now we can determine the optical path difference as follows:

$$\delta(R) = |S\,R_1| + |\,R_1B| - |S\,R_2| - |\,R_2B| = \\ = s_1S\,R_1 + b_1\,R_1B - s_2S\,R_2 - b_2\,R_2B, \tag{2.34}$$

where s_1 and s_2 are unit vectors in the direction of illumination, b_1 and b_2 are unit vectors in the observation direction. Further $S\,R_i$ and R_iB are the vectors from S to R_i or R_i to B.

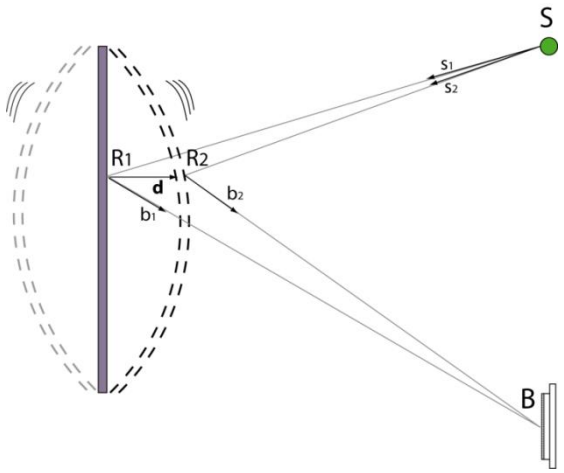

Figure 2.8: Geometry regarded in time average digital holography.

From Figure 2.8 we can also determine the equation for the displacement vector:

$$\boldsymbol{d}(R) = \boldsymbol{R_1B} - \boldsymbol{R_2B} = \boldsymbol{S\,R_2} - \boldsymbol{S\,R_1}. \tag{2.35}$$

Because amplitudes of an oscillating object are much smaller than the distances in holographic setup (the displacement d is in the nano or micrometer range, whereas the distances $|S\,R_i|, |\,R_iB|$ are in range of meters), unit vectors in the direction of illumination s_1, s_2 can be considered as well as in the observation direction b_1, b_2 can be considered parallel. Hence we can use $b = b_1 = b_2$, $s = s_1 = s_2$ and using (2.35) on (2.34) we get:

$$\delta(R) = \boldsymbol{d}(R)[\boldsymbol{b}(R) - \boldsymbol{s}(R)]. \tag{2.36}$$

Now we can define the so called sensitivity vector:

$$\boldsymbol{e}(R) = \frac{2\pi}{\lambda}[\boldsymbol{b}(R) - \boldsymbol{s}(R)]. \tag{2.37}$$

The sensitivity vector is defined by the geometry of the holographic setup. With the use of (2.33), the phase of the object wave phase is related to the displacement vector d as:

$$\Omega(R) = \boldsymbol{d}(R)\boldsymbol{e}(R). \tag{2.38}$$

At any time t, the illuminated surface of the object at point R diffuses an optical wave $U_O(R,t)$ with an amplitude $U_0(R)$, written as:

$$U_O(R,t) = U_0(R)exp(j\Omega(R)\,sin[\omega t + \psi_0(R)]). \tag{2.39}$$

The oscillating object is recorded holographically capturing a digital hologram according to equation $h \approx |U_o + U_r|^2$, see (2.1). The reference wave U_r can be either plane or spherical. The captured hologram will necessarily be time integrated over the exposure time T by the digital sensor:

$$h(\xi,\eta,0) = \int_0^T h(\xi,\eta,0,t)\,dt. \tag{2.40}$$

We can apply equation (2.19) or (2.22) in order to numerically reconstruct the complex field in the image plane. From (2.2) it is obvious, that the computed field is comprised of three different parts: the sharp real image, the blurred virtual image and the d.c. term. The complex field of the real image carrying information about the object wave is proportional to:

$$U_{real}(R,t) \approx \int_0^T U_0(R)exp(j\Omega(R)\,sin[\omega t + \psi_0(R)])\,dt. \tag{2.41}$$

By proper combination of the power series components and using the Euler formula we obtain the formula[1]:

$$\sum_{n=0}^{\infty} J_n(A)\,exp(jnB) = exp(jA\,sin(B)), \tag{2.42}$$

where J_n is the *n-th* kind zero-order Bessel function [65]. Applying (2.42) on (2.41), the complex field becomes:

$$\begin{aligned} U_{real}(R,t) &\approx \int_0^T \sum_{n=0}^{\infty} U_0(R)J_n\big(\Omega(R)\big)\,exp(jn[\omega t + \psi_0(R)])\,dt = \\ &= \sum_{n=0}^{\infty} U_0(R)J_n\big(\Omega(R)\big)\int_0^T exp(jn[\omega t + \psi_0(R)])\,dt. \end{aligned} \tag{2.43}$$

[1] Called Jacobi–Anger expansion.

In time average holography the exposure time is much longer when compared to the period of the vibration of the object[1] $T \gg 2\pi/\omega$. The averaging process can be mathematically expressed by limit as time approaches infinity and therefore:

$$U_{Real}(R) = \lim_{T\to\infty} \sum_{n=0}^{\infty} U_0(R) J_n\big(\Omega(R)\big) \int_0^T exp(jn[\omega t + \psi_0(R)])\, dt = \\ = U_0(R) J_0(\Omega(R)). \qquad (2.44)$$

Due to the integral in (2.44), the term vanishes for all n except n=0. One should note, that the information about the phase of vibrations $\psi_0(R)$ is lost during the averaging process. The reconstructed intensity in the image plane (2.30) is expressed as:

$$I(R) = |U(R)|^2 = I_0(R) {J_0}^2\big(\Omega(R)\big), \qquad (2.45)$$

where I_0 denotes the intensity distribution of the holographically recorded object without presence of oscillation and can be considered unity[2].

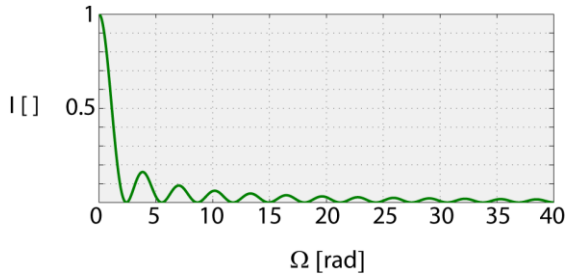

Figure 2.9: Square of the Bessel function modulates the intensity field in each pixel of the surface with respect to amplitude of vibrations.

From (2.45) it is obvious, that the value of vibration amplitude at each point R is encoded in intensity field as an argument of square of the Bessel function ${J_0}^2$. The graphical interpretation is introduced in Figure 2.9. Because there is a steady state at the nodes of the vibration modes, the intensity image exhibits the maximal intensity, ${J_0}^2(0) = 1$, in these points. Thus, the nodal lines can usually be identified. Furthermore there are dark fringes where ${J_0}^2\big(\Omega(R)\big) = 0$. Values at these points equal the arguments of the zeros of the zero-order Bessel function of

[1] A typical exposure time in time average digital holography is set to be $T \approx 1\,s$ while the period of the vibrations (100 Hz) starts at $\frac{2\pi}{\omega} \approx 0.01\,s$.

[2] In practice the reconstructed complex fields of oscillating object are multiplied by conjugate of complex field of non-oscillating object U_0 and dived by its envelope: $U_{norm}(R) = U(R){U_0}^*(R)/|U_0|$ in order to normalize the function. Unless stated otherwise, the normalized distributions without the subscript will be meant in further text. More detailed information about normalization and speckle suppression are given in chapter 3.5.

the first kind. These dark fringes act as contours of vibration amplitude map. Centers of these fringes are searched during the evaluation algorithm. The bright fringes between these zeros, which do not correspond to nodal lines, exhibit less intensity compared to the zero fringe. The simplest example is an out-of-plane vibrating surface in the z-direction $\boldsymbol{d}(R) = (0, 0, d_Z(R))$ that is perpendicularly illuminated $\boldsymbol{s}(R) = (0,0,-1)$ and observed $\boldsymbol{b}(R) = (0,0,1)$ with respect to the object surface. Thus the sensitivity vector becomes $\boldsymbol{e}(R) = 2\pi/\lambda(\boldsymbol{b}(R) - \boldsymbol{s}(R)) = (0,0,4\pi/\lambda)$ and the amplitudes at the centers of dark fringes are easily calculated by $d_Z = b_m\lambda/4\pi$ where b_m is the m-th zero of J_0.

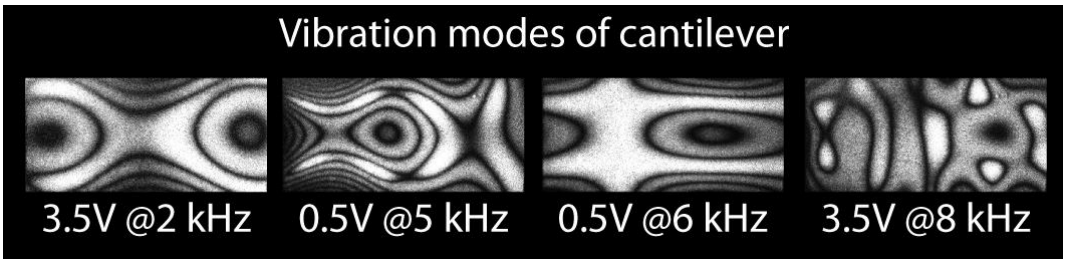

Figure 2.10: Intensity distributions reflecting vibration modes of the cantilever visualized by time average digital holography. The modes of the cantilever's vibrations strongly depend on driving frequency.

Some results obtained by time average digital holography are in Figure 2.10 and Figure 2.11. The beam cantilever from the example outlined in Figure 2.6 was driven by harmonic voltage signal with different magnitudes and frequencies. One should note that the holographical arrangement remains the same and only the ROI is displayed.

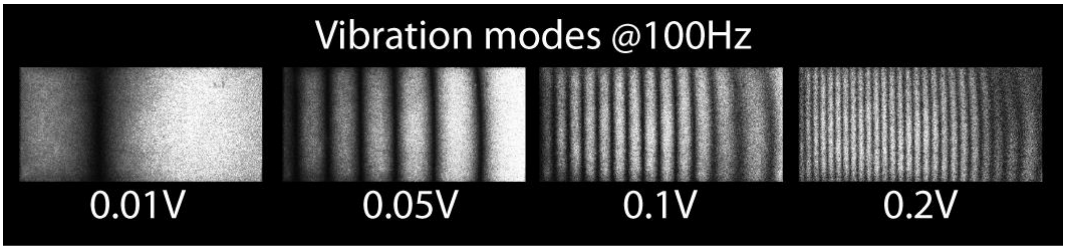

Figure 2.11: Intensity maps of oscillating cantilever at frequency 100 Hz obtained by time average digital holography. It holds that the greater supply voltage generates larger amplitudes of vibrations and thus the dark fringes are denser.

Although we can get a sense of an amplitude distribution from the intensity map, the aim of vibration analysis is to retrieve the amplitude distribution accurately at each point of the surface. The common algorithm for amplitude distribution retrieval from the intensity map usually consists of following steps:

- *Preprocessing of intensity field.* In order to automatically detect the nodal line and the dark fringes, a filtering of the intensity field is recommended [66]. Filtering helps to minimize the disturbances caused by e.g. varying background illumination, electronic noise, speckle, digitization and quantization or environmental distortions. Of special importance are the shading correction to compensate for uneven background intensity and the smoothing for suppressing the speckle influence.
- *Nodal lines and dark fringes skeletonizing.* This step comprises a search for a center of the bright fringes (skeleton), where the intensity becomes maximum – nodal line and for local extrema of the intensity distribution correspond to the maxima and minima of the Bessel function $J_0{}^2$. Usually only the dark fringes (local minima) are used but one can use local maxima as well. The methods for fringe skeletonizing can be divided into those based on fringe tracking, those related to segmentation, and others. Enhance the skeleton by linking together interrupted lines, by adding missing points, and by removal of artifacts, line crossings or interconnections.
- *Numbering of the skeleton.* It is important to define value of amplitude of oscillations to each line. The skeleton lines correspond to zeroes or local maxima of Bessel function $J_0{}^2$ are linked to amplitude distribution by formula $d_Z(R) = b_m \lambda/4\pi$, where b_m is the detected m-th zero of J_0. Generally, a continuous amplitude distribution of oscillation can be assumed, and therefore neighboring skeleton lines can differ in order b_m only by -1, 0, or $+1$, lines of different order must not intersect or merge, lines do not end inside the field of view etc. Automatic fringe numbering algorithms based on these constraints still usually require manual interaction by the user.
- *Interpolation of remaining pixels.* After assignment of the amplitude value to each skeleton line, the values are only known along these lines, which represent a rather irregular distribution of points. To determine the values at all points of a regular grid, the values of amplitude have to be interpolated for the grid points based on the amplitude values at the skeleton lines. Interpolation can be based on one-dimensional splines, by bilinear interpolation or interpolation by triangulation.

At first sight it is clear, that the amplitude retrieval from intensity map is uncomfortable, time consuming procedure, which generally cannot be performed automatically. This is one of the biggest drawbacks of time-average digital holography.

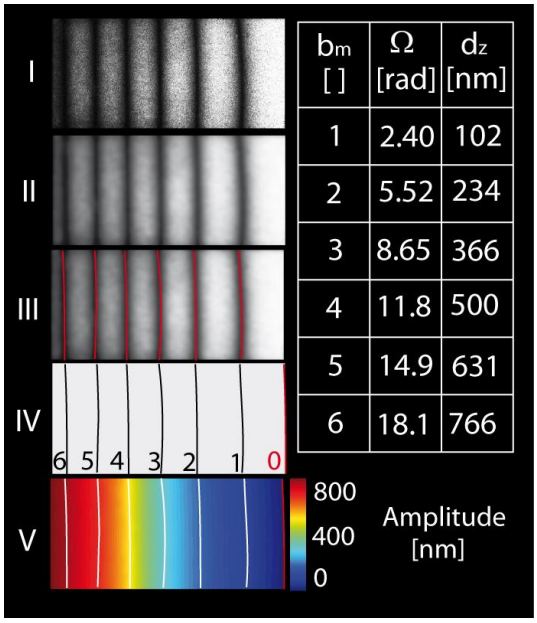

Figure 2.12: Data flow chart of the conventional algorithm for amplitude map retrieval: I-raw data, II-filtered intensity field, III-detection of dark fringes and the nodal line, IV-numbering of the fringes and linking with corresponding value of amplitude from the table, V-interpolation of remaining pixels.

As aforementioned, time average digital holography is used to measure the amplitude distribution of harmonically oscillating object. The range of measureable amplitudes by the method is limited from the both sides.
In order to examine sensitivity of time average holography for small amplitudes, we can rewrite the Bessel functions as the power series:

$$J_n(\Omega) = \sum_{i=0}^{\infty} (-1)^i \Omega^{n+2i} / \left(2^{n+2i} i!\,(n+i)!\right) \qquad (2.46)$$

for $|\Omega| < \infty$. For very small amplitudes when Ω in the formula (2.46) approaches zero, $\Omega \to 0$, the sensitivity of time average method is also approaching zero:

$$\lim_{\Omega \to 0} \frac{dJ_0}{d\Omega} = 0. \qquad (2.47)$$

In practice, for very small amplitudes bellow approximately 30 nm we obtain more or less uniformly distributed intensity map as can be seen in Figure 2.13 (left). Moreover, the reliability of the algorithm for amplitude evaluation based on

fringe skeletonizing followed by interpolation naturally depends on the density of known amplitude values on a distribution of a regular grid. The more values we know, the more reliable and robust is the interpolation procedure. For small amplitudes there are only few dark fringes in the intensity field (see Figure 2.11 – an actuator is driven by only 0.01 V). Interpolation of such a poor data distribution is always a subject of questionable accuracy and strongly depends on modes shape and parameters of the interpolation procedure.

Measurement of large amplitudes is also limited. As the amplitude of vibrations (to be more precise slope of the amplitude) increases, the density of dark fringes in the intensity map also increases, see Figure 2.11. For large amplitudes, an asymptotic formula $I = {J_0}^2(\Omega \to \infty) \approx cos^2(\Omega - \pi/4)$ can be used for simplification. When the illumination and observation direction of the object are parallel, the argument of the Bessel function becomes $\Omega = (4\pi/\lambda)d_Z$. Considering the asymptotic formula, the phase change between two adjoining dark fringes[1] $\Delta\Omega = \pi$ corresponds to amplitude change of $\Delta d_Z = \lambda/4$. In order to follow sampling criterion, at least two samples must lie within one period of the signal and therefore a change of amplitude between two consecutive points cannot be larger than $\lambda/8$.

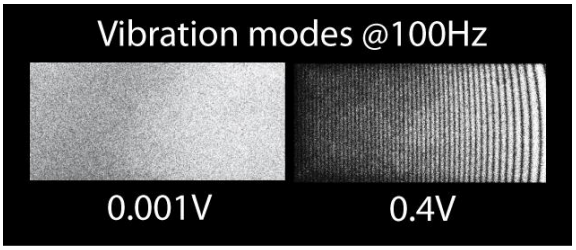

Figure 2.13: Limits of time average digital holography: (left) for very small amplitudes of vibrations the intensity distribution is almost even; (right) for large amplitudes of vibrations the high density fringe pattern with low contrast is unresolvable.

Theoretically, the sampling distance between the two consecutive points is given by pixel extension in image plane (2.18). In practice, size of speckles acts as the smallest resolvable element in the reconstructed field. If we reconstruct using the Fresnel transform, the speckles cover approximately two pixels[2], which tightens the maximal change of amplitudes between two neighborhood pixels in

[1] period of the fringe pattern $I \approx cos^2(4\pi d_Z/\lambda - \pi/4)$

[2] Speckle size in reconstructed image plane $s = \frac{\lambda d\pi}{2N\Delta\xi}$ (when compared to (2.18)) results in $s = \frac{\pi}{2}\Delta x \sim 2\Delta x$.

image plane to be $\lambda/16$. An example of intensity distribution with high fringe density is in Figure 2.13 (right). More than 40 dark fringes can be counted over the object surface. Such intensity map corresponds to amplitude distribution with maximal value of approximately $5\ \mu m$.

3 Extension of measurement capabilities of time average digital holography

3.1 Employment of acusto-optical modulators in holographic arrangements

An acusto-optical modulator uses the interaction of a column of traveling acoustic waves with an incident coherent optical beam to modulate the properties of the transmitted optical wavefront. The modulator consists of a transparent medium into which acoustic waves can be coupled from a piezoelectric transducer. The transducer is driven by a radio frequency (RF) source, which introduces periodical compressions of the acoustic medium. The acoustic wave propagates in the medium through small local displacements of molecules leading to strain in the medium. Associated with these strains are small changes of the local refractive index, a phenomenon known as the acousto-optic or the photo-elastic effect.

The driving voltage ranges in the radio frequency spectrum that is centered at a certain center frequency f_0, with a bandwidth B about that center frequency. For a perfectly sinusoidal drive voltage of frequency f_{mod} the transducer launches a sinusoidal traveling acoustic wave in the cell, which moves with the acoustic velocity v. This traveling wave induces a moving sinusoidal phase grating with period $\Lambda = v/f_{mod}$, which interacts with the incident optical wavefront. There are two different regimes of the acousto-optic interaction: the Raman-Nath regime and the Bragg regime.

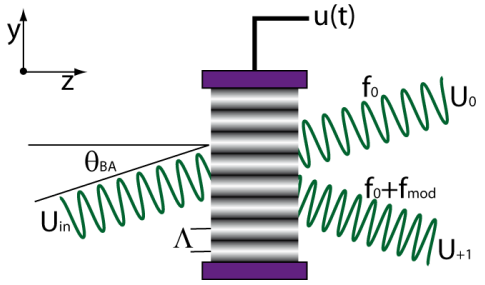

Figure 3.1: Acusto-optical modulator in Bragg regime – Bragg cell.

In Bragg regime, which is the subject of our concern, the RF frequencies are in the hundreds of MHz to the GHz range. Acoustic media consists of crystals and the thickness of the acousto-optic column compared with the acoustic wavelength introduces a preferential weighting for certain diffraction orders, and suppresses

others. This effect is known as the Bragg effect. The dominant diffraction orders in Bragg regime are the zero order and the single first order. Strong diffraction into a first diffraction order occurs only when the angle of the incident beam having the wavelength $\lambda = c/f_0$, satisfies Bragg angle θ_{BA} with respect to plane of the acoustic wavefronts:

$$sin\theta_{BA} = \frac{\lambda}{2\Lambda} \tag{3.1}$$

The optical frequency of the 1st diffraction order can be determined from the Doppler-shift relation:

$$f_1 = f_0\left(1 + \frac{v}{c}\right) sin\theta_{BA} \approx f_0 + f_{mod}. \tag{3.2}$$

Thus the optical frequency of the 1st diffraction order is translated by the driven frequency f_{mod}.

Until now the voltage driving the acousto-optic cell has been assumed to be a perfect continuous wave (CW) signal. However, phase or amplitude modulation of driven voltage has a great importance for time average digital holography as will be shown. Generally, the driving voltage can be an amplitude and phase-modulated CW signal, of the form

$$u(t) = A(t)sin(2\pi f_{mod}t - \phi(t)), \tag{3.3}$$

where $A(t)$ and $\phi(t)$ are the amplitude and phase modulations, respectively. The refractive index disturbance generated by this applied voltage then propagates through the cell with velocity v:

$$\Delta n(y,t) = Cu(t-\tau), \tag{3.4}$$

where C is a proportionality constant, $\tau = t_0 - y/v$ is the total time delay and time delay $t_0 = L/2v$ is required for acoustic propagation over half the length of the cell. The optical wavefront is simply phase modulated by the moving refractive index grating, yielding complex amplitude of the transmitted signal given by

$$U_0(y,t) = U_{in}exp\left(j\frac{2\pi dC}{\lambda}A(t-\tau)sin[2\pi f_{mod}(t-\tau) - \phi(t-\tau)]\right), \tag{3.5}$$

where U_{in} is the complex amplitude of the incident monochromatic optical wave. After some operations [58] one obtain also the complex amplitude transmitted into the first diffraction order:

$$U_{+1}(y,t) = \frac{\pi dC}{\lambda} U_{in} A(t-\tau) exp\left(-j\phi(t-\tau)\right) \times \\ \times exp\left(j\frac{2\pi y}{\Lambda}\right) exp(j2\pi f_{mod}(t-t_0)). \tag{3.6}$$

Thus the acousto-optic cell transforms an electrical voltage modulation applied to the cell into an optical wavefront.

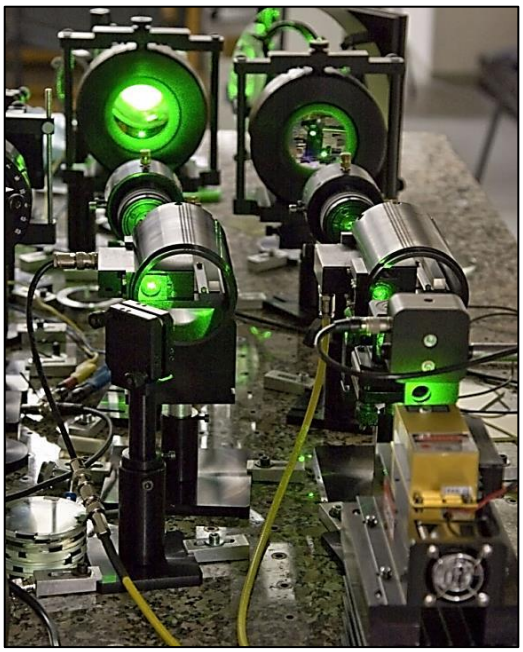

Figure 3.2: Bragg cells employed in a real experimental arrangement.

Introducing Bragg cells into the both arms of a holographical arrangement, as illustrated in Figure 3.3, we can take advantage of the frequency and phase modulation generated by the Bragg cells in order to extend measurement capabilities of time average digital holography.

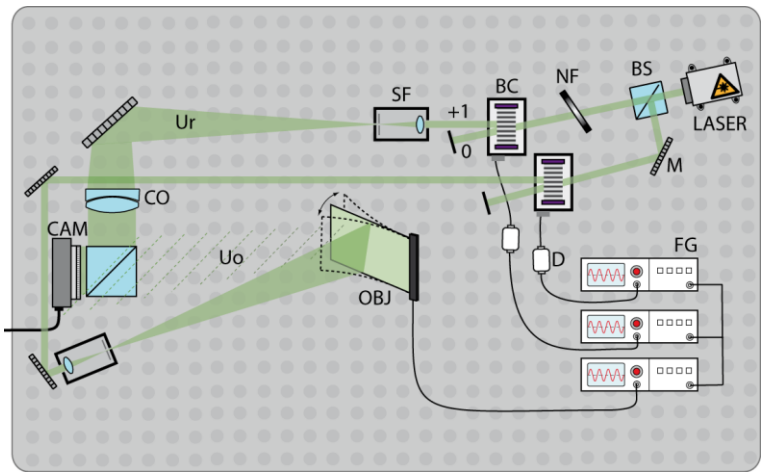

Figure 3.3: Principal scheme of an experimental arrangement for time average digital holography measurement with the employment of Bragg-cells (BC).

The object wave U_o and the reference wave U_r are further modulated by the acousto-optic cells placed in the object and the reference arm U_{BCo}, U_{BCr} in compliance with equation (3.6). The interference formula (2.1) for recording of digital hologram becomes more general:

$$h \approx |U_o U_{BCo} + U_r U_{BCr}|^2 = \\ = |U_o U_{BCo}|^2 + |U_r U_{BCr}|^2 + U_o U_{BCo} U_r{}^* U_{BCr}{}^* + U_o{}^* U_{BCo}{}^* U_r U_{BCr}. \quad (3.7)$$

and parameters of the modulation (A, ϕ, f_{mod}) influence properties of the reconstructed wave field (2.3).

3.2 Improvement of lateral resolution and SNR by heterodyne interferometry

The reconstructed optical field propagating behind hologram consists of three different diffraction orders as derived in formula (2.3). However, only the real image represented by term $I_r U_0$ carries the required information. The remaining terms act only as a disturbing signal. The more detailed discussion is given in chapter 2.3. Angle ϑ between the object wave and the plane reference wave $U_r = exp(-jkx\, sin(\vartheta))$ defines the mutual location of the real image, the virtual image and the d.c. term in the image plane. The limiting value $\vartheta = 0$ leads to in-line holography where all the terms overlap each other.

For further analysis it is illustrative to examine the reconstructed field behind the hologram in its spectral domain. Considering $\mathcal{U}_r, \mathcal{U}_o$, and $\mathcal{H}$ to be Fourier images of U_r, U_o, and h, formula (2.3) can be rewritten as:

$$\mathcal{H} \approx (\mathcal{U}_r + \mathcal{U}_o) * (\mathcal{U}_r{}^* + \mathcal{U}_o{}^*) = \\ = \mathcal{U}_r \star \mathcal{U}_r + \mathcal{U}_o \star \mathcal{U}_o + \mathcal{U}_o * \mathcal{U}_r{}^* + \mathcal{U}_o{}^* * \mathcal{U}_r, \quad (3.8)$$

where symbols $*, \star$ denote convolution and correlation, respectively. The spectrum of the plane reference wave, which is represented by the Dirac δ-function,

$$\mathcal{U}_r = \mathcal{F}\{U_r\} = \delta(f - f_c) \quad (3.9)$$

is shifted in the spectral domain about the carrier frequency $f_c = \frac{sin(\vartheta)}{\lambda}$. Substituting (3.9) into (3.8) and using identity $\delta * g = g * \delta = g$ for any g, formula (3.8) becomes:

$$\mathcal{H} \approx \delta \star \delta + \mathcal{U}_o \star \mathcal{U}_o + \mathcal{U}_o * \delta + \delta * \mathcal{U}_o{}^* = \delta + \mathcal{U}_o \star \mathcal{U}_o + \mathcal{U}_o + \mathcal{U}_o{}^*. \quad (3.10)$$

Graphical interpretation of (3.10) is shown in Figure 3.4.

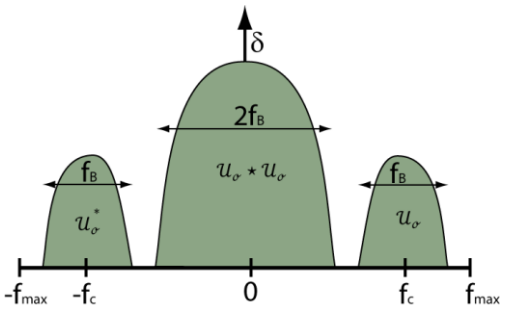

Figure 3.4: 1D outline of spectral domain of an off-axis digital hologram.

The central part of the hologram spectrum is known as the autocorrelation term (d.c. term). Its size is associated with the highest spatial frequencies of the object f_B, which is determined by the largest lateral dimension of the object d_0 and the distance d between the object and the detector: $f_B = \frac{d_0}{d\lambda}$. The real image $\mathcal{U}_o$ and the twin image $\mathcal{U}_o{}^*$ are twice as small as the autocorrelation term. The separation of the terms in spectral domain is driven by the carrier frequency f_c that is directly affected by angle of the reference wave ϑ. From one side, the maximal value of ϑ is limited by Nyquist frequency $f_c < f_{max} = \frac{1}{2\Delta\xi}$, se formula (2.5). On contrary, the individual terms cannot overlap each other and therefore the carrier frequency must be sufficiently great: $f_c > 1.5 f_B = 1.5\frac{d_0}{d\lambda}$. Even though the carrier frequency is set to be optimal, the width of spectrum belonging to useful information $\mathcal{U}_o$ is restricted to approximately one fourth of the total spectrum width $\langle -f_{max}, f_{max} \rangle$.

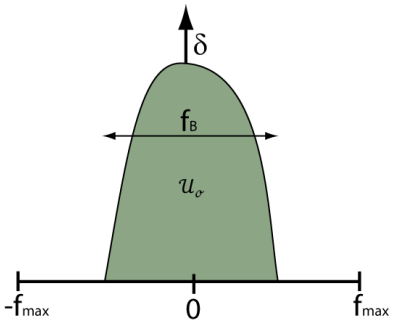

Figure 3.5: 1D outline of an in-line digital hologram that is free of the d.c. term and the twin image.

To improve the reconstruction quality and lateral resolution, d.c. term and twin image terms have to be canceled. Once the undesired terms in the spectrum are suppressed, we can set $f_c = 0$ in the manner of in-line digital holography and bring the object closer to the detector. Thus the bandwidth of the object widens, which results in improvement of the lateral resolution in image plane according to formula (2.18). Obviously, the noise in the hologram or image plane generated by

contributions from the d.c. term and the virtual image is also suppressed, which enhances signal-to-noise ratio (SNR).

The suppression of the d.c. term and the virtual image can be achieved by so called phase-shifting technique, where the complex field in hologram plane is calculated from at least three digital holograms with a mutual phase shift in the reference wave. The calculated complex field represents only the contribution from the real image and thus is free of the virtual image and the d.c. term.

Let us again consider the recorded field in the hologram plane. Substituting the plane reference wave $U_r = |U_r|$ and the object wave $U_o = |U_o| exp(-j\varphi_o)$ into (2.1), the formula becomes:

$$h \approx |U_r|^2 + |U_o|^2 + 2|U_r||U_o| \cos(\varphi_o) \qquad (3.11)$$

or in the general form:

$$h \approx a + b \cos(\varphi_o), \qquad (3.12)$$

where the additional term $a = |U_r|^2 + |U_o|^2$ is average intensity of the hologram and the multiplicative term $b = 2|U_r||U_o|$ expresses intensity modulation.

The aim is to calculate the complex field of the object wave $U_0 = |U_o| \exp(-j\varphi_o)$, that is obviously proportional to the real image. The magnitude $|U_o| = \sqrt{I_o}$ can be easily measured; however, $|U_o|$ acts only as a normalization factor and therefore can be set unity. The unknown phase field φ_o must be calculated accurately. The formula (3.12) contains three unknowns variables and therefore not a single, but at least three digital holograms with well-defined phase shifts $\Delta\varphi$ introduced into the reference beam or the object beam must be captured. This leads to set of N equations:

$$h_i \approx a + b \cos(\varphi_o + \Delta\varphi_i), \qquad (3.13)$$

where i denotes an integer $i = 1,2,3, \dots N$. The unknown phase φ_o can be directly calculated as a solution of the set of equations. One should note, that phase of the object field is a spatial function $\varphi_o(\xi, \eta)$, whereas the phase shift $\Delta\varphi_i(t)$ is a temporal function. For temporal varying phase shift, the intensity at each point of the digital hologram varies as a function of the introduced phase shift $\Delta\varphi_i$ with a temporal offset φ_o given by the unknown wavefront phase. If the hologram is viewed during the phase shifting operation, the fringe pattern will appear to move across the field. The phase shift is usually realized by an employment of a mirror

mounted on a piezoelectric transducer into the reference arm. The optical path difference generated by the mirror slight movement introduces the required phase shift. However, the piezoelectric transducer is not perfectly linear, requires calibration, etc. [67]. In order to suppress most of the phase shift errors, one can replace the phase shift generated by piezoelectric transducer movement by a frequency shift induced by Bragg cells.

The holographical arrangement is illustrated in Figure 3.3. The Brag cell in the reference arm and the object arm is driven by sinusoidal voltage of frequency f_{R-mod} , f_{O-mod}, respectively. From equation (3.2) it follows that the beams are temporally modulated by frequency $\omega_r = 2\pi(f_0 + f_{R-mod})$, respectively, $\omega_O = 2\pi(f_0 + f_{O-mod})$, where f_0 is working RF frequency of the Bragg cells. If $\omega_R \neq \omega_O$, the frequency shift in one of the interfering light waves can be envisaged as a continuous shift of the mutual phase between the light waves:

$$h \approx a + b\,cos(\varphi_o + (\omega_O - \omega_R)t). \qquad (3.14)$$

The intensity at each point of the digital hologram varies as a sinusoidal function with the beat frequency $\omega_B = 2(\omega_O - \omega_R) = 2\Delta\omega$. The interference of two optical waves of different frequencies is a basis of so called heterodyne technique. We need to sample the temporal varying digital hologram with required phase shift $\Delta\varphi_i$ in order to substitute these values in (3.13). The inherent temporal sampler in digital holography is a digital sensor via its frame rate FPS. The relative phase shift $\Delta\varphi$ between two consecutive digital holograms is:

$$\Delta\varphi(\Delta\omega) = \varphi(t) - \varphi\left(t + \frac{1}{FPS}\right) = (\omega_O - \omega_R)\frac{1}{FPS} = \frac{\Delta\omega}{FPS}. \qquad (3.15)$$

Formula (3.15) shows that we can generate arbitrary phase shift $\Delta\varphi$ between frames h_i and h_{i+1} by driving the frequency of Brag cells. This can be favorable used for a solution of the set of equations defined in (3.13). An example of such a heterodyne detection is illustrated in Figure 3.6. The plots show how intensity in one pixel of hologram varies in time during the heterodyne detection. The blue points are sequences of intensity values captured by digital camera with frame rate $FPS = 6.5\,Hz$ at different beat frequencies $\Delta\omega$. The green line represents theoretical curve as derived in (3.14). It was verified, that the frequency difference $\Delta\omega$ drives the phase shift between two consecutive holograms according to (3.15).

Although a broad spectrum of phase-shifting algorithms have been developed and described [68] (having e.g. different sensitivity to sources of error), the most

straightforward approach is a four step algorithm. The four step algorithm requires that four separate digital holograms are recorded.

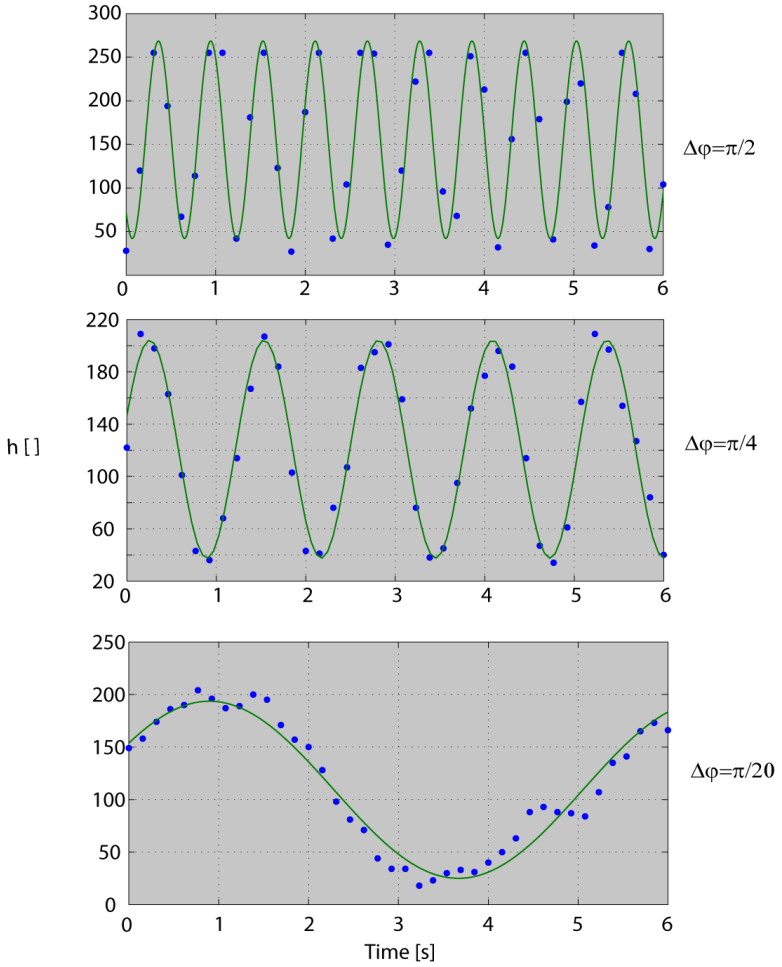

Figure 3.6: Intensity variation (blue points) in time within one pixel of captured digital holograms. The green line is fitted cosine function. Different frequencies of reference and object wave generated by the Bragg cells enables heterodyne detection with easy controllable phase steps between two consecutive frames.

An optical phase shift $\Delta\varphi = \pi/2$ is introduced between each of the sequentially recorded holograms in the manner of (3.15). For digital camera used in our experimental setup with $FPS = 6.5\,Hz$, the frequency difference must be set to $\Delta f = 1.625Hz$. Since these are now discrete measurements, the frequency difference dependence $\Delta\varphi(\Delta\omega)$ has been changed to the phase step index i. The function $\Delta\varphi_i$ now takes on four discrete values: $\Delta\varphi_i = 0, \pi/2, \pi, 3\pi/2$ for $i = 1,2,3,4$. Substituting each of these four values into (3.13) results in four equations describing the four measured digital holograms:

$$h_1 \approx a + b\,cos(\varphi_o), \qquad (3.16)$$

$$h_2 \approx a + b\,cos\left(\varphi_o + \frac{\pi}{2}\right) = a - b\,sin(\varphi_o), \tag{3.17}$$

$$h_3 \approx a + b\,cos(\varphi_o + \pi) = a - b\,cos(\varphi_o), \tag{3.18}$$

$$h_4 \approx a + b\,cos\left(\varphi_o + \frac{3\pi}{2}\right) = a + b\,sin(\varphi_o). \tag{3.19}$$

These four equations in three unknowns a, b, φ_o can be solved at each point of the digital hologram. The intensity bias term a is eliminated by subtracting the equations in pairs:

$$h_1 - h_3 = 2bcos(\varphi_o), \tag{3.20}$$

$$h_4 - h_2 = 2bsin(\varphi_o). \tag{3.21}$$

The complex field of the object wave can be written in a form: $U_o = |U_o| \exp(-j\varphi_o) = |U_o|\big(\cos(\varphi_o) - jsin(\varphi_o)\big)$, and thus

$$U_o = A\big((h_1 - h_3) - j(h_4 - h_2)\big), \tag{3.22}$$

where A is only a normalization factor $A \approx 1/4|U_r|$ and can be omitted. In the last step, the intensity field recorded by digital camera (digital hologram) h can be replaced in reconstruction formulas (2.19), (2.22), (2.25), (2.29) by the complex field of object wave in the hologram plane U_0 and the reconstructed field in image plane is free of the undesired terms. A deeper analysis of the example mentioned in chapter 2.3 is provided in the next paragraph.

For a recapitulation, the object is a steady beam cantilever of the width $d_{0-x} = 49\,mm$ and the height $d_{0-y} = 21\,mm$. The cantilever is located at the distance $d = 600\,mm$ apart from the sensor. The sensor is a CMOS having number of pixels $N = M = 2048\,pix$ with pixel extensions $\Delta\xi = \Delta\eta = 3.45\,\mu m$. Laser emits light of the wavelength $\lambda = 532\,nm$. The digital hologram introduced in Figure 2.7 is a result of superposition between a reference plane wave and the object wave scattered from the object. A spectral domain of such a digital hologram, theoretically described by formula (3.10), is introduced in Figure 3.7 left. Note, that Figure 3.4 outlines the same spectral information in 1D. False colors in Figure 3.7 represent magnitude of the complex field in a logarithmic scale. The real image $\mathcal{U}_o$ covers only a small part of the spectral region. The carrier

frequency $f_{c-\eta}$ is particularly introduced in the vertical direction in which the object has the frequency bandwidth $f_{B-\eta} = \frac{d_{0-y}}{d\lambda} = 66\ mm^{-1}$.

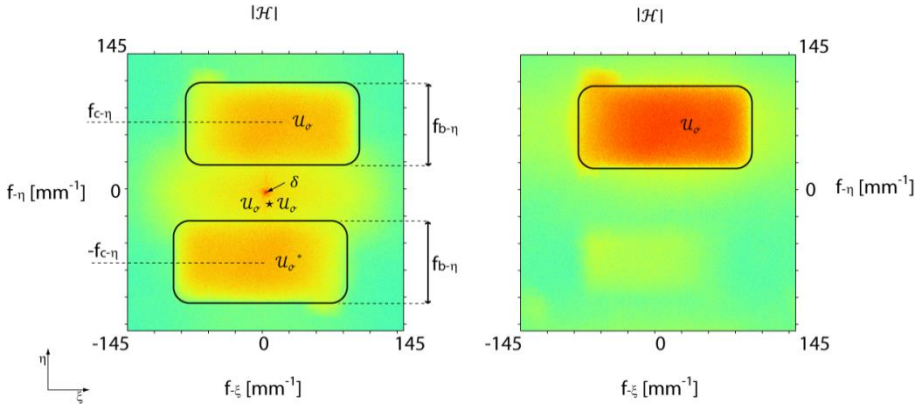

Figure 3.7: Spectral domain of off-axis digital hologram without (left) and with (right) phase shifting technique. False colors represent magnitude of the spectrum in a logarithmic scale.

The real image and the autocorrelation term $\mathcal{U}_o \star \mathcal{U}_o$ are not completely separated since $f_{c-\eta} < 1.5 f_B$, which results in lower but acceptable SNR in the region belonging to the real image. Field in the hologram plane is propagated by means of Fresnel transform to image plane, see Figure 3.8 left. The field in the image plane is mirrored with respect to the field in the hologram plane due to Fourier transformation included in Fresnel transform.

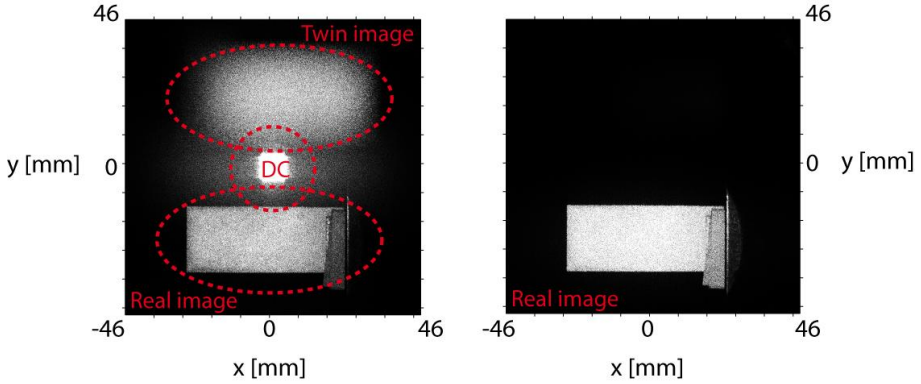

Figure 3.8: Reconstructed intensity field in image plane in case of off-axis arrangements without (left) and with (right) phase shifting technique.

Using the phase-shifting approach one can suppress the undesired terms in equation (3.10). The Bragg cell in the object arm is only modulated by angular frequency $\omega_o = 2\pi f_O$ with its working RF frequency $f_O = 40MHz$. The reference arm Bragg cell is in addition modulated by frequency $f_{r-mod} = FPS/4 = 1.625Hz$ in order to have heterodyne technique with phase shifts between holograms $\Delta\varphi = \pi/2$: $\omega_r = 2\pi(f_0 + f_{r-mod})$, see Figure 3.6 (very top plot). A sequence of four digital

holograms corresponding to (3.16)-(3.19) was captured and processed by formula (3.22). The calculated magnitude spectrum, see Figure 3.7 right, bears particularly information about the real image while the twin image and the autocorrelation term (d.c. term) are strongly suppressed. The false colors are again magnitudes of the complex field in the same logarithmic scale as in the left sub figure. The improvement of SNR in case of phase-shifting technique is clearly seen. Reconstructed intensity distribution in the image plane, which is the main subject of concern, is then shown in Figure 3.8 right.

The power of the real image signal[1] η with $N_{\mathcal{U}_o}$ elements defined as $\eta = \sum_{f_b} |\mathcal{U}_o(f_b)|^2 / N_{\mathcal{U}_o}$ is about 30% better in case when phase-shifting technique is employed, which helps to improve the recovered information and makes the time average holography more sensitive (as will be discussed hereinafter).

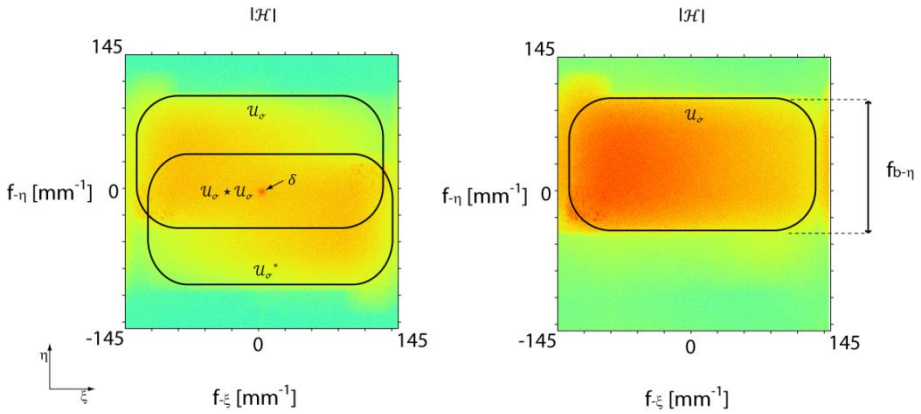

Figure 3.9: Spectral domain of in-line digital hologram without (left) and with (right) phase shifting technique. False colors represent magnitude of the spectrum in a logarithmic scale.

In the next step one can place the object closer to digital sensor in order to improve the lateral resolution. If the object is $d = 350\,mm$ apart from the digital sensor, the bandwidth of the object increases to $f_{B-\eta} = 121 mm^{-1}$. The bandwidth of the object in horizontal direction $f_{B-\xi} = 263\,mm^{-1}$ approaches the maximum bandwidth $f_{max} = 290\,mm^{-1}$ determined by sampling criterion (2.5). Therefore, $d = 350\,mm$ is almost the minimal possible distance between the object and the CMOS. Naturally, lack of carrier frequency leads to mutual overlapping of all the terms (3.10) in spectral domain of the digital hologram, as it is obvious from Figure 3.9 left. A reconstruction of such a hologram leads to noisy intensity field, see Figure 3.10 left. However, if the phase-shifting technique is employed,

[1]The power spectrum η can be regarded as a diffraction efficiency of a diffraction grating at certain spatial frequency.

disturbing terms in hologram plane are suppressed; see Figure 3.9 right, and thus the reconstructed field in image plane evinces good quality. Moreover, the object is reconstructed almost over the whole image plane maximizing the lateral resolution.

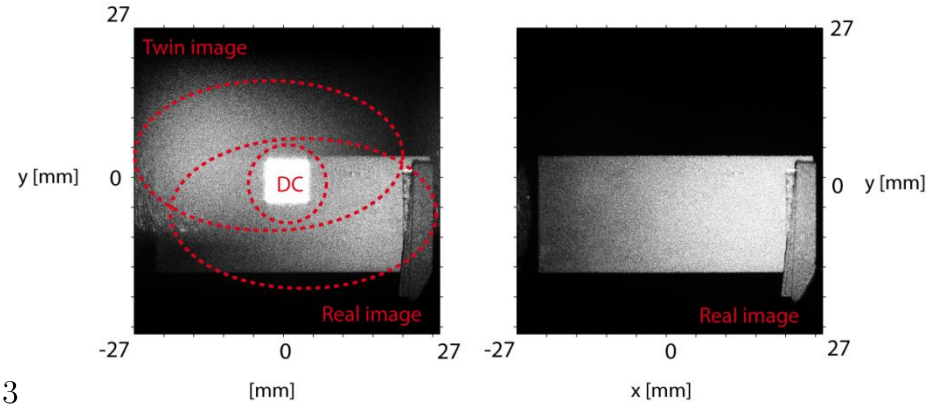

Figure 3.10: Reconstructed intensity field in image plane in case of in-line arrangements without (left) and with (right) phase shifting technique.

3.3 Extension of dynamic range by means of frequency modulation

The dynamic range of measurable amplitudes by time average digital holography was estimated to be in the range starting from approximately 100 nm to few microns, see chapter 2.4. For smaller amplitudes the first limiting factor is the amplitude retrieval by interpolation of a sparse array of known values. This limit is just a subject of calculation, however, when approaching zero (order of nm), the sensitivity of time average method decreases and falls to zero, see (2.47). The upper bound is limited to situation where fringes in the intensity field can be counted. Otherwise, it becomes difficult to count many narrow fringes, and even impossible when they are smaller than the optical resolution. Frequency modulation introduced in one of the arm can address the above mentioned problem and shift the limits of time average holography.

Let´s start with arrangement shown in Figure 3.3. Oscillating object modulates phase of the object wave in the same manner as described in (2.39). Applying a sinusoidal signal with frequency $f_0 + f_{R-mod}$ to the Bragg cell placed in reference arm results, according to expression (3.2), in frequency modulation of the reference wave: $U_{BCr} = exp(j2\pi(f_0 + f_{R-mod})t) = exp(j(\omega_0 + \omega_{R-mod})t)$. As will be demonstrated, it is advantageous when the reference wave is modulated by an

integer multiple $\omega_{R-mod} = m\omega$ of the object vibration frequency ω. For simplicity, the object wave is modulated only with working frequency $\omega_0 = 2\pi f_0$: $U_{BCo} = exp(j\omega_0 t)$.

The interesting third term of (3.7) describes the complex amplitude of a wave field proportional to:

$$U_{real}(R,t) \approx \int_0^T U_o U_{BCo} {U_r}^* {U_{BCr}}^* \, dt = \\ = \int_0^T exp(j\Omega(R)\, sin[\omega t + \psi_0(R)])\, exp(-jm\omega t)\, dt, \tag{3.23}$$

where for plane reference wave holds ${U_r}^* = 1$. Proportionality factors influencing only the overall brightness have been omitted for convenience. Further steps are identical with those in the chapter 2.4 with exception of the presence of the frequency modulation. Using expression (2.42) and applying time averaging, formula (3.23) becomes:

$$U_{real}(R,t) \approx \lim_{T\to\infty} \sum_{n=1}^{\infty} J_n\big(\Omega(R)\big) \int_0^T exp(jn[\omega t + \psi_0(R)]) \times \\ \times\, exp(-jm\omega t)\, dt. \tag{3.24}$$

All terms of sum in (3.24) except for $n = m$ are canceled due to time averaging and thus the magnitude[1] of the reconstructed real image:

$$|U(R)| \approx \big|J_m\big(\Omega(R)\big)\big|. \tag{3.25}$$

is modulated by m-th order Bessel function. In conclusion, controlling the frequency shift of reference (or object) wave about integer multiple of the object vibration frequency allows for control of order of the Bessel function modulating the resulting intensity field. This result is consistent with the unmodulated time average case where $m = 0$.

Time-average holography with frequency modulation can be used to increase the sensitivity for vibrations with small as well as with large amplitudes. Small amplitudes are such that the interference phase $\Omega(R) \ll 1$.

In time average holography with no modulation, the magnitude of reconstructed field $|U| \approx |J_0(0)|$ is unity and has zero slope (2.47). On the other hand when $m=1$, $|U| \approx |J_1(0)|$ has a positive slope in the dark field:

[1] Using magnitude distribution instead of intensity distribution (2.45) brings better sensitivity of the measurements since $\lim_{\Omega\to 0} \frac{d{J_m}^2}{d\Omega} = 0$ for all m. Notice, the classical (not digital) time average holography has only access to the intensity distribution, which is another disadvantage of classical approach.

$$\lim_{\Omega \to 0} \frac{dJ_1}{d\Omega} = 0.5 \qquad (3.26)$$

yielding visible intensity variations even for small amplitudes.

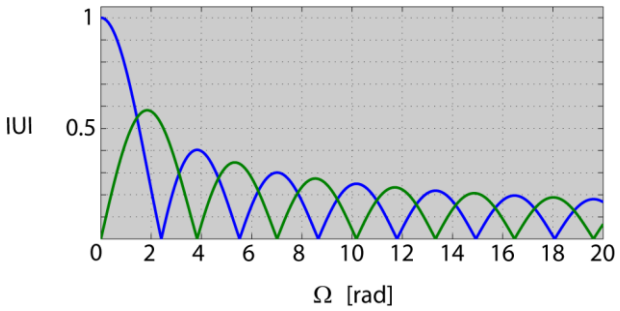

Figure 3.11: Magnitude of zeroth order (blue) and first (green) Bessel function.

The following experiment comprises two aims. The first aim is to verify validity of the formula (3.25). The second aim is to compare sensitivity of frequency modulated with frequency non-modulated time average digital holography for small amplitudes. The experiment was conducted with oscillating cantilever at frequency $f = \omega/2\pi = 6000\,Hz$ supplied with different values of voltage. Properties of such a cantilever require linear behavior in every single pixel: increasing supplying voltage u leads to proportional increase of maximal amplitude of vibrations $d_Z = C_v u$ with proportional constant C_v. The experimental arrangement is outlined in Figure 3.3. Starting with non-modulated measurement; the both Bragg cells were only driven by harmonic signal with working RF frequency $f_o = f_r = f_0 = 40\,MHz$. Therefore frequency of the both wavefronts is shifted about the same value f_0 and no frequency modulation is employed. A set of ten digital holograms with different supplying voltages was captured and reconstructed using the Fresnel transform. The magnitude of the reconstructed complex field in image plane $|U_{J0}| \approx \left|J_0\left(\frac{4\pi}{\lambda} C_v u\right)\right|$ holds for arrangements with sensitivity vector $\boldsymbol{e} = (0, 0, 4\pi/\lambda)$ in (2.38). The reconstructed magnitude images are introduced in the left column of the black frame in Figure 3.12. The very top image represents magnitude distribution measured at supply voltage $u = 0.05\,V$. Lower images show how the magnitude distributions vary with increasing voltage of step $\Delta u = 0.05\,V$ up to $u = 0.5\,V$. As expected, higher voltage applied on the cantilever results in its larger vibration amplitudes and growing number of dark fringes in the magnitude field.

The same procedure except the Bragg cells driven signal settings was repeated for frequency modulated time average holography. In this case, the Bragg cell in reference arm was driven by harmonic signal having frequency $f_r = f_0 + f_{R-mod} = f_0 + mf$, where $m = 1$ and thus $f_r = 40.006\,MHz$. The wavefront of the object wave remains modulated only at working frequency $f_o = f_0 = 40\,MHz$. Resulting magnitude distributions $|U_{J1}| \approx \left|J_1\left(\frac{4\pi}{\lambda} C_v u\right)\right|$ are modulated by 1st order Bessel function and organized with the same logic as in previous case in the right column of the black frame in Figure 3.12. Similarly we can observe the growing number of dark fringes when the supply voltage increases.

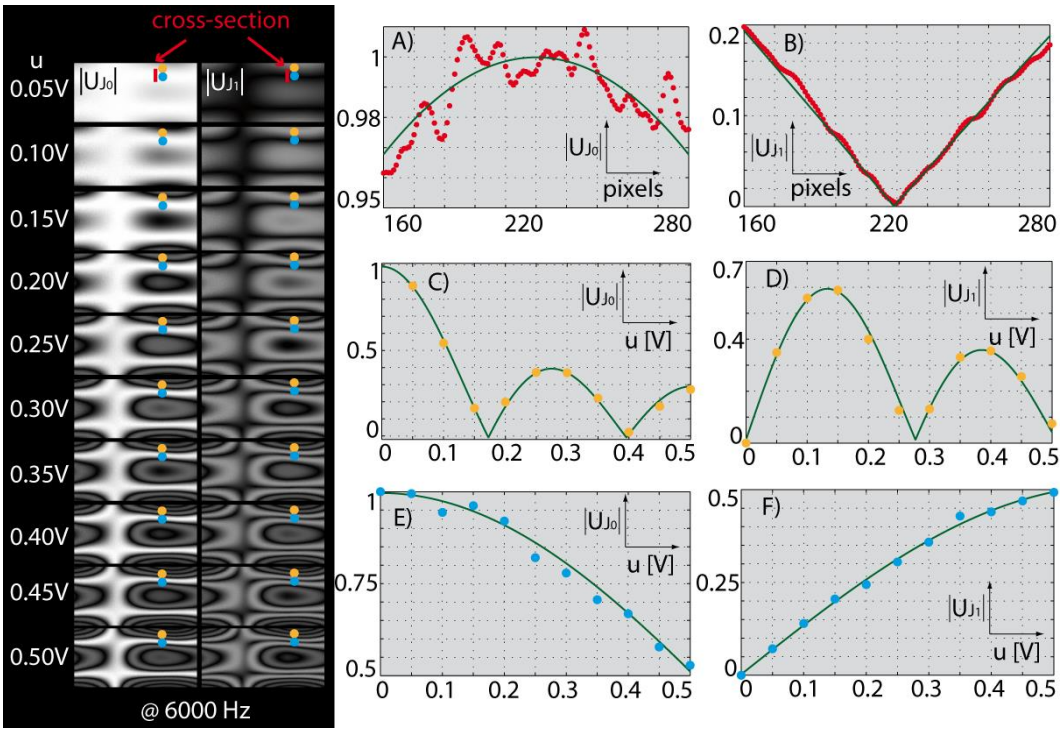

Figure 3.12: (black frame) Impact of frequency modulation on magnitude maps when increasing the supply voltage; (A, B) Measured values (red points) and theoretical values (green line) along cross-section denoted by the red line in magnitude map for 0.05V. Left plot (A) stands for non-modulated holography, where the sensitivity and SNR is obviously lower when compared to modulated technique introduced in the right plot (B); (C, D, E, F) As the supply voltage increases, the magnitude in each pixel varies. Magnitude variations at two pixels denoted by orange and blue circle were investigated in detail and compared to theoretical curves (green line). This was done for non-modulated (C, D) as well as modulated (D, F) technique.

Two representative pixels from the magnitude distributions were picked for further analysis. The first pixel denoted by an orange circle ("orange point") is relatively far from the nodal line, while the second pixel denoted by a blue circle ("blue point") is closer. Since the orange point is far from the nodal line and so closer to antinode, the amplitude of vibration is more sensitive to supply voltage

than in case of the blue point. The development of magnitude distributions $|U_{J0}|$ and $|U_{J1}|$ as a function of the supply voltage are plotted in the middle and down plots in Figure 3.12.. The discrete values (blue or orange points) are measured values while the solid line represents theoretically derived function $\left|J_0\left(\frac{4\pi}{\lambda}C_v u\right)\right|$, $\left|J_1\left(\frac{4\pi}{\lambda}C_v u\right)\right|$, respectively. One can see that the measured points in the both measurement modes (non-modulated and modulated) follow the predicted curves described by Bessel function of corresponding order. The proportional constant C_v was set to be an optimization parameter found by means of least square fitting. Obviously, the proportional constant obtained from $|U_{J0}|$ and $|U_{J1}|$ in the same point must be in agreement. For orange point the fitted procedure returns the proportional constant $C_v = 589$ in case of $|U_{J0}|$ whereas $C_v = 585$ for $|U_{J1}|$. In terms of amplitude, for maximal measured voltage 0.5V we obtain $d_{Z-non} = 294.5\,nm$ and $d_{Z-mod} = 292.5\,nm$. The results are in a very good agreement. One can note, that orange point measured at voltage 0.4V in case of non-modulated technique is very close to 2nd zero of the Bessel function, see Figure 3.12 (middle). Comparing to value b_2 in Figure 2.12 we can expect measured amplitude for this supply voltage to be around 234 nm. Using the proportional constant e.g. $C_v = 589$; amplitude of vibrations at 0.4V is $d_Z = 235.6\,nm$. The same procedure was done for blue point. There the proportional constants are $C_v = 141$, $C_v = 136$ for $|U_{J0}|$, $|U_{J1}|$, respectively, which corresponds to maximal amplitudes of vibrations $d_{Z-non}(u = 0.5) = 70.5\,nm$ and $d_{Z-mod}(0.5) = 68\,nm$. This analysis only proves the formula (3.25) and the reliability of the frequency modulated time average holography but says nothing about the sensitivity of different orders m for small amplitudes.

For that we plotted magnitude values along pixels denoted by the red line as outlined in the very top magnitude maps in the black frame of Figure 3.12. The cross-section is chosen to be in a nearness of a nodal line, where the amplitude is minimal and tends to evince linear behavior. In the left graph of the top row in Figure 3.12, magnitude values of non-modulated technique (m=0) are plotted as a red circles. The green solid line represents theoretically predicted values. The measured magnitudes are scattered around the theoretical curve, moreover, the small range of the graph testifies about low sensitivity of measurement in this range. The same results are plotted in the right hand side graph for frequency modulated measurement (m=1). The reconstructed magnitude values reliably follow the predicted curve. From the comparison of

the both plots follows, that the modulated technique brings much better sensitivity in case of very small amplitudes.

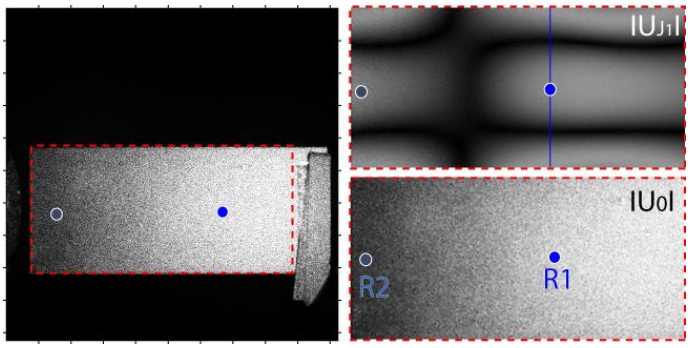

Figure 3.13: (left) The overall field of view in image plane with steady cantilever recorded by digital holography. Red dashed line delineates ROI; (right top) magnitude distribution within ROI of oscillating cantilever. Blue line denotes cross-section used for further analysis. Blue and violet points (pixels) are also important due to their detailed investigation; (right down) magnitude distribution of steady cantilever within ROI with the two important points R1 and R2.

In order to determine the smallest measurable amplitude by the frequency modulated holography (for our holographic arrangement); the following experiment was carried out. The supply voltage was successively increased started at 0 V with fine steps 0.05 mV up to 4 mV. Such low supply voltage generates extremely small amplitudes of vibration. The aim was to find the threshold of the supply voltage (or vibration amplitude) where noise represses measured signal and measurement can no longer be considered as valid. Again, two representative pixels (blue and violet points in Figure 3.13) were chosen for detailed analysis. The graphically interpreted results of blue point are plotted in Figure 3.14. The graph (A) represents coarse measurement executed in higher supply voltage range. The "coarse" measurement serves for calibration of independent (x) axis scale in order to obtain dependence on argument of Bessel function $\Omega = \frac{4\pi}{\lambda} d_z$ defined in (2.38) instead of supply voltage. This can be achieved with the use of properties of the first order Bessel function $J_{1-max}(\Omega = 1.84) = 0.58$. One should note, that for small amplitudes where $\Omega < 0.5$ the Bessel function can be approximated by linear function $J_1(\Omega) \approx \frac{1}{2}\Omega$, see red line in Figure 3.14. Finally, the graph (B) shows results of the "fine" measurement in the very small interval of supply voltages (small amplitudes). When approaching zero, the measured values (blue circles) do not significantly deviate from theoretical value up to $|U_{J1}|$~0.001. This was considered as the measurement threshold. Using the linear approximation:

$$d_z = 2\frac{\lambda}{4\pi}|U_{J1}|, \tag{3.27}$$

the smallest measureable amplitude reaches $d_z \sim 0.085\,nm$ or in terms of wavelength $d_z \sim \frac{\lambda}{6000}$.

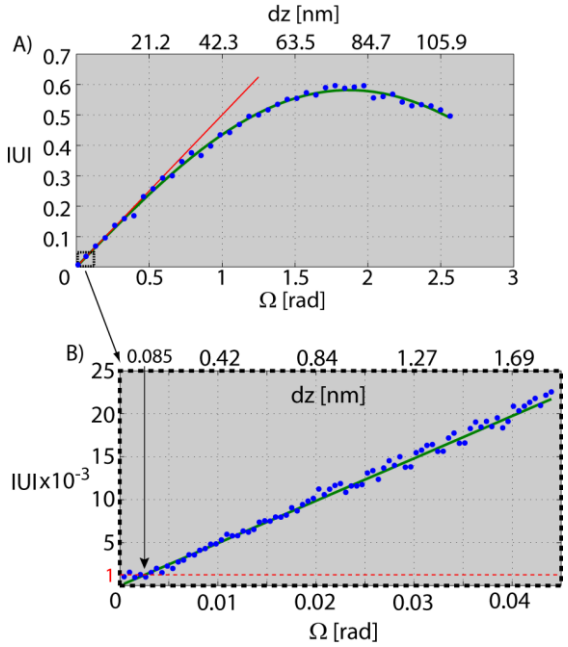

Figure 3.14: Values of magnitude at blue point with increasing supply voltage. The independent axis is calibrated to argument of the Bessel function. The red line marks out the noise level and the lowest measurable amplitude.

The level of noise presented in the reconstructed magnitude at this limiting value is around 20%, see Figure 3.15 – blue circles. The amount of noise was computed as a mean $\langle \frac{|U_{J1}|}{\langle |U_{J1}| \rangle} \rangle$ of ratio of the measured magnitudes $|U_{J1}|$ and theoretical data represented by average $\langle |U_{J1}| \rangle$ along the cross-section denoted by the blue line in Figure 3.13.

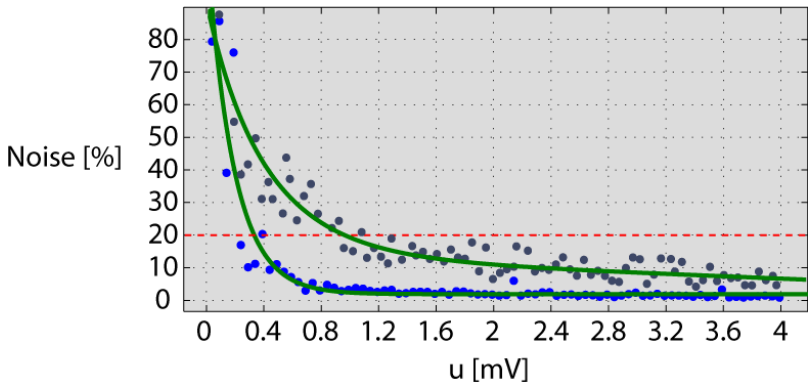

Figure 3.15: Presence of noise in magnitude values in blue and violet point as a function of supply voltage (or amplitude of vibrations).

The theoretical value was estimated from magnitudes at large amplitudes and scaled linearly with respect to supply voltage, see Figure 3.16. The theoretical value $\langle|U_{J1}|\rangle$ is denoted by red dashed line while the solid lines represent values of $|U_{J1}|$ at different supply voltages.

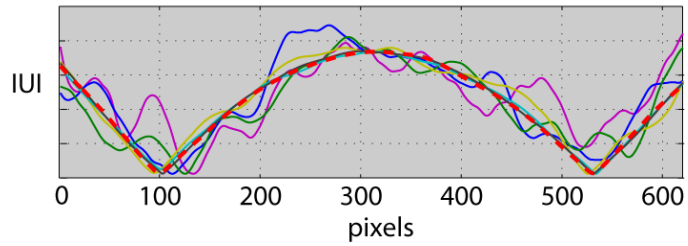

Figure 3.16: Values of magnitude along the "blue" cross-section in Figure 3.13. Dashed red line represents theoretical data, while solid lines represent values at different supply voltages (amplitudes of vibrations). For small amplitudes of vibrations the deviation from the theoretical curve rises (blue and purple curve) while larger amplitudes of vibrations result in better SNR (yellow). The limiting acceptable value of noise in data was set to be 20%.

All the values plotted in Figure 3.16 are normalized. As long as the supply voltage increases, the curves approach the theoretical value. This tendency can be approximated by decreasing exponential function (green line in Figure 3.15), which reflects the probability density distribution of speckle noise $p(I) = exp(-\frac{I}{\langle I\rangle})$, where I denotes intensity and $\langle I\rangle$ is its average. It illustrates the fact, that speckle noise plays a crucial role in our measurement as it holds true inherently for coherent measurement techniques like time average digital holography.

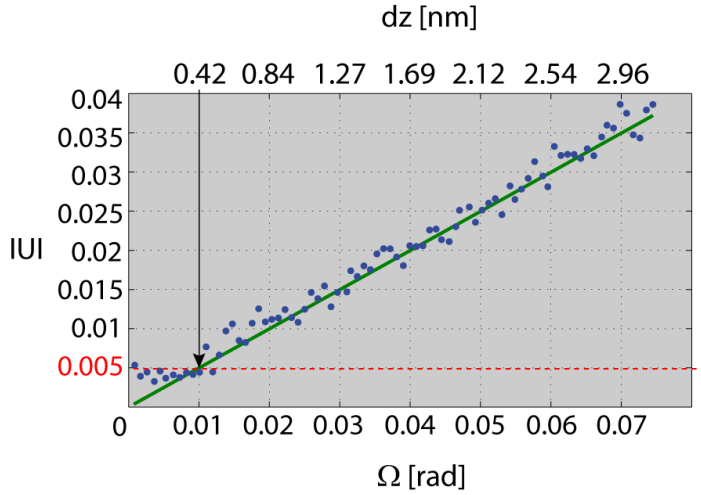

Figure 3.17: Values of magnitude at violet point with increasing supply voltage. The independent axis is calibrated to argument of the Bessel function. The red line marks out the noise level and the lowest measurable amplitude.

The same measurement procedure was repeated for pixel denoted by the violet circle. As it is shown in Figure 3.17, the smallest measureable amplitude is five times greater when compared with the blue point: d_z~0.42 nm. The worse SNR can also be noticed in Figure 3.15 (see the violet circles). At first sight it seems to be in contrary with the "blue point" measurement; however, the subsequent analysis will clarify the apparent discrepancy.

Starting with formula of the reconstructed magnitude field

$$\left|U_{J1}(R)\right| = |U_0(R)|\left|J_1\big(\Omega(R)\big)\right|, \tag{3.28}$$

where the magnitude distribution of non-oscillating object $|U_0(R)|$ is modulated by the first order Bessel function, see (2.44). Using (3.28) one can define a sensitivity S of the frequency modulated time average holography

$$S(R) = \frac{d\left|U_{J1}(R)\right|}{dd_Z} = \frac{d\left(|U_0(R)|\left|J_1\left(\frac{4\pi}{\lambda}d_Z(R)\right)\right|\right)}{dd_Z} \tag{3.29}$$

expressing the change of the measured value generated by the measured quantity - amplitude of vibrations. Substituting $J'_1(\Omega) = 1/2[J_0(\Omega) - J_2(\Omega)]$ [65] the formula (3.29) becomes

$$S(R) = \frac{2\pi}{\lambda}|U_0(R)|\left(\left|J_0\left(\frac{4\pi}{\lambda}d_Z(R)\right)\right| - \left|J_2\left(\frac{4\pi}{\lambda}d_Z(R)\right)\right|\right). \tag{3.30}$$

The sensitivity of the time average holography is defined by wavelength, the average exposure determining $|U_0(R)|$ and the amplitude of vibrations change itself coded in an argument of the zeroth and the second order Bessel functions. For extremely small amplitudes $J_0\big(\Omega(R)\big) \approx 1$ and $J_2\big(\Omega(R)\big) \approx 0$; the formula (3.30) simplifies to

$$S(R) = \frac{d\left|U_{J1}(R)\right|}{dd_Z} \approx \frac{2\pi}{\lambda}|U_0(R)|, \tag{3.31}$$

which is in agreement with linear approximation used in (3.27). The wavelength of laser is very stable and spatially independent. On the other hand the average exposure $|U_0(R)|$ varies with position R[1]. The discrepancy present between measurements at the blue and the violet point can be explained by the term $|U_0(R)|$. The normalized value of $|U_0|$ at the blue point $R1$ is $|U_0(R1)| = 1$, while $|U_0(R2)| = 0.25$ at the violet point $R2$. This results in ratio 5:1. Since

[1] The spatially dependence of $|U_0(R)|$ is in praxis caused by non-uniform illumination of the object, which, as a consequence of the analysis, should be avoided.

the measurement in $R1$ gives the best SNR in the whole reconstructed field, the limiting value $|U_{J1}(R1)|$~0.001 can be considered as a spatially independent constant of noise threshold $\Delta|U_{J1}|$ reachable in our experimental arrangements[1]. The minimal measurable amplitude in position R2: $d_{Z-MIN}(R2) = \frac{\lambda}{2\pi}\frac{\Delta|U_{J1}|}{|U_0(R2)|} = \frac{\lambda}{2\pi}\frac{\Delta|U_{J1}|}{0.25} = 5\frac{\lambda}{2\pi}\Delta|U_{J1}|$ is therefore expected to be five times larger than in R1 as verified experimentally.

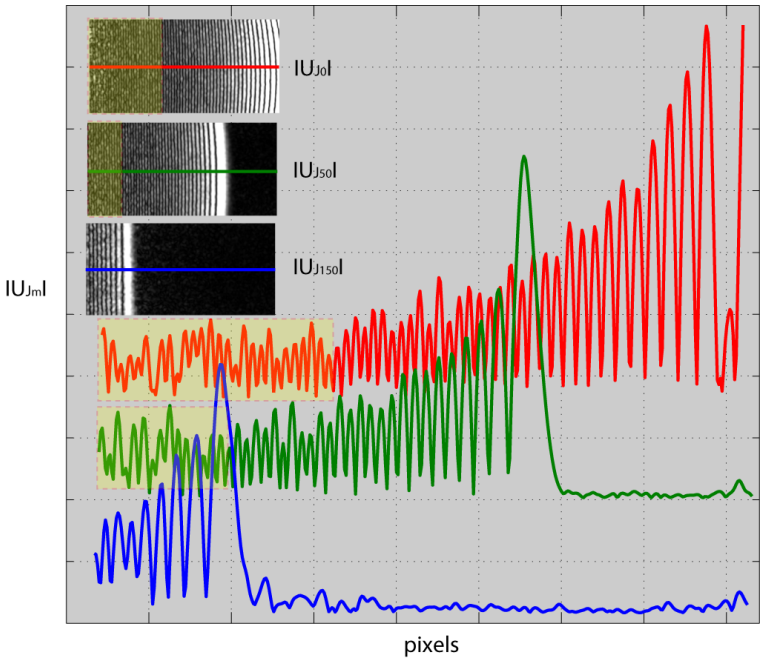

Figure 3.18: Frequency modulation used for large amplitudes of vibrations. Red line represents magnitude cross-section of non-modulated technique, while green and blue lines represent modulation of order m=50 respectively m=150.

In the case of large vibration amplitudes we take advantage of the fact that the locations of the zeros of the Bessel functions are spread apart for increasing order m. As a consequence, the number of fringes for the same amplitudes decreases with increasing m and therefore fringe patterns exceeding the sampling criterion can be effectively avoided. An example is introduced in Figure 3.18. The supply voltage of the cantilever was set to be 0.4 V, which at 100Hz generates vibrations amplitudes of the beam cantilever out of the measuring range of the non-modulated time average digital holography. This magnitude distribution inside the figure is denoted by $|U_{J0}|$ and the red cross-section is

[1] The exposure $|U_0(R)|$ depends on power of the laser, reflectivity and roughness of the object, dimensions of the object, geometrical arrangements etc. and therefore the noise threshold varies with these parameters. The noise threshold thus slightly varies for different objects under investigation.

plotted separately. The yellow rectangle covers the region, where the density of fringes is unresolvable due to speckles. Shifting the frequency of the reference wave about a fifty times multiple of the object oscillations frequency $f_r = f_0 + mf = 40MHz + 50 * 100Hz$ results in magnitude distribution $|U_{J50}|$. One can observe that the yellow rectangle has shifted closer to the edge of the cantilever as the measurement range has. One dimensional cross-section is denoted by the green curve in Figure 3.18. Although the measurement range has been extended using $|U_{J50}|$, still, the fringe pattern in very close region to the edge is not resolvable. Applying m=150 one can shift the measurement range even closer to the edge of the cantilever and by proper combination of zeroes extracted from magnitudes $|U_{J0}|, |U_{J50}|$ and $|U_{J150}|$ the amplitude distribution can be evaluated over the whole surface, see Figure 3.19.

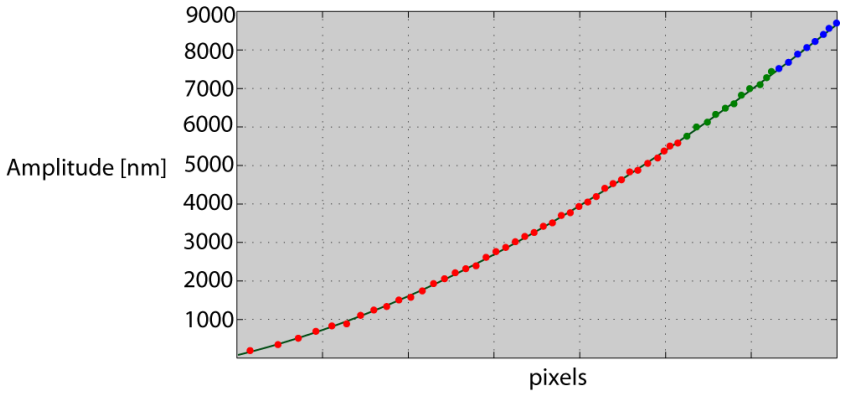

Figure 3.19: Amplitude of vibrations along the cantilever cross-section.

3.4 Evaluation of vibration amplitude independently in every pixel using phase modulation

So far we have only assumed a harmonic signal which drives the Bragg cells. The driving harmonic signal lead to frequency modulation, when the optical frequency of the 1st diffraction order is translated by the working frequency f_0[1]. However, phase-modulated CW signal

$$u(t) = sin(2\pi f_0 t - \phi(t)) \qquad (3.32)$$

can also be used, as it was already mentioned in chapter 3.1. From (3.6) follows, that phase modulation of the driven voltage is transformed in phase modulation of the 1st order wavefront

[1] Let us remind the working frequency $f_0 = 40\,MHz$ for the Bragg cells used within scope of this work.

$$U_{+1} = U_{in}exp(-j\phi)exp(j2\pi f_0)). \tag{3.33}$$

In this chapter, it will be shown how the phase modulation of the reference arm influences behavior of the time-average holography and how it can be exploited for quantitative analysis of vibrations amplitudes. Let us remind, that evaluation of amplitude distribution from intensity field obtained by time average holography is in most cases based on interpolation method, see chapter 2.4. This procedure has many inherent drawbacks and therefore a different approach to quantitative analysis of amplitude distributions is demanding. Considering the experimental setup outlined in Figure 3.3, the reference beam is phase modulated at frequency ω of the vibrating object with a modulation depth ϕ_{BC}.

$$U_r U_{BCr} = exp\big(j\phi_{BC}sin(\omega t)\big)exp(j2\pi f_0), \tag{3.34}$$

while the object wave is only modulated by oscillations of the object:

$$U_o U_{BCo} = exp(j\Omega\, sin[\omega t + \psi_0])\, exp(j2\pi f_0). \tag{3.35}$$

The object and the reference beams superpose forming a digital hologram (3.7). The real image of the diffracted field in the image plane

$$U_{real} \approx \int_0^T U_o U_{BCo} {U_r}^* {U_{BCr}}^*\, dt = \int_0^T exp\Big(j\big(\Omega\, sin[\omega t + \psi_0] - \phi_{BC}sin(\omega t)\big)\Big)\, dt = J_0\left(\sqrt{\Omega^2 - 2\Omega\phi_{BC}cos\,\psi_0 + {\phi_{BC}}^2}\right). \tag{3.36}$$

is computed by e.g. Fresenel transform. When oscillations of the object are synchronized with the reference beam phase modulation $\psi_0 = 0$, the formula (3.36) simplifies to:

$$|U_{real}| \approx |J_0(\Omega - \phi_{BC})|. \tag{3.37}$$

Now the loci of bright zero fringes are controllable by the user, since they appear where $\Omega = \phi_{BC}$. In order to verify the formula (3.37) a fine tuning of the modulation depth ϕ_{BC} was experimentally performed. The object under investigation was (similarly as it was in the previous experiments) the beam cantilever oscillating with frequency 1 kHz supplied with voltage 3.5 V. The reference wave was phase modulated according to formula (3.34). The modulation depth was successively increasing started at value $\phi_{BC} = 0\, rad$ with step of $\pi/31$ over the whole range up to 2π. Some magnitude distributions of the whole surface are introduced in black frame of Figure 3.20. For more detailed

analysis four representative pixels denoted by letters A,B,C,D in Figure 3.20 (right) were picked. In these points magnitude versus modulation depth with the fine steps was evaluated.

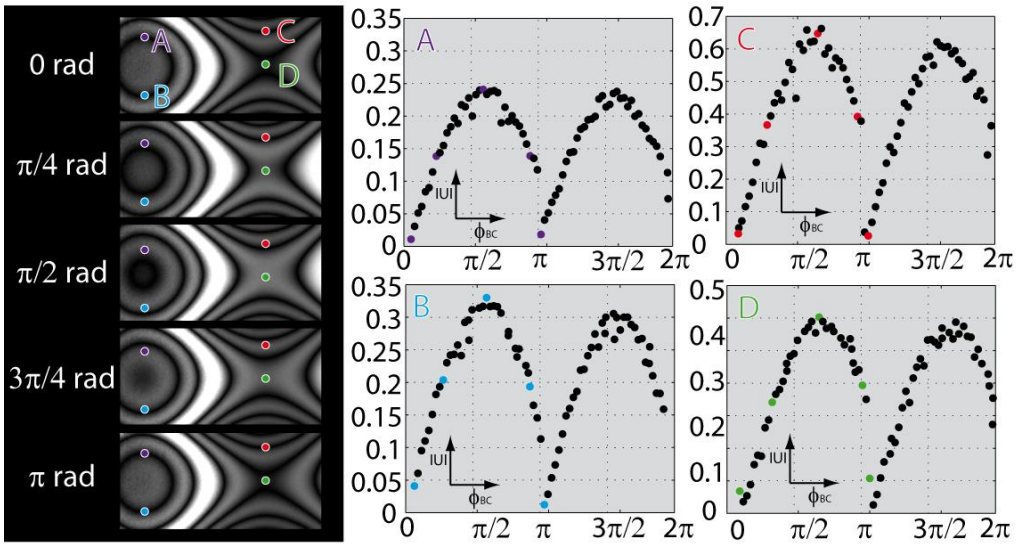

Figure 3.20: (black frame) Magnitude maps of an oscillating cantilever with different phase offsets; (right) Magnitude values at four points (A, B, C, D) are plotted as a function of the phase offset (colored point correspond to magnitude maps in black frame).

Although some noise is presented, the magnitude follows the formula $|J_0(\Omega - \phi_{BC})|$ within the half interval $\langle 0, \pi \rangle$ radians that creates period of the signal. These results can be consequently used for independent evaluation of vibrations amplitudes in every single pixel. In chapter 3.2 it was introduced, how to recover argument[1] of cosine function encoded in set of phase-shifted intensity field (3.13). Easy use of phase-shifting interferometry is derived from the harmonic cosine nature of interference fringes. In time average holography the intensity is modulated by Bessel functions. Unfortunately, the Bessel function of a sum cannot be expressed as a sum of terms, which holds true for the cosine: $cos(x - y) = cos(x)cos(y) + sin(x)sin(y)$. Therefore the straightforward phase recovery in the very same way as for cosine fringes is not possible. However, a possible solution is to exploit a nearly periodic nature of the Bessel functions and regard the modulation to be cosine. Replacing the real argument Ω with an approximate argument Ω^* the phase-shifting approach can be applied. We first have to capture and reconstruct set of time average digital holograms with different phase offsets ϕ_{BC}; similarly to formulas (3.16)-(3.19):

[1] In this case argument of cosine function physically represents phase between the reference and the object beam.

$$|U_i| = a + b|J_0(\Omega - \phi_{BCi})| \sim a + b|cos(\Omega^* - \phi_{BCi})|, \quad (3.38)$$

where additional term a is average value of the object field and multiplicative term b is the object field in the absence of oscillations. Assuming four-step algorithm, the optical phase shift about one fourth of the period, $\phi_{BCi} = \pi/4$, is introduced between each of the reconstructed amplitudes of object field:

$$|U_1| \sim a + b|cos(\Omega^*)|, \quad (3.39)$$

$$|U_2| \sim a + b|cos(\Omega^* + \pi/4)| = a + b|sin(\Omega^*)|, \quad (3.40)$$

$$|U_3| \sim a + b|cos(\Omega^* + \pi/2)| = a - b|cos(\Omega^*)|, \quad (3.41)$$

and

$$|U_4| \sim a + b|cos(\Omega^* + 3\pi/4)| = a - b|sin(\Omega^*)|. \quad (3.42)$$

These four equations in three unknowns a, b, Ω can be solved at each point of the reconstructed field. The additional term a is eliminated by subtracting the equations in pairs:

$$|U_1| - |U_3| = 2b|cos(\Omega^*)|, \quad (3.43)$$

$$|U_4| - |U_2| = 2b|sin(\Omega^*)|, \quad (3.44)$$

and the approximate argument Ω^* can be computed by formula:

$$\Omega^* = atan\left(\frac{|U_4| - |U_2|}{|U_1| - |U_3|}\right). \quad (3.45)$$

The four step algorithm is quite sensitive to deviations of the phase shift excursion from the expected or optimal value $\pi/4$. Some noise or outliers are also observable in results of measurement outlined in Figure 3.20. Therefore a more robust phase algorithm can be employed. For technique of phase-modulated time average digital holography 13-step algorithm has provided the best results in the used arrangements. The 13 step algorithm [69]:

$$\Omega^* = atan\left(\frac{-4A - 12B + 16C + 24|U_7|}{3D + 4A - 12E - 21F - 16G}\right), \quad (3.46)$$

where $A = |U_2| - |U_{12}|, B = |U_3| + |U_{11}| + |U_4| + |U_{10}|, C = |U_6| + |U_8|, D = |U_1| - |U_{13}|, E = |U_4| - |U_{10}|$, $F = |U_5| - |U_9|$, $G = |U_6| - |U_8|$, uses a frame increment of $\pi/8$.

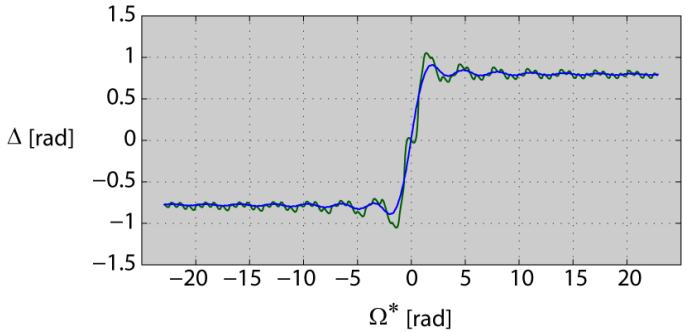

Figure 3.21: Correction function used for compensation of angle between $|cos\, x|$ and $|J_0(x)|$, Green line stands for 4-step algorithm, while blue line represents correction function for 13-step algorithm.

Since the arctangent function is bounded, the resulting phase (or argument of the Bessel function) Ω^* is wrapped within interval $\langle -\pi, \pi \rangle$[1]. Such a wrapped field must be unwrapped [25] in order to obtain phase distribution free of the 2π jumps. The approximate unwrapped phase Ω^* differs from the real argument of Bessel function Ω due to not perfectly periodic nature of Bessel function. The difference $\Delta = \Omega - \Omega^*$ is calculated as an angle between $|cos\, x|$ and $|J_0(x)|$, see equation (3.38). A graphically representation of Δ for 4 step algorithm (green) as well as for 13 step algorithm (blue) is plotted in Figure 3.21. Once the angle difference is known, the approximate phase is corrected in order to get real argument of the Bessel function $\Omega = \Omega^* + \Delta$.

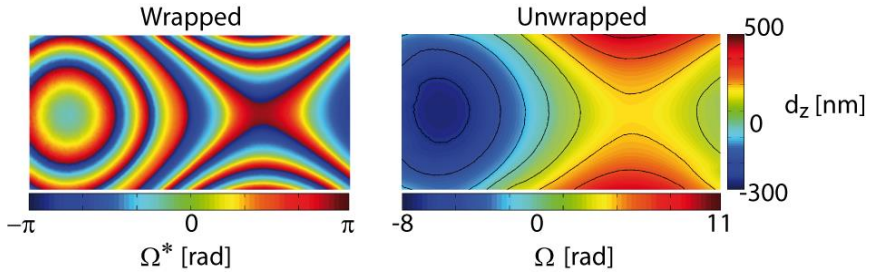

Figure 3.22: Wrapped phase with value within interval $\langle -\pi, \pi \rangle$ (left) and corrected unwrapped phase (right) without the phase jumps. Since phase is linearly proportional to amplitude of vibrations, vertical colorbar stands for values of amplitudes of vibrations.

The amplitude distribution can be computed with use of magnitude distributions with appropriate phase shifts from experiment shown in Figure 3.20. Then Figure

[1] The scale of arctangent function is $\langle -\pi/2, \pi/2 \rangle$ but it is good practice to consider the signs of the numerator and the denominator separately e.g. by ATAN2 function in MatLab.

3.22 presents wrapped phase Ω^* obtained by 13 step phase shifting algorithm and corrected unwrapped phase Ω. It is very important to note, that the phase shifting technique unlike other vibrations amplitude retrieval approaches is sensitive to sign of mechanical phase of vibrations. The measured phase Ω can be easily coded back into magnitude distribution by $|U_{Cal}| = |J_0(\Omega)|$ and compared to measured magnitude distribution $|U_{Meas}|$, see Figure 3.23. The both magnitude distributions are in a very good agreement.

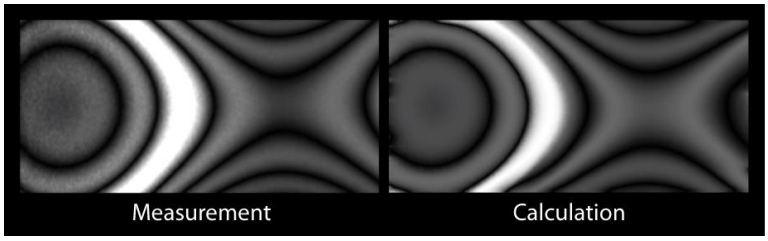

Figure 3.23: Measured (left) and calculated (right) magnitude distribution. The both maps are in a very good agreement as it is required.

Once the argument of Bessel function Ω is known, the amplitude distributions independently in every single pixel is calculated by $d_z = \frac{\lambda}{4\pi}\Omega$, that comes from (2.38) in case of normal incidence and reflection of illumination beam.

The most significant benefit of the phase modulated time average holography is its robustness and usability. A sequence of measurements at different times was carried out in order to asses a repeatability of the method. The total number of conducted measurement was 15. The first seven measurements were done in a short time, approximately 2 minutes gap in between two consecutive measurements. The time interval between the remaining measurements was prolonged to 10-15 minutes. The set of measured amplitude distributions was analyzed by means of basic statistical tools. The averaged amplitude distribution $\overline{d_z(R)} = \frac{1}{N}\sum_{n=1}^{N} d_{z\,n}(R)$ is shown in Figure 3.24. The averaged values of amplitudes as well as standard deviation $\sigma(R) = \sqrt{\frac{1}{N}\sum_{n=1}^{N}\left(d_{z\,n}(R) - \overline{d_z(R)}\right)^2}$ along the cross-section denoted by green line in Figure 3.24 are introduced in Figure 3.25 (A). The standard deviation defines "type A" uncertainty representing primarily random noise presented in the measurement procedure. Noise usually consists of an additional and multiplicative part. In the same manner one can define

the standard deviation as $\sigma(R) = \mathrm{A} + \mathrm{B}\,\overline{d_z(R)}$[1]. After fitting the measured data, standard deviation is determined as:

$$\sigma(R) = 0.05 + 0.01\,\overline{d_z(R)}\ [nm], \qquad (3.47)$$

or in terms of percentage of the measured amplitude $\frac{100\sigma}{\overline{d_z}} = \frac{5}{\overline{d_z}} + 1\ [\%]$. Considering value $\overline{d_z} = 300\,nm$, the standard deviations becomes $\sigma = 3.05\,nm \sim 1.17\,\%$.

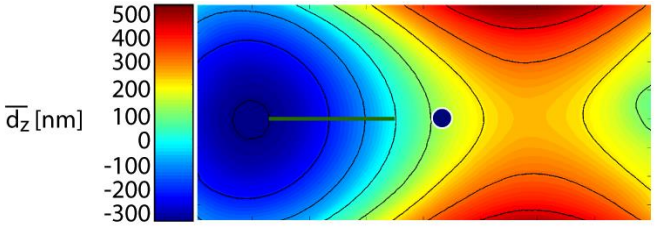

Figure 3.24: Amplitude distribution averaged from 15 measurements. Green cross-section and blue point are used for further analysis.

The values of measured amplitudes are spread around mean value according to laws of normal distribution as can be seen from histogram plot Figure 3.25 (B).

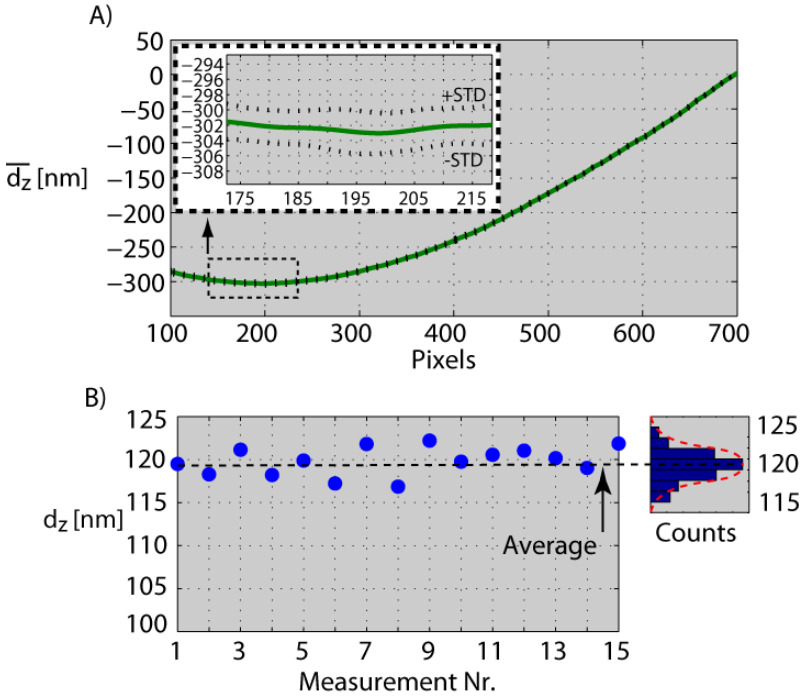

Figure 3.25: (A) Averaged values of vibrations amplitudes along the green cross-section (green curve) and interval determined by standard deviation (black dotted curves); (B) fifteen measurements of vibrations amplitudes at the blue point that are spread around the average according to laws of normal distribution as can be observed in the histogram plot.

[1] The standard deviation σ depends furthermore on values of magnitude fields. Therefore (3.47) is also influenced by Bessel function, however, this influence was omitted in order to stay clear

The histogram was created from values measured at pixel denoted by blue circle. The normal distribution is described by Gaussian function of which properties can be used for deeper insight to error analysis. Standard deviation σ accounts for 68.27 percent of the Gaussian function; while two standard deviations from the mean account for 95.45 percent and three standard deviations account for 99.73 percent. In other words, results of almost all measurements fall into interval of 3σ, what means $3\sigma = 9.2\,nm \sim 3.5\%$ for the measurement around $\overline{d_z} = 300\,nm$. One should note, that this kind of analysis does not include evaluations of all contributions to the dispersion of values that might reasonably be attributed to the measurand.

3.5 Discussions and conclusions

Three techniques improving time average digital holography have been developed and they were introduced in chapter three. Namely it is:

- Heterodyne detection realized via appropriate frequency modulation in relation with frame rate of the digital sensor. It was shown, that using phase-shifting technique one can improve lateral resolution up to spatial frequency bandwidth of the digital sensor. Moreover the amount of useful signal (playing crucial role in sensitivity of the method) is increased about more than 30%.
- Frequency modulation, when the frequency of the Bragg cell in reference arm is shifted about an integer multiple of frequency at which the object oscillates. This technique results in extension of dynamic range for very small as well as for very large amplitudes. The lower bound of the measureable range is around $\lambda/6000$, the higher bound can be estimated to be 20λ, that creates a dynamic range of the method to be 120000[1].
- Phase modulation can add a well-defined bias to argument of the Bessel function. This can be used for direct application of phase-shifting technique resulting in rapid, accurate, robust and user-friendly evaluation of amplitude distribution.

Although all the methods were introduced separately for clarity reasons, they share identical hardware requirements and can be arbitrarily combined, keeping in mind the experimental arrangements outlined in Figure 3.3. The Bragg cell

[1] For larger amplitudes of vibrations than 20λ the recovery of amplitude distribution is becoming more difficult due to lack of fringes at region with small amplitudes, however, the higher bound can be further shifted

placed in the reference arm is driven by voltage generated by an arbitrary waveform generator: $u_{BCR}(t) = sin(2\pi f_{R-mod}t - \phi(t))$ while $u_{BCO}(t) = sin(2\pi f_{O-mod}t)$ holds for driving signal supplying the Bragg cell employed in the object arm. The driving signal is transformed via the Bragg cell into the 1st order wavefront described by:

$$U_{BCr} = exp(-j\phi)exp(j2\pi f_{R-mod})) \tag{3.48}$$

in case of reference wave and

$$U_{BCo} = exp(j2\pi f_{R-mod})) \tag{3.49}$$

for the object wave. The reference beam is phase modulated at frequency ω of the vibrating object with a modulation depth ϕ_{BC}: $\phi = \phi_{BC}\sin(\omega t)$ while the frequency is shifted about integer m of frequency of the object f and one fourth of digital camera frame rate FPS in order to employ heterodyne technique with $\pi/2$ phase shifts between holograms[1]: $f_{R-mod} = f_0 + mf + FPS/4$. The wavefront exiting the Bragg cell in the object arm U_{BCo} is additionally phase modulated by oscillations of the object $exp(j\Omega(R)\, sin[\omega t + \psi_0(R)])$ resulting in

$$U_o U_{BCo} = U_0 exp(j\Omega(R)\, sin[\omega t + \psi_0(R)])exp(j2\pi f_{R-mod})). \tag{3.50}$$

The object and the reference beam superposing on the digital sensor are forming a digital hologram (3.7). The hologram is time integrated over exposure time T. Due to heterodyne acquisition, the series of phase shifted holograms can be processed by means of phase shifting approach and complex field U_o replaces the hologram field h in reconstruction process, see (3.22). The real image of diffracted field in image plane

$$U_{real} \approx U_0 \sum_{n=-\infty}^{\infty} J_n(\Omega - \phi_{BC}) \int_{-T/2}^{T/2} exp(jn[\omega t + \psi_0]) \times \\ \times exp(-jm\omega t)\, dt. \tag{3.51}$$

is computed by e.g. Fresnel transform. When the integration time is much longer in comparison with the period of the vibrations, the time averaging process lead to

$$|U_{real}| \approx |U_0||J_n(\Omega - \phi_{BC})|. \tag{3.52}$$

[1] In general, one can use FPS/M, where M is an integer in order to generate phase shifts appropriate for the used phase-shifting algorithm.

The formula (3.52) includes all advantages described separately in previous subsections.

A combination of these three approaches was used for measurement of cantilever vibrating at $1000\,Hz$. The supplying voltage of the cantilever started at $200\,\mu V$ and finished at $200\,mV$.

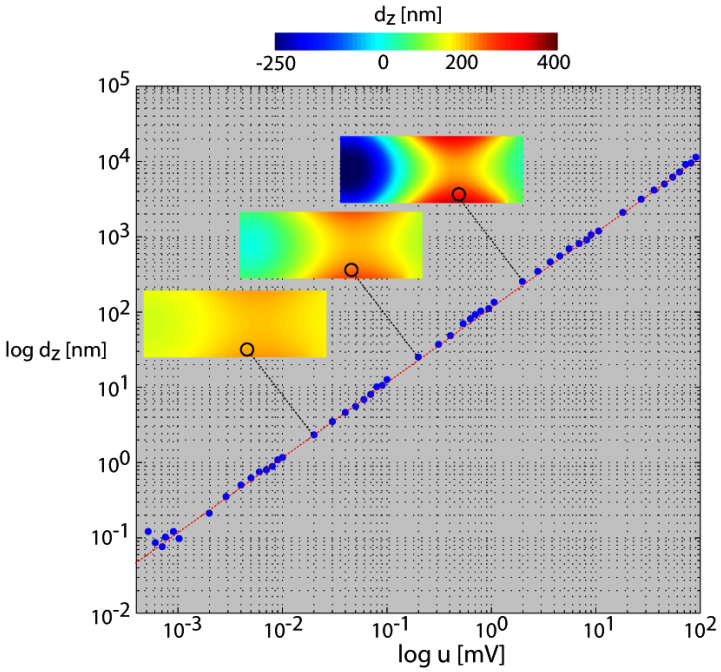

Figure 3.26: Measured amplitudes of vibrations of the beam cantilever at different supply voltages. Blue points determine value of amplitude of vibrations in the marked position. Some amplitude maps of the whole surface are also introduced and linked to corresponding measurement.

Logarithmic increment steps of supplying voltage were chosen instead of linear due to a huge amount of measurements. The Bragg cells in reference and object arm were set in agreement with formulas (3.48), (3.49), respectively. For small amplitudes the frequency of supplying signal of reference arm Bragg cell was shifted about frequency of the cantilever in order to get the maximal sensitivity. In total, thirteen measurements $i = 0,1,2 \dots 12$ with different phase offsets $\phi_{BC} = i\pi/8$ were taken for each voltage of the cantilever. Formula (3.46) and related corrections were applied for recovery of vibration amplitude distributions d_z. Results of the measurement are introduced in Figure 3.26. Some whole-field distributions are shown in the inner figures while the logarithmic plot represents values measured in one pixel denoted by the black circle. Measured values (blue points) follow the theoretical values (red dashed line) down to approximately

$0.1\,nm$. This noise level has already been derived in chapter 3.3. As obvious from scale of the plot in Figure 3.26, the dynamic range of the measurement is 100000.
It is worthwhile to mention some sources of distortions degrading the magnitude distribution. A typical intensity distribution at one instant of time is of the form:

$$\left|U_{Jn}\right| = |U_0|\left(1 + V\left|J_n\left(\frac{4\pi}{\lambda}d_z - \phi_{BC}\right)\right|\right) n_S n_{E*} + n_{E+} + n_D, \qquad (3.53)$$

where $|U_0|$ denotes the low frequency background intensity caused by a varying illumination, e.g. a Gaussian profile of the expanded laser beam, or a changing object reflectivity. The parameter V is the fringe visibility influenced mainly by the ratio between the reference and object wave amplitudes. Parameter n_S describes the magnitude variation caused by the speckles, which act as signal dependent coherent noise. The electronic noise n_{E+}, n_{E*} originates in photodetectors or waveform generators supplying the Bragg cells. In practical applications of holographic interferometry electronic noise plays a minor role as compared to the speckle noise. So normally no special care is taken regarding electronic noise. Finally n_D describes diffraction patterns of particles in the optical paths. Special sources of distortions are environmental distortions like vibrations and air turbulence. Therefore care has to be taken to isolate the holographic arrangement from vibration. This is normally done with help of vibration isolated tables. Equipment which undergoes any mechanical motion should be removed from the vibration isolated table. Air turbulence may change the refractive index distribution of air. Any distortions in either arm of the holographic interferometer between measurements influence the phase drift Ω_D.
All the aforementioned mentioned distortions affect the additive A and multiplicative B noise components simplifying (3.53) to:

$$\left|U_{Jn}\right| = A + B\left|J_n\left(\frac{4\pi}{\lambda}d_z - \phi_{BC}\right)\right|. \qquad (3.54)$$

The optimization of visibility $V = 2|U_r||U_o|/(|U_r|^2 + |U_o|^2)$ hidden in multiplicative noise $B = |U_0|Vn_S n_{E*}$ is not as trivial as in case of non-modulated holography [32]. However, when $\left|J_n\left(\frac{4\pi}{\lambda}d_z - \phi_{BC}\right)\right| \ll 1$, the optimal value of parameter $V = 1$ holds for $|U_r| = |U_o|$. The additional component A is eliminated due to phase-shifting, see (3.43), (3.44). The most significant source of noise is deterministic speckle noise described by phase Ω_S. The speckles are characterized by high-spatial frequency and due to their deterministic nature they cannot be easily removed. The direct approach to a complex field within digital holography, however, enables to lower

the speckle noise. For that one needs to use two digitally reconstructed time-averaged holograms: one of the vibrating object $\sim U_{Jn}$ and the other one of the object without vibrations $\sim U_0$. The reconstructed complex field $U = Re\{U\} + jIm\{U\}$ by formulas (2.19), (2.22), (2.25) consists of orthogonal components (real and imaginary part). Let us consider complex field of the object without oscillations U_0 and of the object undergoing harmonically oscillations U_{Jn}:

$$U_0 = B_0 exp[j(\Omega_S + \Omega_{D0})], \tag{3.55}$$

$$U_{Jn} = B_1 J_n\left(\frac{4\pi}{\lambda} d_z - \phi_{BC}\right) exp[j(\Omega_S + \Omega_{D1})], \tag{3.56}$$

respectively. Normalization of (3.56) with respect to (3.55) is calculated as a product of complex field U_{Jn} and conjugate of U_0 divided by envelope $|U_0|$:

$$\langle \frac{U_{Jn} U_0^*}{|U_0|^2} \rangle = \frac{B_1}{B_0} J_n\left(\frac{4\pi}{\lambda} d_z - \phi_{BC}\right) exp[j(\Omega_{D1} - \Omega_{D0})]. \tag{3.57}$$

It is important to notice, that in (3.57) the high spatially varying speckle noise Ω_S is replaced by low frequency phase drift $\Delta\Omega_D = \Omega_{D1} - \Omega_{D0}$ between measurements of U_0 and U_{Jn}. Therefore a time gap between the measurements is required to be minimized.

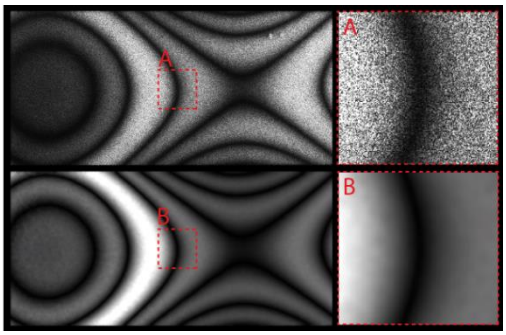

Figure 3.27: Non filtered magnitude distribution (top) and its filtered version (down). Detailed subsections of the both versions is shown in the right column.

Moreover, the smooth orthogonal components of $U_{Jn}U_0^*/|U_0|^2$ can be easily low-pass filtered without the loss of fringe contrast, see Figure 3.27. The filtering process removing the high-frequency speckle noise is denoted by $\langle\ \rangle$. It is also worth noticing, that phase field

$$atan\left(\frac{Im\{U\}}{Re\{U\}}\right) = \Delta\Omega_D + \frac{\pi}{2} sgn\left(J_n\left(\frac{4\pi}{\lambda} d_z - \phi_{BC}\right) + 1\right) \tag{3.58}$$

can be used for identification of zeroes[1] of the Bessel function instead of searching of minima in the intensity field as mentioned in Figure 2.12. An example of such a phase field is introduced in Figure 3.28.

After filtering of speckle noise, which is generating high frequency disturbing signal, the formula (3.54) becomes

$$|U_{Jn}| = \tilde{B}\left|J_n\left(\frac{4\pi}{\lambda}d_z - \phi_{BC}\right)\right|, \tag{3.59}$$

where $\tilde{B} = B_1/B_0$ denotes distortions caused by drift of environmental conditions between measurement of U_{Jn} and U_0 (ideally if $B_1 = B_0$). The magnitude $|U_{Jn}| \sim |U_{Jn}U_0^*/|U_0|^2|$ has been used for all measurement within this scope if not stated elsewhere.

Figure 3.28: (left) Magnitude map; (middle) phase map with almost no phase drift. Phase jumps correspond to zeroes in the magnitude map; (right) phase map including a phase drift.

From (3.59) follows, that three parameters $\tilde{B}$, λ, ϕ_{BC} influence the resulting magnitude distribution. Although the error sources can be mutually compensated, for the maximal error estimation we can apply total differential in a form

$$d|U_{Jn}| = \sqrt{\left(\frac{\partial|U_{Jn}|}{\partial\tilde{B}}d\tilde{B}\right)^2 + \left(\frac{\partial|U_{Jn}|}{\partial\lambda}d\lambda\right)^2}, \tag{3.60}$$

where

$$\frac{\partial|U_{Jn}|}{\partial\tilde{B}} = \left|J_n\left(\frac{4\pi}{\lambda}d_z - \phi_{BC}\right)\right|, \tag{3.61}$$

$$\frac{\partial|U_{Jn}|}{\partial\lambda} = \frac{\tilde{B}}{2}\left|\left|J_{n-1}\left(\frac{4\pi}{\lambda}d_z - \phi_{BC}\right)\right| - \left|J_{n+1}\left(\frac{4\pi}{\lambda}d_z - \phi_{BC}\right)\right|\right|\frac{4\pi}{\lambda^2}d_z. \tag{3.62}$$

Due to the great coherence and the stability of laser source, the ratio $\Delta\lambda/\lambda^2$ makes the contribution of (3.62) to the total error (3.60) about at least five orders lower than contribution coming from (3.61) and therefore can be neglected.

In case of an amplitude distribution calculated by the direct inversion of a magnitude distribution e.g. in [39], [50], [66], no phase shift $\phi_{BC} = 0$ need not to

[1] Change of Bessel function sign (zero) is found as a jump in (3.58) via sgn (signum) function

be introduced and formula (3.60) describes the final error contribution. The error acting in amplitude distribution is directly proportional to error $d\tilde{B}$. The situation is becoming little bit more complicated in phase modulated holography, since there is in addition an error contribution coming from deviations of phase offsets. The phase offset error lies in an interval ε shifting the ideal phase offset $\hat{\phi}_{BC}$ to be:

$$\phi_{BC} = \hat{\phi}_{BC} + \varepsilon. \tag{3.63}$$

An evident error of ϕ_{BC} arrives when the phase of the reference and the object wave are not perfectly synchronized $\psi_0 \neq 0$, see (3.37). Moreover, the source of multiplicative distortions denoted by $d\tilde{B}$ behaves differently from the direct inversion approach. Although the 13-step phase shifting algorithm has been used within the scope of this dissertation by reason of robustness, for simplification the four step algorithm (3.39)-(3.42) is considered in following analysis. A set of magnitude distributions is necessary for employing the phase shifting approach. The time gap between measurements results in a variation of the multiplicative parameter $\tilde{B}$, which can be described by its mean value $\tilde{B}_{AVE}$ and an interval defined by standard deviation $\sigma(\tilde{B})$:

$$\tilde{B} = \tilde{B}_{AVE} + \sigma(\tilde{B}). \tag{3.64}$$

Four phase shifted magnitude distributions including the error sources ε, $\tilde{B}$ yield to:

$$|U_1| = \left(\tilde{B}_{AVE} + \sigma(\tilde{B})\right)|cos(\Omega^*)|, \tag{3.65}$$

$$|U_2| = \left(\tilde{B}_{AVE} - \sigma(\tilde{B})\right)\left|cos\left(\Omega^* + \frac{\pi}{4} + \varepsilon\right)\right|, \tag{3.66}$$

$$|U_3| = \left(\tilde{B}_{AVE} + \sigma(\tilde{B})\right)\left|cos\left(\Omega^* + \frac{\pi}{2} + \varepsilon\right)\right|, \tag{3.67}$$

and

$$|U_4| = \left(\tilde{B}_{AVE} - \sigma(\tilde{B})\right)cos\left(\Omega^* + \frac{3\pi}{4} + \varepsilon\right). \tag{3.68}$$

These four equations in three unknowns can be solved at each point of the reconstructed field. After some mathematical operations[1], formulas (3.65)-(3.68) simplify to:

$$|U_1| \approx \left(\tilde{B}_{AVE} + \sigma(\tilde{B})\right)|cos(\Omega^*)|, \tag{3.69}$$

$$|U_2| \approx -\left(\tilde{B}_{AVE} + \sigma(\tilde{B})\right)|sin(\Omega^*)\, cos\,\varepsilon|, \tag{3.70}$$

$$|U_3| \approx -\left(\tilde{B}_{AVE} + \sigma(\tilde{B})\right)|cos(\Omega^*)cos\,\varepsilon|, \tag{3.71}$$

and

$$|U_4| \approx \left(\tilde{B}_{AVE} + \sigma(\tilde{B})\right) sin(\Omega^*)\, cos\,\varepsilon. \tag{3.72}$$

The aim of the analysis is to treat the worst error, even though in some measurements the values can be mutually compensated. Therefore a numerator of the fraction describing the error parameter was intended to be maximal unlike the value of denominator. Using of the approximation for small angles $cos\,\varepsilon = 1 - \varepsilon^2/2$ and subtraction in pairs $|U_1| - |U_3|$, $|U_4| - |U_2|$ leads to phase recovery formula

$$\Omega^* = atan\left(\frac{2\tilde{B}_{AVE} + 2\left|\sigma(\tilde{B})\right|}{2\tilde{B}_{AVE} - 2\left|\sigma(\tilde{B})\right|}\frac{\varepsilon^2}{4-\varepsilon^2}\frac{|U_4| - |U_2|}{|U_1| - |U_3|}\right). \tag{3.73}$$

The ratio $c_v = \frac{|\sigma(\tilde{B})|}{\tilde{B}_{AVE}}$ represents a coefficient of variation, which, together with considering $\sigma(\tilde{B}) \ll \tilde{B}_{AVE}$, makes the formula (3.73) to be:

$$\Omega^* = atan\left((1 + 2c_v)\left(1 + \left(\frac{\varepsilon}{2}\right)^2\right)\frac{|U_4| - |U_2|}{|U_1| - |U_3|}\right). \tag{3.74}$$

Individual disturbances contributing to overall error in the phase map $\Delta\Omega^*$ can be expressed by

$$d\Omega^* = \sqrt{\left(\frac{\partial\Omega^*}{\partial c_v}dc_v\right)^2 + \left(\frac{\partial\Omega^*}{\partial\varepsilon}d\varepsilon\right)^2}. \tag{3.75}$$

Substituting (3.74) into (3.75) gives the formula[2]

---

[1] Formula $cos(x+y) = cos(x)\,cos(y) - sin(x)\,sin(y) \approx cos(x)\,cos(y)$ for very small value of y was applied.

[2] Used relations:

$(1 + 2c_v)(1 + \varepsilon^2/4) \approx 1 + 2c_v + \varepsilon^2/4$

$2c_v tan\dot{\Omega}^* + (\varepsilon^2/4)tan\dot{\Omega}^* + tan\dot{\Omega}^* \approx tan\dot{\Omega}^*$

$(|U_4| - |U_2|)/(|U_1| - |U_3|) = tan\dot{\Omega}^*$

$$d\Omega^* = \sqrt{\left(sin2\dot{\Omega}^* dc_v\right)^2 + \left(sin2\dot{\Omega}^* \frac{\varepsilon}{4} d\varepsilon\right)^2}, \tag{3.76}$$

where $\dot{\Omega}^*$ denotes phase distribution without presence of disturbances. Similarly, formula

$$dd_z = \frac{dd_z}{d\Omega^*} d\Omega^* = \\ = \frac{\lambda}{4\pi} \sqrt{\left[\left(sin2\dot{\Omega}^* dc_v\right)^2 + \left(sin2\dot{\Omega}^* \frac{\varepsilon}{4} d\varepsilon\right)^2 + \left(\frac{\partial \Delta(\Omega^*)}{\partial \Omega^*} d\Omega^*\right)^2\right]} \tag{3.77}$$

provides better picture of how the individual disturbances contribute to overall error in amplitude distribution $d_z = \frac{\lambda}{4\pi}[\Omega^* + \Delta(\Omega^*)]$, where $\Delta(\Omega^*)$ is the correction function introduced in 3.4.

Formula (3.77) holds true generally unless the applied approximations are valid. However, it is necessary to know real values of error parameters dc_v, $d\varepsilon$ emerging in the experimental arrangements, which can be substituted in relation (3.77). A convenient way to estimate the phase offset error of the experimental arrangements is to use the solution for phase offset ϕ_{BC} from a series of five Bessel fringe patterns. The patterns are recorded with equally distributed $\frac{\pi}{2}$ steps and the phase offset is then calculated by formula:

$$\phi_{BC} = acos\left(\frac{1}{2}\frac{|U_5| - |U_1|}{|U_4| - |U_2|}\right). \tag{3.78}$$

As a matter of fact formula (3.78) is a solution of a set of five equations (3.38) for ϕ_{BC}. The solution yields the phase shift at each measurement point R. The results can be visualized by a histogram plot, where the height of the bars represents counts of pixels shifted about value $\phi_{BC}(R)$.

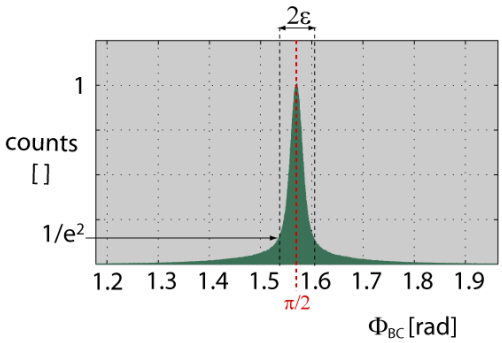

Figure 3.29: Normalized histogram of phase steps calculated for the whole surface of the cantilever.

In faultless world, the histogram would be a single bar at $\frac{\pi}{2}$ having height corresponding to total number of pixels of the field. The width, on the other hand, reflects the error of the phase offsets. The histogram of measurement performed by the experimental arrangements is shown in Figure 3.29. At first sight, the histogram envelope is pretty narrow standing for high quality phase shifting realization. HW (half width) at[1] $1/e^2$ was chosen as a measure of the error, that is more stringent in comparison to HWHM (half width at half maximum). The measured value is $\varepsilon = 0.0035\, rad$.

In order to estimate the error $d\tilde{B}$, two complex fields of non-oscillating object were subsequently captured with a 20 seconds time gap between measurement. The aim of the measurement was to follow formulas (3.55) and (3.56) where the error $d\tilde{B}$ originates. As mentioned, the both fields were captured in state of non-oscillating object[2] and therefore (3.55) and (3.56) become:

$$U_1 = B_0 exp[j(\Omega_S + \Omega_{D0})], \tag{3.79}$$

$$U_2 = B_1 exp[j(\Omega_S + \Omega_{D1})]. \tag{3.80}$$

Mean filter of a product of complex field U_2 and conjugate of U_1 divided by envelope $|U_1|$:

$$\langle \frac{U_2 U_1^*}{|U_1|^2} \rangle = \frac{B_1}{B_0} exp[j(\Omega_{D1} - \Omega_{D0})]. \tag{3.81}$$

yields to normalized complex field analogously to (3.57). Magnitude

$$|U_{12}| = \tilde{B} \tag{3.82}$$

affords direct access to $\tilde{B} = B_1/B_0$, since neither of complex fields U_1, U_2 is modulated by the Bessel function due to steady state of the object. Magnitude distribution $|U_{12}|$ is introduced in the inner image of Figure 3.30. It is obviously seen, that magnitude values over the object surface are uniformly distributed about 1 as expected. For error analysis statistical parameters defined in (3.64) are required and therefore the measurement was repeatedly performed. Results of the experiment are illustrated in Figure 3.30. The measured values at the pixel denoted by the blue circle are plotted as a function of measurement number (meaning acquisition at different times). The measured values of $\tilde{B}$ are scattered

[1] e = 2.718 – Euler number

[2] For non-oscillating object holds $d_z = 0$ and therefore $J_0(0) = 1$.

around mean value $\tilde{B}_{AVE} = 0.977$ expressed in number by standard deviation $\sigma(\tilde{B}) = 0.018$. The coefficient of variation $c_v = \frac{|\sigma(\tilde{B})|}{\tilde{B}_{AVE}} = 0.018$ is used in (3.74) and acts as a parameter in (3.77).

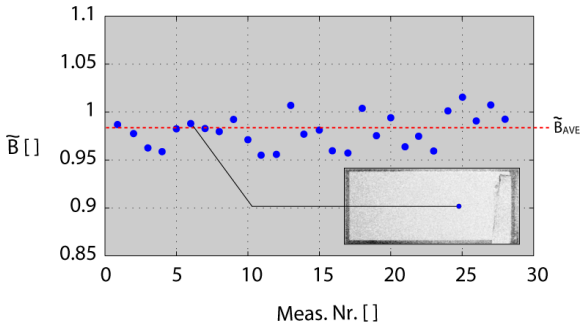

Figure 3.30: Results of repetitive measurement of multiplicative parameter $\tilde{B}$ in the position marked by the blue point in the inner figure.

Once the values of the error contributions c_v, ε are known, one can substitute them into relations (3.76) and (3.77). Error in recovered phase $d\Omega^*$ is plotted as a function of phase Ω^* itself in Figure 3.31. The blue line follows values calculated by formula $\sin 2\dot{\Omega}^* \frac{\varepsilon}{4} d\varepsilon$, while formula $\sin 2\dot{\Omega}^* dc_v$ is represented by the green line.

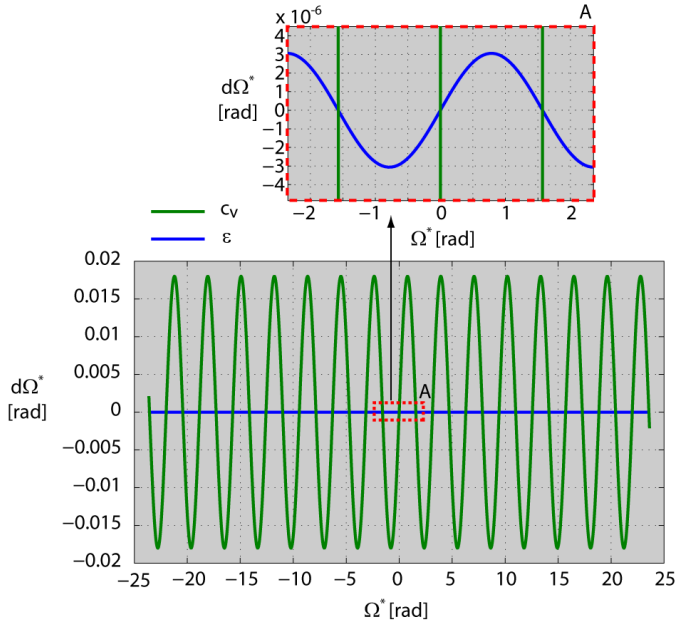

Figure 3.31: Contributions to overall measurement error coming from parameters $\mathbf{c_v}$, $\boldsymbol{\varepsilon}$, respectively.

The contribution coming from the phase offset error ε is negligible when compared to the error caused by a variation of the multiplicative factor $\tilde{B}$. Before the recovered phase Ω^* can be recalculated in order to obtain amplitude distribution, one has to correct the phase due to difference between cosine and

Bessel function, see chapter 3.4. This fact must also be considered in the error analysis since wrong value of Ω^* will produce an incorrect link to correction value within the correction look-up table. This error contribution is in equation (3.77) described by the term $(\partial\Delta(\Omega^*)/\partial\Omega^*)d\Omega^*$. The derivative $\partial\Delta(\Omega^*)/\partial\Omega^*$ is calculated as a slope of function introduced in Figure 3.21. The total error occurring in amplitude distribution as function of amplitude values is plotted in Figure 3.32.

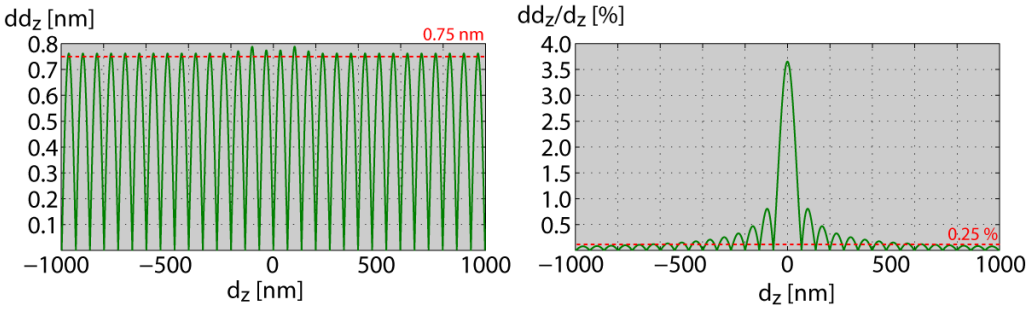

Figure 3.32: Error of measurement employing phase shifting technique as a function of measured amplitude of vibrations. Relative error is introduced in the right-hand plot.

The most significant contribution from error rate point of view is the multiplicative noise described by c_v. The error originating by incorrect phase offset[1] is negligible and error coming from the correction procedure generates error at least four times smaller.

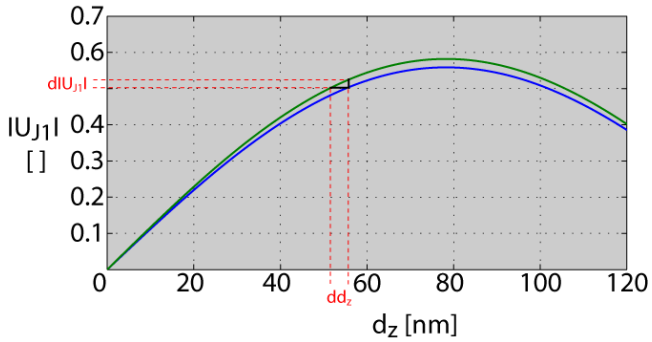

Figure 3.33: Error dd_z in amplitude of vibrations measurement generated by deviation in multiplicative parameter $\tilde{B}$. Green line represents theoretical value, while blue line stands for values burdened with the error.

The peak to valley error is about 0.75 nm while RMS (Root Mean Square) error is 0.53 nm. These value were computed for frequency modulated technique when $m=1$ in (3.59); however, due to minor contribution of $\partial\Delta(\Omega^*)/\partial\Omega^*$ to total error, the same error (except some local deviations in order of 0.05nm) influences measurement for $m\neq1$.

[1] This holds true for four step phase shifting algorithm. 13-step algorithm evinces results even about two order better comparing to 4-step algorithm.

When analyzing error behavior of the phase modulated time average digital holography, it is also worthwhile to mention error connected with the direct inversion of the magnitude field. The only error source in (3.60) is multiplicative parameter $\tilde{B} = \tilde{B}_{AVE} + \sigma(\tilde{B})$ quantitatively described by (3.61). The experiment, of which results are introduced in Figure 3.30, determined the parameter $\tilde{B} = \tilde{B}_{AVE} - \sigma(\tilde{B}) = 0.96$ in the worst case. Theoretical curve $\left|J_1\left(\frac{4\pi}{\lambda}d_z\right)\right|$ is plotted in Figure 3.33 as the green line while the blue line in the same figure represents a measured curve $\tilde{B}\left|J_1\left(\frac{4\pi}{\lambda}d_z\right)\right|$. The error in the magnitude distribution $d|U_{J1}|$ produces an error in the amplitude distribution dd_z as outlined also in Figure 3.33. The error in amplitude distribution as a function of amplitude is plotted in Figure 3.34. At first sight direct inversion approach is much more sensitive for error distortions. There is a crucial difference in response to presence of the multiplicative error between phase modulated holography and the direct inversion. When averaging a great number of measurement, the standard deviations is expected to approach zero $\sigma(\tilde{B}) \to 0$. In case of the phase modulated holography, the ratio of magnitude distribution pairs (3.73) results in sensitivity of the method proportional only to the standard deviation $\sigma(\tilde{B})$ via the coefficient of variance $c_v = \frac{|\sigma(\tilde{B})|}{\tilde{B}_{AVE}}$. Hence, the averaging of great number of measurement also suppresses effect of the multiplicative noise (theoretically) down to zero $c_v \to 0$. On the other hand, averaging of great number of measurement in case of direct inversion approaches to value $\tilde{B} \to \tilde{B}_{AVE}$, which may not be equal to one and therefore still the multiplicative error is presented.

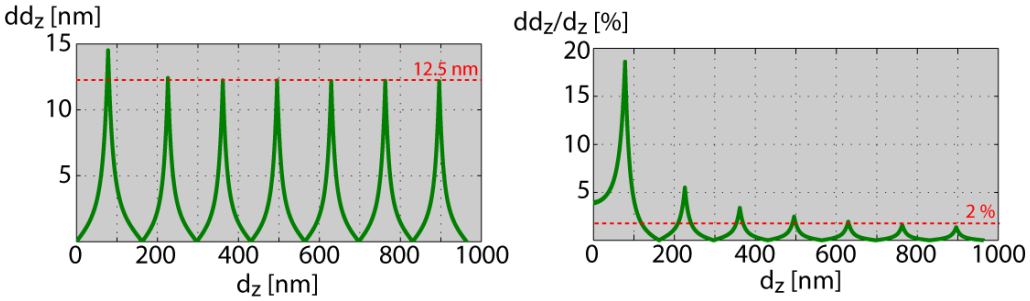

Figure 3.34: Error of measurement using direct inversion for amplitude retrieval as a function of measured amplitude of vibrations. Relative error is introduced in the right-hand plot.

Recently, error analysis has been largely replaced by uncertainty analysis [70]. In order to convert error contributions coming from (3.77) into standard uncertainties, one has to estimate probability distribution of the individual distortion sources. The histogram of phase offsets introduced in Figure 3.29 tends

to evince the Gaussian profile corresponding to the normal distribution with estimated standard deviation $\sigma(\varepsilon) \approx 0.1\,rad$. This value was estimated from behavior of Gaussian function when approximately 95% values lie in an interval with length of two standard deviations from the mean value. Thus, the standard uncertainty

$$u_\varepsilon = \frac{\lambda\,\sigma^2(\varepsilon)}{32\pi} sin\left(\frac{8\pi}{\lambda} d_z\right) \tag{3.83}$$

represents uncertainty generated by incorrect phase offset. The second source of distortions considered within this analysis is the multiplicative factor $\tilde{B}$. As shown in Figure 3.30 the values $\tilde{B}$ are scattered according to the rectangular probability distribution within interval $\tilde{B} \in \langle 0.9955, 1.016 \rangle$ with the standard deviation $\sigma(\tilde{B}) \approx \frac{\tilde{B}_{max} - \tilde{B}_{min}}{2\sqrt{3}} = 0.018$[1]. It follows relation

$$u_{\tilde{B}} = \frac{\lambda\sigma(\tilde{B})}{4\pi} sin\left(\frac{8\pi}{\lambda} d_z\right). \tag{3.84}$$

holding for standard uncertainty of multiplicative parameter distortion. Analogously to the error analysis, the third source of uncertainty is the correction function

$$u_\Delta = \frac{\partial\Delta(d_z)}{\partial d_z} dd_z. \tag{3.85}$$

Last considering source of distortion is repeatability (type A uncertainty while the above are all type B uncertainties) determined by relation (3.47):

$$u_A = 0.05 + 0.01\,d_z. \tag{3.86}$$

Formulas (3.83)-(3.86) can be used for definition of so called combined standard uncertainty:

$$u_c = \sqrt{{u_\varepsilon}^2 + {u_{\tilde{B}}}^2 + {u_\Delta}^2 + {u_A}^2} \tag{3.87}$$

comprising all important sources of distortions.

Although the combined standard uncertainty u_c is usually used to express the uncertainty of measurement results, sometimes is required a measure of uncertainty that defines an interval about the measurement result. The measure of uncertainty intended to meet this requirement is termed the expanded

[1] This is only a different approach of how to calculate $\sigma(\tilde{B})$ comparing to value introduced in error analysis.

uncertainty and is obtained by multiplying u_c by a coverage factor k: $U = ku_c$. In general, the value of the coverage factor k is chosen on the basis of the desired level of confidence to be associated with the interval defined by $U = ku_c$. Typically, $U = 2u_c$, that defines an interval having a level of confidence of approximately 95 %.

For illustration, combined standard uncertainties and expanded uncertainties for some values of measured amplitude of vibrations d_z are presented in the table below.

	$d_z = 10\ nm$	$d_z = 100\ nm$	$d_z = 1000\ nm$
$u_c\ [nm]$	0.4	1.3	10.1
$d_z \pm U\ (k = 2)$	$(10.0 \pm 0.8)\ nm$	$(100.0 \pm 2.6)\ nm$	$(1000.0 \pm 20.2)\ nm$

Another important parameter of a measurement technique is its time consumption. In general, operators demand a quick and accurate measurement. Therefore huge application software comprising of numerous packages was developed. The whole system (built in MATLAB R2013a environment) treats with control and settings of all hardware components as well as with the complete data processing. The measurement time strongly depends on the employed hardware and software equipment (PC: intel core i5 3570 CPU, 8GB RAM). In our arrangement we must control HW components: two Rigol DG 4102 waveform generators, AVT Stingray camera (6.5 FPS, 2048 x 2056 pixels). The measurement procedure consists of four steps:

- Initializing of the hardware (3.8 s)
- Capturing and saving of sequence of phase-shifted digital holograms at steady state of the object as a reference (1.4 s)
- Capturing and saving of phase-shifted digital holograms sequence at oscillating state with different phase-offsets (5.7 s)[1]
- Loading data and data processing (6.7 s)[1]

In total, the whole procedure takes less than 18 s counted from the start of the measurement to visualization of a distribution of vibration amplitudes over the whole surface.

[1] Stands for 4-step phase shifting technique

4 Experiments

4.1 Measurement of piezoelectric transformers

Years of experiments	2011-2012
Heterodyne technique	YES
Frequency modulation	YES (n=1)
Phase modulation	NO
Amplitude distribution retrieval technique	Direct inversion within first monotonous interval of the Bessel function
Publications	[37], [37], [47], [49], [50], [71]

A piezoelectric transformer (PT) is a device used for the transformation of alternating electric voltage by the means of ultrasonic vibrations. It utilizes reverse piezoelectric effect in the input part and direct piezoelectric effect in the output part. The best transformation ratio is achieved at the mechanical vibration resonance. The measurement of out-of-plane displacement as well as the shapes of transformer vibration modes near resonant frequencies provides useful data, applicable in theoretical research of piezoelectric transformers behavior as well as in practical applications. A typical example is an effect of a transformer's properties as a function of its mechanical mounting.

PTs are used e.g. for Cold cathode fluorescent lamp electronics, high voltage generator for cold plasma, mobile phone battery recharging etc. High transformation ratio at no-load conditions is a specific feature of the PT's operation. PT applications are complex, including specific transformer mounting, wiring and driving circuit electronics. A very important parameter for characterization pf PTs is out-of-plane displacement distribution, which can be measured by time average holography. Maximal values of vibration amplitudes appearing on surface of PTs are in range of tens of nanometers. Therefore one has to use a sensitive method for very small vibration amplitudes – frequency modulated time average digital holography introduced in 3.3.

The experimental arrangement for measurement is outlined in Figure 4.1. The interferometer is based on the Mach-Zehnder type of a holographic interferometer. The laser beam has a wavelength of 532 nm and power of 100

mW. After the mechanical shutter, the beam is split by the polarizing beam splitter, equipped with half wavelength retardation plates in two beams. Half wavelength retardation plates help set the intensities in both beams as well as the polarization of each beam. The first beam acts as a reference wave and could be further attenuated if necessary by a set of gray filters placed in filter wheels. Each beam is frequency shifted by an acousto-optic frequency modulator - Bragg cell, with its working frequency of 40 MHz. The Bragg cell placed in the reference arm was frequency modulated by the frequency of the PT in order to increase the sensitivity of the method for small amplitudes.

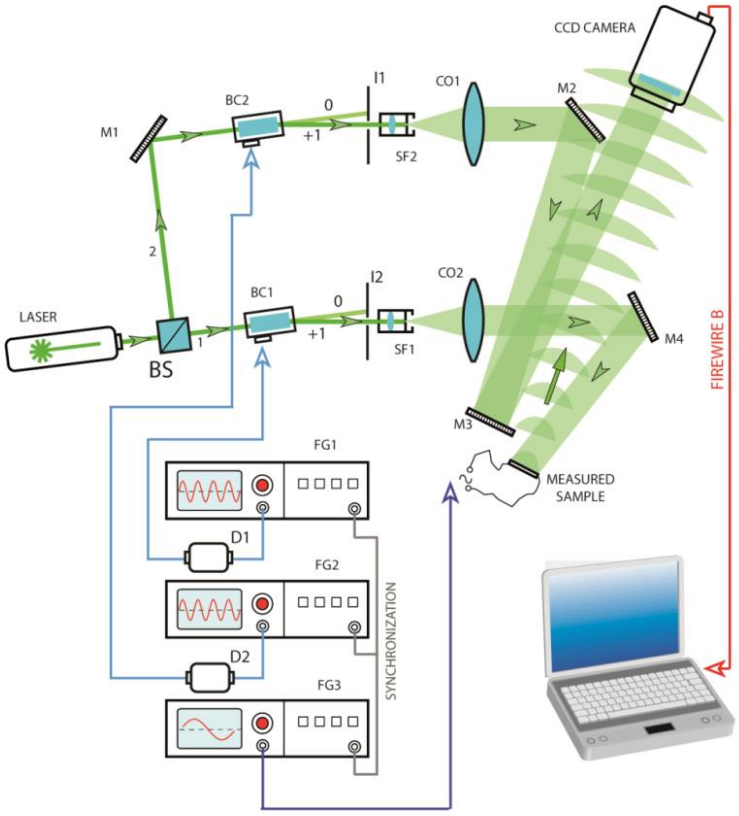

Figure 4.1: Outline of the experimental arrangement used for PT measurement employing components: BS – beam splitter, SF – spatial filter, BC – Bragg cell, M – mirror, CO – collimating objective, FG – function generator, D – driver.

Moreover the heterodyne detection was employed. The both beams are further spatially filtered and collimated. After two reflections on mirrors M2 and M3, the reference beam hits CCD. The object beam illuminates the sample and the light scattered from its surface impinges on the CCD sensor. The setup is designed as an off axis Leith-Upatnieks scheme. The angle between the beams is set to be approximately 3°. The camera is an AVT Stingray - F 504 with

a resolution of 2045 × 2056 pixels, each pixel having the size 3.45 µm × 3.45 µm. The camera is connected to the computer via a Fire Wire B interface enabling a frame rate of 6.5 FPS. The image from camera – digital hologram – is cropped to 2048 × 2048 pixels due to Fast Fourier Transform (FFT) in the reconstruction process. A sequence of 16 phase-shifted frames was captured and processed in a way presented in 3.2. Retrieval of amplitude of vibrations distribution was based on direct inversion method, since phase modulation had not been developed yet.

The measurement was performed for ring PTs and disc PTs with a different diameter and mounting. All piezoelectric transformers are made of hard lead zirconate titanate ceramics (PZT, APC841 type).

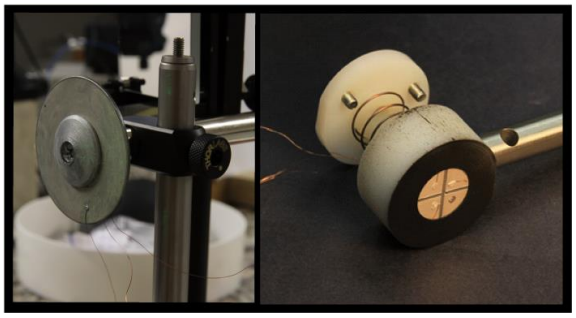

Figure 4.2: Measured ring piezoelectric transformer (left) and 4-segment disc piezoelectric transformer placed in manufactured holder (right).

The first measured samples were ring PTs with a diameter of 40mm and thickness of 1mm. The electrodes were designed in the shape of concentric rings. For the purpose of mounting, all transformers have a hole in the center and they are fixed onto a precisely machined shaft by the flange as can be seen in Figure 4.2. For every mounted sample, its resonant frequencies were measured and then the holographic method for out-of-plane vibrations measurement was applied.

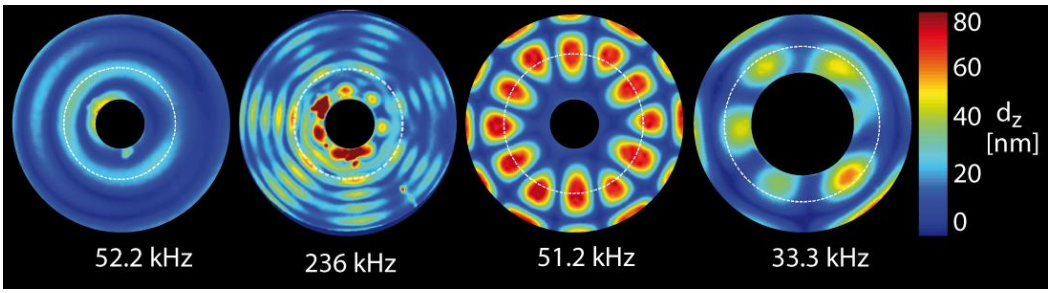

Figure 4.3: The out-of-plane displacement of ring piezoelectric transformer at resonant frequencies driven by $30V_{pp,}$ dashed white concentric circles represent the position of borderlines between electrode segments with diameters 8 mm and 20 mm.

The transformers were driven by voltages of 15, 30, 45, 60 V_{pp} and the out-of-plane displacement distributions near resonant frequencies were measured, data was processed and results were visualized by in-house developed software. Some illustrative examples are shown in Figure 4.3.

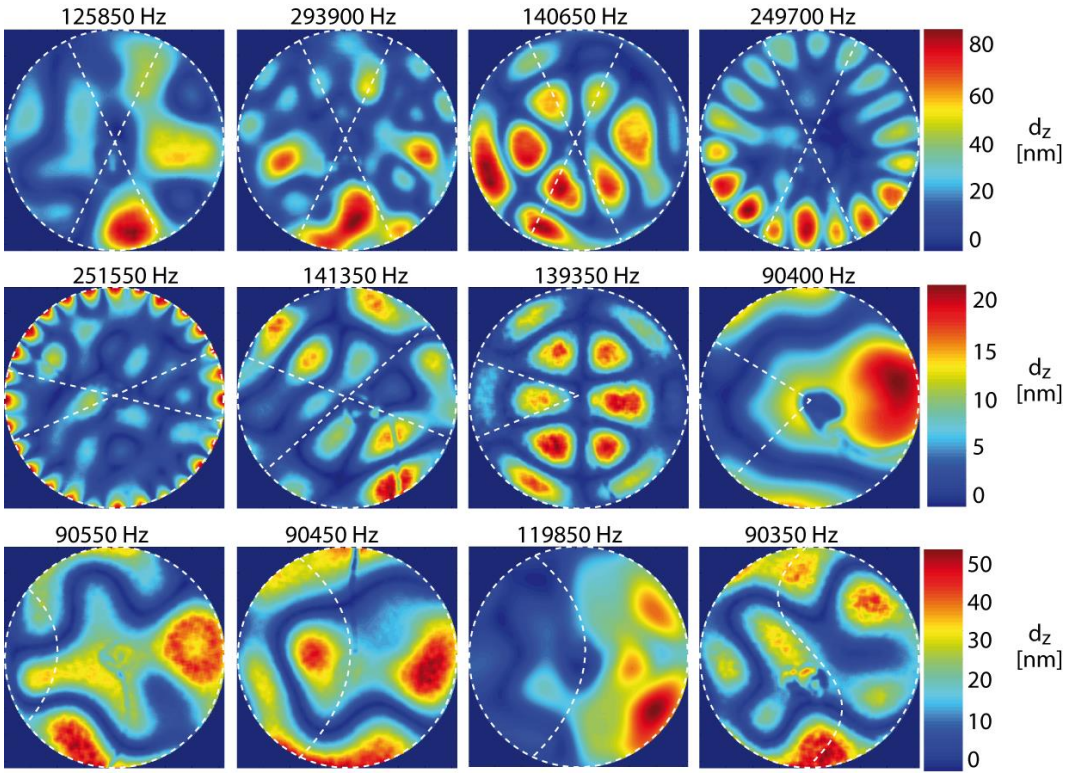

Figure 4.4: The out-of-plane displacement of disc piezoelectric transformers with differently shaped electrodes driven by $30V_{pp}$ at resonant frequencies. A diameter of a transformer is 20 mm and the dashed white lines represent position of borderlines between electrode segments.

The second type of studied PTs were disc PTs with diameter of 20 mm and thickness of 1 mm. Electrodes were designed in different shapes such as crescent-shaped, 2-, 3-, 4-segments PT, ring-dot or wedge V shape. The PTs were placed in a manufactured holder (see Figure 4.2). The disc was pushed by a spring from the back-side to ensure that the pressure would be approximately identical during all measurements. The PTs were driven by a voltage of 30 V_{pp}. Some results of disc PT measurement are shown in Figure 4.4. The intensity of pseudo-color image corresponds to the amplitude of the vibration according to the colorbar on the right-hand side. Since the experiment was conducted without employment of phase modulation, only magnitude of oscillation amplitude is measured. The sign of mechanical phase is lost.

In order to obtain better knowledge of PTs behavior, some additional measurements were performed:

- Infrared Camera Measurement- a surface temperature distribution was obtained using an infrared camera (Ti55FT, Fluke Corp.). The images were acquired after about 2 min of a steady operation in high power regime (PTs were driven by a power amplifier (HSA4052, NF Corp.) at constant amplitude and frequency).
- FEM Simulation - a harmonic analysis of PTs was employed using software ANSYS in order to predict PT behavior prior to its fabrication. Full 3D models of all tested PTs were created, applied material properties are given in Table I. In order to obtain characteristics under load a resistor element was also introduced.

The vibration distribution of a PT is affected by operating mode and clamping. When operated in higher power regime, the vibrations are connected with more pronounced temperature distribution. Infrared camera measurement revealed the most critical parts when operated in high power regime. These were usually the areas close to the input lead contact. The surface temperature was typically below 60°C, however, it reached 100°C for smile 1/2 D PT. Holographic interferometry and FEM simulation enabled normal displacement visualization. Measured vibrations distribution were affected by electrode placement imperfection, PT clamping. The influence of the electrode pattern symmetry was clearly visible in the vibration displacement distribution. Results of the aforementioned techniques are shown in Figure 4.5.

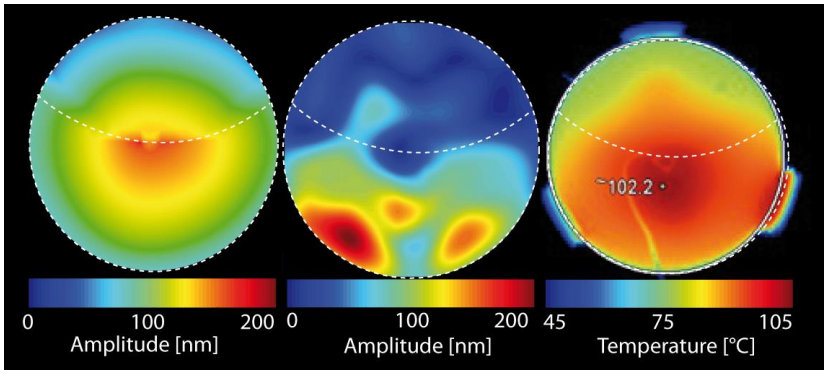

Figure 4.5: Investigation of disc PT by different techniques. Namely it is FEM simulation (left), holographic measurement (middle) and infrared camera visualization (right).

4.2 Comparison of frequency modulated technique to single point laser interferometer

Years of experiments	2012 - 2013
Heterodyne technique	YES
Frequency modulation	YES (n=1)
Phase modulation	NO
Amplitude distribution retrieval technique	Direct inversion
Publications	[38], [72]

The experiment introduced in this chapter shows the comparison of amplitude of vibration measurement simultaneously performed with three different methods on the same sample. The aim is to experimentally prove the capability of the frequency modulated time average digital holography combined with heterodyne technique and phase averaging. The methods used as a bench mark are Doppler vibrometry performed with commercial single point vibrometer (Ometron) and single point interferometer in Michelson configuration which is improved with lock in principle.

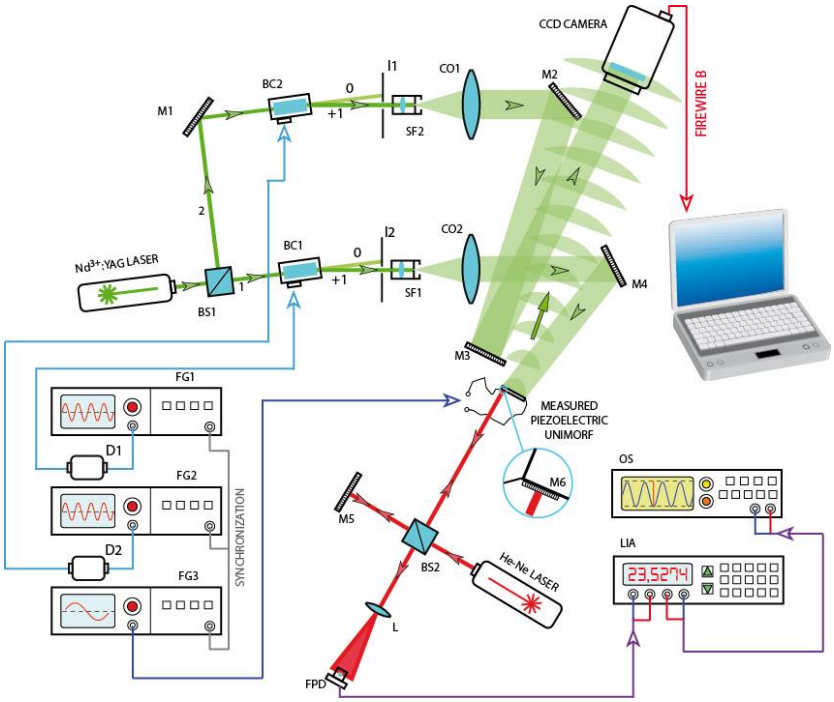

Figure 4.6: Holographic and interferometric arrangements for small amplitude vibration measurement.(BS-beam splitter, M-mirror, SF spatial filter, CO-collimating objective, O-focusing objective, FG-function generator, OS – oscilloscope, LIA – lock-in amplifier, L- lens, FPD – fast photodiode).

Figure 4.6 outlines the measurement arrangement which includes two of three mentioned different measurement methods. Considering the readability of the scheme, the vibrometer measurement is not depicted there. Digital holographic measurement is based on the Mach-Zehnder type of holographic interferometer having the same parameters when compared to piezoelectric transformer measurements in chapter 4.1. The data processing is also performed in the same way as in 4.1.

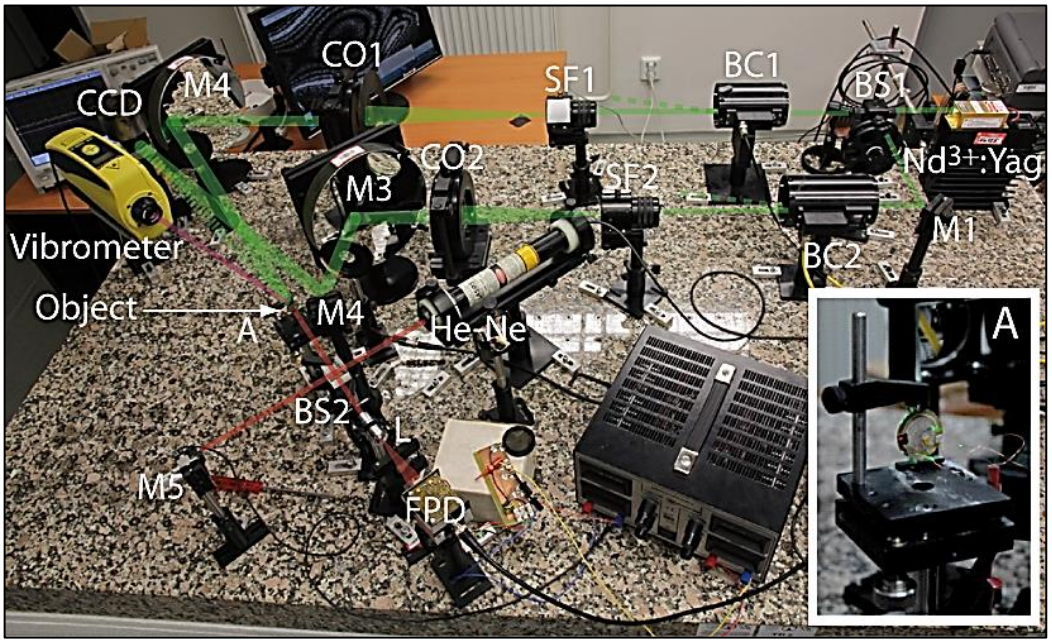

Figure 4.7: Photography of the experimental arrangement with highlighted optical paths. The arrangement combines three different techniques. The inner image (A) presents the measured piezoelectric element - object.

For the Michelson interferometric measurement a stabilized He-Ne laser with a wavelength of 632.8 nm is used as a light source. The beam is divided by a beamsplitter BS2 to two interferometer arms. The sample with the mirror M6 is placed at the first arm. The sample can vibrate with the frequency of the applied electric field from AC source. An active element, holding a constant phase difference $\pi/2$ between waves from both arms, is situated in the second reference arm. Beams are joined after reflection, and the interference pattern is projected to the photodiode by the lens. The lock-in amplifier (LIA) and, simultaneously, the oscilloscope (OS) are used for signal detection. With use of lock-in amplifier technique the Michelson interferometer enables to measure amplitudes in the order of 10^{-12}m.

The vibrometer was precisely set to measure at the same point as the interferometric method. Since the holographic method measures in a whole-field, after the data evaluation, it was necessary to consider just the values from the area, which correspond to single-point methods.

The object under investigation is piezoelectric unimorph membrane. The measurement was realized for three different driven frequencies: 2 khz, 9khz and 13 khz. For every frequency, a set of measurement for different excitation voltages (10 V, 20 V, 30 V, 50 V, 100 V, 200 V) of the unimorph was performed. Due to thermal properties and relevance of measurements, the different method measurements were done in the same time. Detected harmonic voltage at the photodiode is proportional to the intensity so it is possible to measure voltage on the photodiode. The harmonic part of the signal can be detected and amplified by lock-in amplifier technique. The lock-in amplifier compares the detected voltage with the reference signal from the voltage generator. This reference signal has a frequency of the electric field applied on the sample. The output voltage from the lock-in amplifier is proportional to the product of measured and sinusoidal reference voltages. This comparison of signals can be made at a desired integration time, much longer than is the period of applied AC voltage. Therefore the device is able to detect a very small signal of reference frequency from a high-noise signal, where the noise level is about three orders of magnitude higher. This amplifier measures effective voltage so the amplitude of harmonic vibration of the sample can finally be calculated from the equation

$$d = \frac{U_{OUT}}{U_{PP}} \frac{\lambda}{\sqrt{2\pi}}, \qquad (4.1)$$

where U_{OUT} is the voltage detected by the lock-in amplifier, U_{PP} is the peak to peak voltage and λ is wavelength of used laser.

In Figure 4.8 the measured data for 13 kHz drive frequency obtained by simultaneous measurement are plotted. From the physical point of view, the linear behavior was predicted. Therefore, the deviation from linearity as a reliability factor was also calculated and visualized in Figure 4.8. In Figure 4.9 the relative deviations between methods are plotted. These deviations are calculated as an amplitude difference between the two methods divided by the value of a reference method. As a reference method it was considered the lock-in interferometric method. On the basis of obtained data, one may claim all methods fulfill linearity requirements and the deviation between methods

(especially for amplitude larger than 1 nm) is in tolerance range of the methods. The same measurement for driven frequency 2 kHz (where the range of amplitudes is different) is presented in Figure 4.11 and Figure 4.12.

The interferometric lock-in method and the vibrometer based method are generally considered as a reliable and precise method and it was shown, the holographic method has comparable parameters. Some results obtained by the holographic method are presented in Figure 4.13

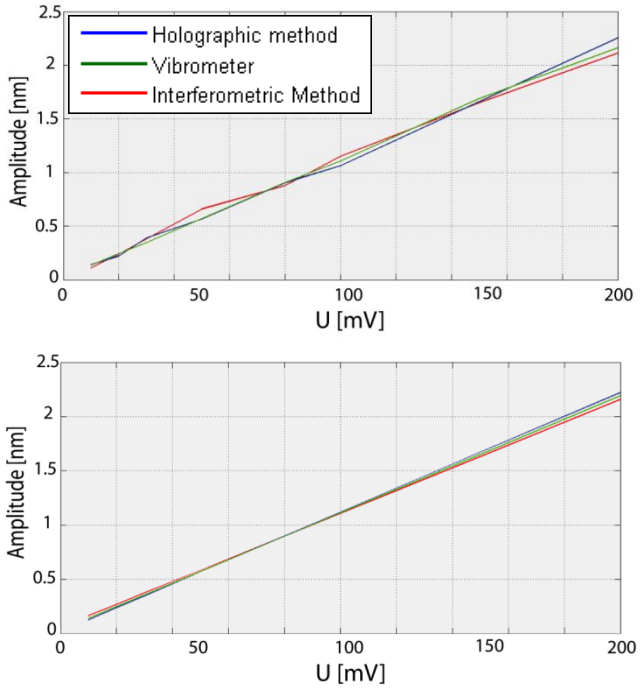

Figure 4.8: (up) Results of measurement (holographic method – blue line, vibrometer based method – green line, interferometric lock-in method – red line); (down) linear regression of the measured data. The linearity of holographic method, vibrometer based method and interferometric lock-in method are 99,72%, 99,85% and 99,55%.

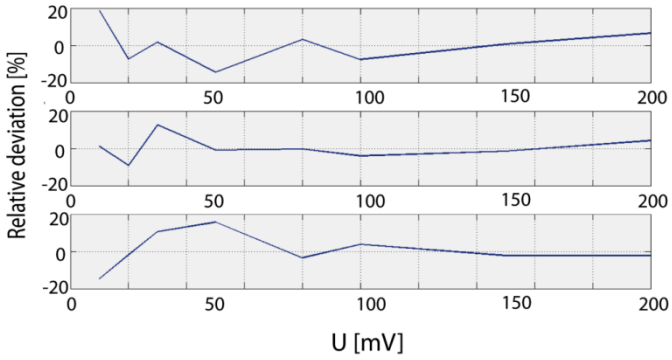

Figure 4.9: (up) Relative deviations between holographic and interferometric method (the average deviation is 7,513%); (middle) relative deviations between holographic and vibrometer method (the average deviation is 4,25%) and down - relative deviations between vibrometer and interferometric method (the average deviation is 6,85%);

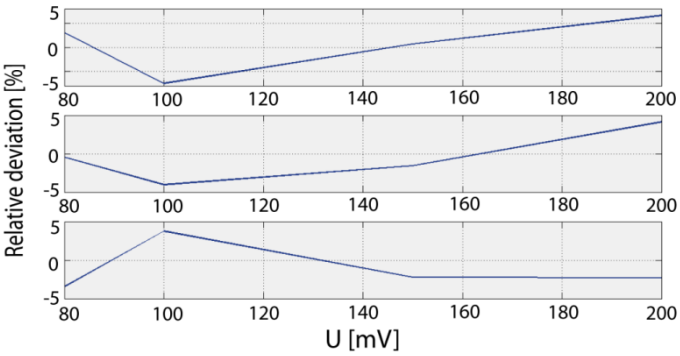

Figure 4.10: Relative deviations between methods (same ordering as in previous figure) for amplitudes larger than approximately 1nm with average deviation 4,47%, 2,54% and 2,93%.

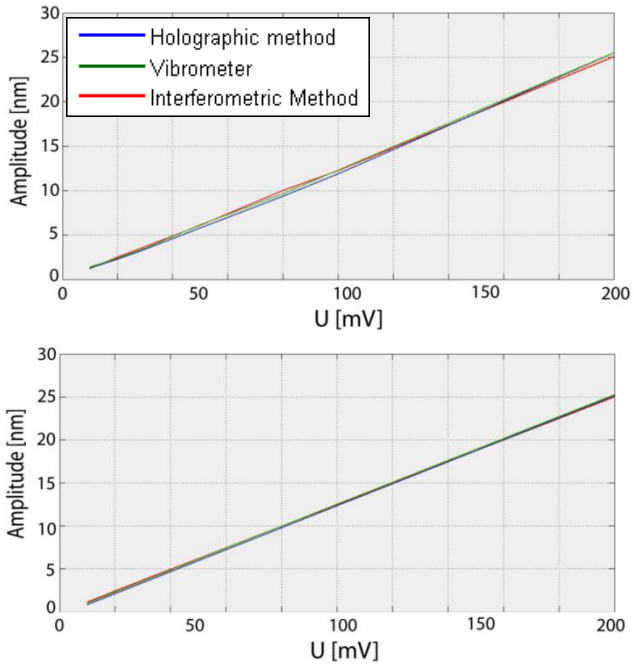

Figure 4.11: (up) The measured data (holographic method – blue line, vibrometer based method – green line, interferometric lock-in method – red line); (down) linear regression of measured data. The linearity of holographic method, vibrometer based method and interferometric lock-in method are 99,73%, 99,85% and 99,90%.

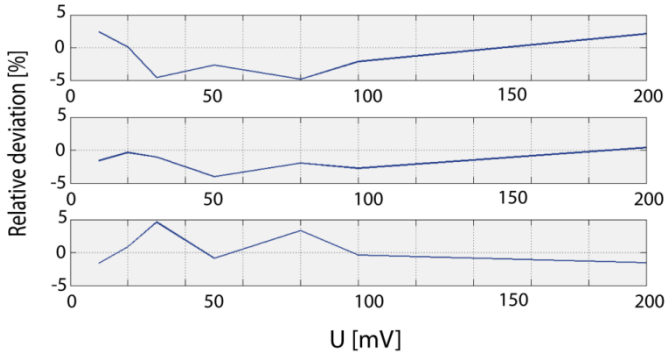

Figure 4.12: Up - relative deviations between holographic and interferometric method, middle - relative deviations between holographic and vibrometer method and down - relative deviations between vibrometer and interferometric method. The average deviation is smaller than 4%.

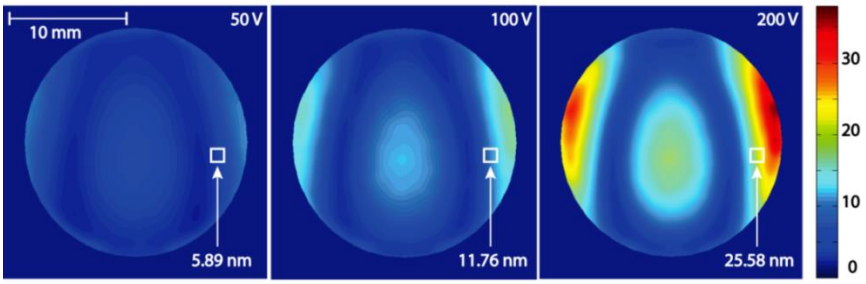

Figure 4.13: Results of piezoelectric unimorph measurement for driven frequency 2 kHz and excitation voltages 50V, 100V and 200V by digital holography. The white square denotes an area corresponding to the measuring area of the single point methods.

4.3 Noise suppression in curved glass shells using macro-fiber-composite actuators

Years of experiments	2014 - 2015
Heterodyne technique	YES
Frequency modulation	YES (n=1, n=10, n=50)
Phase modulation	YES
Amplitude distribution retrieval technique	Least square approach and 13-step phase stepping technique
Publications	[51]–[55]

This chapter introduces some experimental results of measurement during the semi-active control of noise transmission in a curved glass shell with attached piezoelectric macro fiber composite (MFC) actuators. The semi-active noise control is achieved via active elasticity control of piezoelectric actuators by connecting them to an active electric shunt circuit that has a negative effective capacitance. Using this approach, it is possible to suppress the vibration of the glass shell in the normal direction with respect to its surface and to increase the acoustic transmission loss of the piezoelectric MFC-glass composite structure. The effect of the MFC actuators connected to the negative capacitance shunt circuit on the surface distribution of the normal vibration amplitude is studied using phase and frequency modulated time average digital holography (PFMTADH). The frequency dependence of the acoustic transmission loss through the piezoelectric MFC-glass composite structure is estimated using measurements of the specific acoustic impedance of the curved glass shell. The specific acoustic impedance is measured using two microphones and a laser

Doppler vibrometer (LDV). The results from the LDV measurements are compared with the holographic data. The results of the experiments show that using this approach, the acoustic transmission loss in a glass shell can be increased by 35 dB in the frequency range around 270 Hz and by 31 dB in the frequency range around 720 Hz. The experiments indicate that PFMTADH measurements provide an efficient tool that can be used for fast and accurate measurements of the acoustic transmission loss in large planar structures.

Due to their physical nature, noise and vibrations are accompanied with the flow of mechanical or acoustic energy. Propagation of acoustic energy and the reflection of acoustic waves at interfaces of two different materials are controlled by a physical property called specific acoustic impedance z_m. Specific acoustic impedance of a planar structure is a frequency-dependent parameter defined as an acoustic sound pressure p divided by particle velocity v:

$$z_m = \frac{p}{v}, \tag{4.2}$$

The sound shielding efficiency of the noise isolation devices (NID) can be expressed using the physical quantity called acoustic transmission loss, which is defined as a ratio of the acoustic powers of the incident and transmitted acoustic waves and usually expressed in the decibel scale. For the purposes of our study, it is convenient to express the acoustic transmission loss (TL) in terms of the specific acoustic impedance of the NID:

$$TL = 20log_{10}\left|1 + \frac{z_m}{2z_a}\right|, \tag{4.3}$$

where z_a is the characteristic acoustic impedance of air. From (4.3)(4) follows that large values of the TL correspond to large values of the specific acoustic impedance z_m of the NID. In the passive noise shielding approach, the large values of z_m can be achieved by increasing the weight of the sound barrier. Such a situation is often unacceptable in real-world devices. Therefore, it is very challenging to increase the value of z_m to a great extent with keeping the weight of the structure as small as possible.

Figure 4.14 outlines the Mach-Zehnder type of holographic interferometer used for the measurement. The laser beam has a wavelength of 532 nm and a power of 150 mW. Similarly to previous experiments, behind the mechanical shutter, the beam is split in two by the polarizing beam splitter equipped with half-wavelength retardation plates. Half-wavelength retardation plates help to set

the intensities in both beams as well as the polarization of each beam. The first beam acts as a reference wave and it could be further attenuated if necessary by a set of gray filters placed in the filter wheels. Each beam is frequency-shifted by means of an acousto-optic frequency modulator - Bragg cell with a fundamental frequency of 40 MHz. It is important to note, that measurement of piezoelectric MFC-glass composite structure requires great dynamic range of the method. Measured amplitudes of vibration start from nanometers at frequencies for which the negative capacitance (NC) shunt circuit is optimized. On the other hand, when the negative capacitance shunt circuit is disconnected (or detuned), the amplitudes of vibration at resonant frequencies of the curved glass reach units of microns. Therefore the frequency modulation as described in chapter 3.3 must be employed.

The beams exiting the Bragg cells are spatially filtered and the reference beam is collimated. The object beam illuminates the measured window and the light scattered from its surface interferes with the reference wave. The negative lens reduces the imaging angle and the measured window having size of 420 × 300 mm can thus be measured. The setup is designed as an in-line scheme combined with heterodyne technique of holograms acquisition (see chapter 3.2) in order to maximize the lateral resolution and suppress the overlapping diffraction terms.

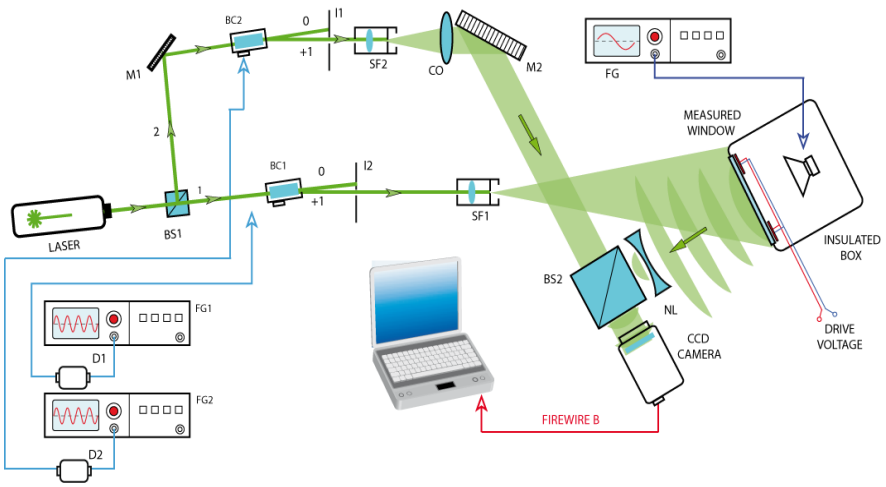

Figure 4.14: An outline of the experimental arrangements used for glass shell measurement. Negative lens (NL) is used to reduce the imaging angle. Other components: BS-beam splitter, M-mirror, SF spatial filter, CO-collimating objective, O-focusing objective, FG-function generator, BC – Bragg cell, D – driver.

The measurement of the transmission loss by acoustic method was conducted at frequency range from 200 Hz to 800 Hz. Results are represented by solid green

line in Figure 4.16. Subsequently, frequencies of 290 Hz and 735 Hz were identified with a minimum value of the acoustic transmission loss, which corresponds to dominant vibration modes of the curved glass shell. Finally, two values 270 Hz and 720 Hz of a frequency ω_o were chosen, for which the NC was adjusted (marked by the violet and the blue circles). For more detailed technical description as well as physical background regarding the noise suppression, see the original papers.

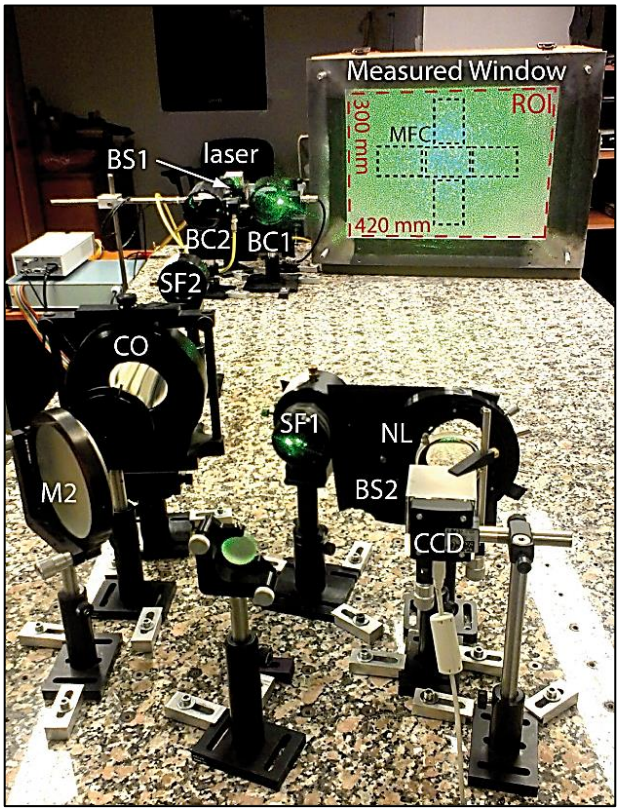

Figure 4.15: A photography of the experimental arrangement. ROI (region of interest) delineates the investigated surface of the glass shell. Position of MFCs is outlined by black dashed rectangles.

The profiles of the vibration modes of the curved glass shell were measured using digital holography in the frequency ranges from 265 Hz to 275 Hz and from 715 Hz to 730 Hz in the two situations, when the NC was disconnected (OFF) and when the NC was connected and adjusted at the frequency 270 Hz, 720 Hz, respectively. Moreover, the NC was slightly detuned by capacity value in order to see the influence of this parameter. Figure 4.16 down shows the results. Values within each figure of amplitude distribution introduce RMS (Root Mean Square) value of the amplitudes over the whole surface. Two interesting features can be observed from the results.

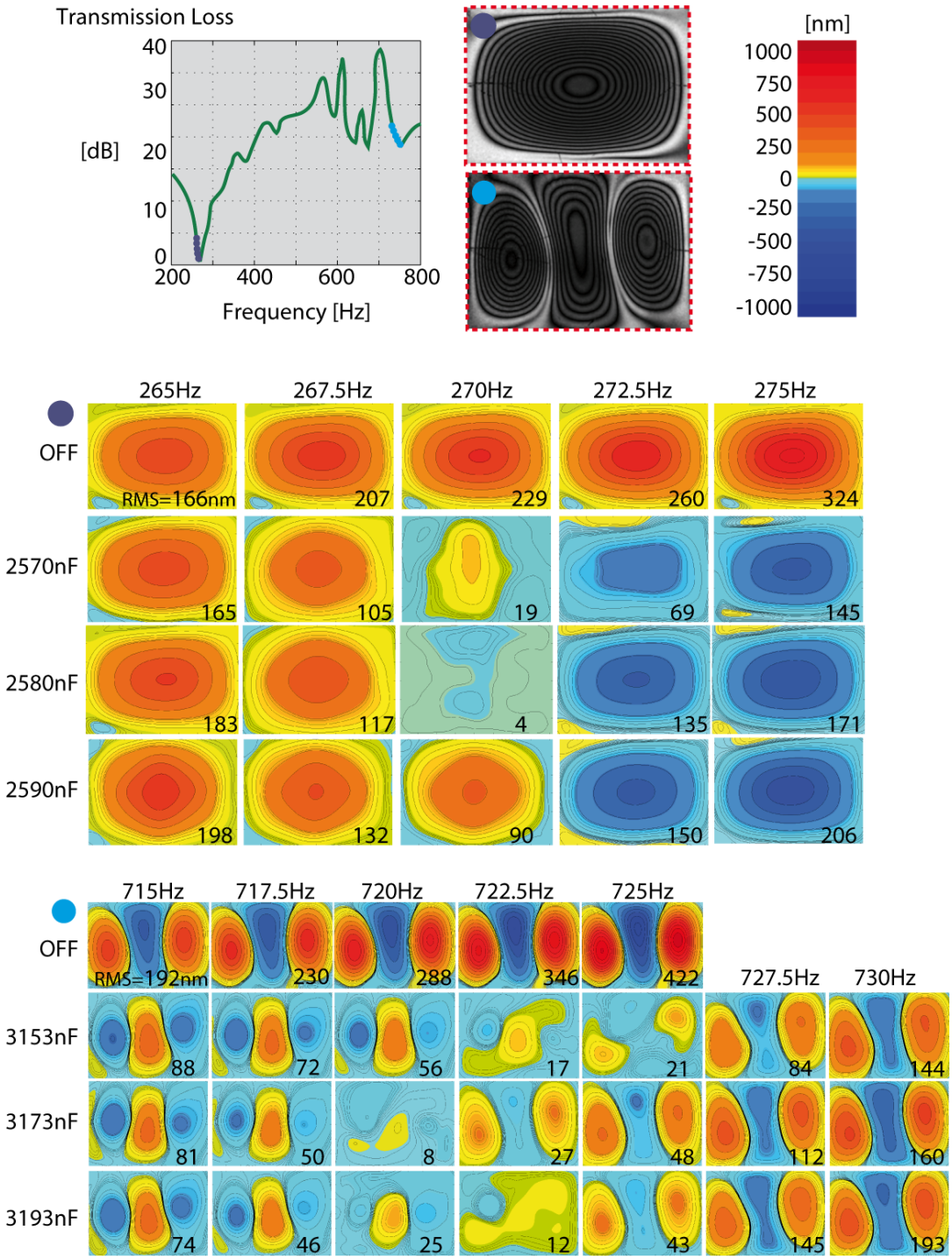

Figure 4.16: Results of experiments carried out on the glass shell with attached MFC for noise suppression. The 1D plot shows result of acoustic measurement. Magnitude maps of ROI measured at 270 Hz and 720 Hz by holographic method are introduced in the red dashed rectangles. The false color maps represent amplitudes of vibration within the ROI while the NC circuit is ON or OFF and for different values of capacity of the NC circuit. One should note that the colorbar is not linear due to large dynamic range of the measurement.

Apparently, one can see the suppression of the amplitude of vibrations in situation when the NC circuit was on and off. That corresponds to an increase in the TL by approximately 35 dB respectively 31 dB due to the effect of the NC

circuit. The sign of the amplitude is also worth noting. The sign changes when the frequency passes the optimized value or a resonant frequency of the system. This behavior is important from the metamaterial engineering point of view. It also shows importance of phase modulation in time average digital holography bringing the advantage of the amplitude sign sensitivity, which would remain otherwise hidden.

Conclusion

This dissertation is aimed to research and development of an advanced method for amplitudes of vibration measurement based on the digital holographic approach. The vibration analysis is massively used in many branches of industry as well as in research and development. The high demand for contactless, full-field and very sensitive method for vibration measurement combined with its complete lack let us to start with the method development. Although there is a vast amount of techniques for vibration analysis that are based on different principles, digital holography has offered new opportunities. Method for vibration measurement based on digital holography is called time-average digital holography (TADH). TADH is a whole-field method with great lateral resolution and unprecedented sensitivity. On the other hand, since its discovery, TADH has contended with drawbacks like a limited measurement range or lack of automatable quantitative analysis. The aim of this work was to push the limits of TADH and make the method easy-to-use and applicable in vast range of different applications. Based on previous research carried out in our research group I employed acusto-optical modulator (Bragg cell) into the experimental arrangement and combined advantages resulting from frequency and phase modulation of a reference or/and an object wave. The new method can be called phase and frequency modulated time average digital holography (PFMTADH). All theoretically derived impacts on the method caused by my inventions were experimentally verified by measurement of a beam cantilever.

As described in detail in chapter 3.1, different frequency modulation of the object and the reference wave in experimental arrangements results in a temporally harmonic development of intensity values in digital hologram. This expresses the relative phase variation between the both waves. In this way, an arbitrary phase shift between frames of the digital sensor can be used for solution of a set of equations by means of phase-shifting algorithms. As a result, one obtains wavefield in the digital hologram plane that is free of undesired diffraction orders called d.c. term or twin image. Thus a bandwidth of the object in a digital hologram plane can be extended up to the bandwidth of the whole digital hologram. This leads to an improvement of the lateral resolution within the surface of the object. The experiment carried out in the chapter 3.1 shew the improvement of lateral resolution corresponding to the object surface about a factor of two when compared to the non-modulated technique. In a frequency domain, the object bandwidth (in horizontal direction) accounts for more than

90% of the whole bandwidth of the digital hologram. These numbers are indicative (based on experimental data in selected experiment), since lateral resolution in Fresnel holography depends on laser wavelength, parameters of used digital camera and distance between object and the camera.

In addition, as a consequence of better lateral resolution, the measurement range of the method in case of large amplitudes is increased. Better lateral resolution inevitably mitigates the sampling criterion for the Bessel fringe pattern modulating the magnitude field over the object surface. Therefore larger amplitudes exhibiting a denser fringe pattern can be resolved and evaluated.

Due to combination of more digital holograms in phase-shifting technique, signal-to-noise ratio is also increased when compared to the single captured digital hologram. The demonstrative experiment exhibited more energy within the spectral domain of the object about 30%.

Typical frequency modulation in order to use the phase-shifting technique ranges in fractions of frame rate of the digital camera (units of Hz). However, when the reference wave is further modulated by an integer multiple of frequency at which the object oscillates, the order of the Bessel function defining the fringe pattern varies in connection with the integer value. Therefore one can easily make use of properties of different orders of the Bessel function. For very small amplitudes it is beneficial to modulate the reference wave by frequency of the object oscillations. This leads to the first order Bessel function that exhibits sufficient slope for small values of vibration amplitudes. In chapter 3.2, I experimentally established the threshold of the smallest measurable amplitude to be under 0.1 nm. On the other hand, in the case of large vibration amplitudes one can take advantage of the fact that the locations of the zeros of the Bessel functions are spread apart for increasing order of the Bessel function. Experimentally I reached amplitude of vibration larger than 9 um measured with modulation of reference wave by 150th multiple of the objet oscillations. The dynamic range of the measurement has been increased due to frequency modulation up to 10000.

The second major challenge of the dissertation was aimed at retrieval of vibrations amplitude values coded in the Bessel fringe pattern due to lack of fully-automatic procedure, which I designed and developed for this purpose. The method uses Bragg cells in the holographic arrangements that modulate phase of the reference wave. A sequence of phase modulated fringe patterns is reconstructed and with the use of suitable phase-shifting algorithm, the amplitude

of vibrations can be straightforwardly computed. This procedure is elaborately introduced in the chapter 3.3 together with appropriate experimental verification. A repeatability of the method was determined on the basis of experimental study to be 0.01 of measured amplitude in nm plus bias 0.05 nm having an impact only for very small amplitudes.

In the chapter 3.4 I verified that frequency and phase modulation can be arbitrary combined in order to exploit benefits of the both approaches. The dynamic range of 10000 was reached also with the employment of the phase modulation. Further in the chapter 3.4 the sources of possible distortions influencing the accuracy of the method are discussed. The contributions of individual distortions are included in a resulting formula describing the total error of the measurement. Individual contributions to the total error are experimentally established and substitute into the error equation. Finally I determined the uncertainty of the method. As an example, expanded uncertainty (k=2) was calculated for nominal amplitude of vibrations 10 nm to be (10.0 ± 0.8) nm and (1000.0 ± 20.2) nm for nominal value 1000 nm.

The developed techniques were applied in many experiments. Some of the experiments were selected in order to demonstrate the capability of the method. Measurement of disc and ring piezoelectric transformers is introduced in the chapter 4.1. The characteristic feature of this measurement was very small amplitudes of vibrations of the transformers. Maps of vibration amplitudes over the transformers surface with differently shaped electrodes at resonant frequencies were measured and the results have been used for further research in the field of piezoelectricity and the transformers design. A reliability of the method was experimentally verified by simultaneous measurement of a piezoelectric unimorph by three different techniques and results are presented in the chapter 4.2. Namely it was laser interferometry with lock-in amplifier, commercial laser vibrometer and the developed holographic method. It was proofed that all the methods provide comparable results and the difference is in the 5 % interval.

Some results in the chapter 4.3 were obtained during an investigation of a semi-active noise control by active elasticity control of piezoelectric actuators. A characteristic feature of the measurement is its large dynamic range (when the control is on and off) and large number of performed measurements (different setting of the control circuit).

As I already mentioned in the chapter “Motivation,” trends of development in measurement techniques (either my personal or as a LOM) are mainly influenced

by requirements of applied research. That is why I put effort into improvement of the time average digital holography in the described way, however, I have not exhausted all the potential hidden in the PFMTADH. Within scope of this dissertation I only dealt with harmonically oscillating objects. In some papers from the very beginning of holographic interferometry authors indicate, that frequency modulation can also be used for analysis of non-harmonic vibrations [73]. Moreover, I have omitted amplitude modulation (for my purpose useless) [74], easily accomplished by the Bragg cells. Phase modulation was also used for phase of vibration measurement [75]. All this ways open some new opportunities for further improvement of the method.

Reference

[1] R. A. Collacott, *Mechanical Vibrations: Their Calculation, Measurement, Effects and Suppression*. I. Pitman, 1947.

[2] K. G. McConnell and P. S. Varoto, *Vibration testing: theory and practice*. John Wiley & Sons, 1995.

[3] J. N. Butters and J. A. Leendertz, "Holographic and Video Techniques Applied to Engineering Measurement," *Measurement and Control*, vol. 4, no. 12, pp. 349–354, Dec. 1971.

[4] A. Macovski, S. D. Ramsey, and L. F. Schaefer, "Time-Lapse Interferometry and Contouring Using Television Systems," *Applied Optics*, vol. 10, no. 12, p. 2722, Dec. 1971.

[5] D. Gabor, "A new microscopic principle," *Nature*, vol. 161, no. 4098, pp. 777–778, 1948.

[6] E. N. Leith and J. Upatnieks, "Wavefront Reconstruction with Diffused Illumination and Three-Dimensional Objects," *Journal of the Optical Society of America*, vol. 54, no. 11, p. 1295, Nov. 1964.

[7] Y. N. Denisyuk, "Photographic Reconstruction of the Optical Properties of an Object in Its Own Scattered Radiation Field," *Soviet Physics Doklady*, vol. 7, p. 543, Dec. 1962.

[8] A. W. Lohmann and D. P. Paris, "Binary Fraunhofer Holograms, Generated by Computer," *Applied Optics*, vol. 6, no. 10, p. 1739, Oct. 1967.

[9] W.-H. Lee, "Binary Synthetic Holograms," *Applied Optics*, vol. 13, no. 7, p. 1677, Jul. 1974.

[10] W. H. Lee, "Sampled Fourier Transform Hologram Generated by Computer," *Applied Optics*, vol. 9, no. 3, p. 639, Mar. 1970.

[11] J. F. Heanue, M. C. Bashaw, and L. Hesselink, "Volume holographic storage and retrieval of digital data," *Science*, vol. 265, no. 5173, pp. 749–752, Aug. 1994.

[12] R. L. Powell and K. A. Stetson, "Interferometric Vibration Analysis by Wavefront Reconstruction," *Journal of the Optical Society of America*, vol. 55, no. 12, p. 1593, Dec. 1965.

[13] K. A. Stetson and R. L. Powell, "Interferometric Hologram Evaluation and Real-Time Vibration Analysis of Diffuse Objects," *Journal of the Optical Society of America*, vol. 55, no. 12, p. 1694, Dec. 1965.

[14] R. E. Brooks, L. O. Heflinger, and R. F. Wuerker, "INTERFEROMETRY WITH A HOLOGRAPHICALLY RECONSTRUCTED COMPARISON BEAM," *Applied Physics Letters*, vol. 7, no. 9, pp. 248–249, Nov. 1965.

[15] K. A. Haines and B. P. Hildebrand, "Surface-Deformation Measurement Using the Wavefront Reconstruction Technique," *Applied Optics*, vol. 5, no. 4, p. 595, Apr. 1966.

[16] B. P. Hildebrand and K. A. Haines, "The generation of three-dimensional contour maps by wavefront reconstruction," *Physics Letters*, vol. 21, no. 4, pp. 422–423, Jun. 1966.

[17] L. O. Heflinger and R. F. Wuerker, "Holographic Contouring via Multifrequency Lasers," *Applied Physics Letters*, vol. 15, pp. 28–30, Jul. 1969.

[18] M. H. Horman, "An Application of Wavefront Reconstruction to Interferometry," *Applied Optics*, vol. 4, no. 3, p. 333, Mar. 1965.

[19] D. W. Sweeney and C. M. Vest, "Reconstruction of Three-Dimensional Refractive Index Fields from Multidirectional Interferometric Data," *Applied Optics*, vol. 12, no. 11, p. 2649, Nov. 1973.

[20] I. H. Lira and C. M. Vest, "Refraction correction in holographic interferometry and tomography of transparent objects," *Applied optics*, vol. 26, no. 18, pp. 3919–3928, 1987.

[21] J. W. Goodman, "<title>Digital Image Formation From Electronically Detected Holograms</title>," 1967, pp. 176–181.

[22] M.A. Kronrod, L.P. Yaroslavsky, and N.S. Merzlyakov, "Reconstruction of holograms with a computer," *Soviet Physics-Technical Physics*, vol. 17, no. 2, 1972.

[23] U. Schnars and W. Jüptner, "Direct recording of holograms by a CCD target and numerical reconstruction," *Applied Optics*, vol. 33, no. 2, p. 179, Jan. 1994.

[24] Y. Zou, G. Pedrini, and H. Tiziani, "Surface contouring in a video frame by changing the wavelength of a diode laser," *Opt. Eng*, vol. 35, no. 4, pp. 1074–1079, 1996.

[25] T. Kreis, *Handbook of holographic interferometry: optical and digital methods. 2005.* Weinheim: Wiley-VCH. xii.

[26] U. Schnars and W. Jueptner, *Digital holography: digital hologram recording, numerical reconstruction, and related techniques*. Springer, 2004.

[27] M. K. Kim, "Principles and techniques of digital holographic microscopy," *Journal of Photonics for Energy*, p. 018005, Apr. 2010.

[28] J. Garcia-Sucerquia, W. Xu, S. K. Jericho, P. Klages, M. H. Jericho, and H. J. Kreuzer, "Digital in-line holographic microscopy," *Applied optics*, vol. 45, no. 5, pp. 836–850, 2006.

[29] Y. Takaki and H. Ohzu, "Fast Numerical Reconstruction Technique for High-Resolution Hybrid Holographic Microscopy," *Applied Optics*, vol. 38, no. 11, p. 2204, Apr. 1999.

[30] F. Dubois, L. Joannes, and J.-C. Legros, "Improved Three-Dimensional Imaging with a Digital Holography Microscope With a Source of Partial Spatial Coherence," *Applied Optics*, vol. 38, no. 34, p. 7085, Dec. 1999.

[31] J. W. Goodman, "Temporal Filtering Properties of Holograms," *Applied Optics*, vol. 6, no. 5, p. 857, May 1967.

[32] C. C. Aleksoff, "Temporally modulated holography," *Applied Optics*, vol. 10, no. 6, pp. 1329–1341, 1971.

[33] M. Ueda, S. Miida, and T. Sato, "Signal-to-noise ratio and smallest detectable vibration amplitude in frequency-translated holography: an analysis," *Applied Optics*, vol. 15, no. 11, pp. 2690–2694, 1976.

[34] P. Picart, J. Leval, D. Mounier, and S. Gougeon, "Time-averaged digital holography," *Opt. Lett.*, vol. 28, no. 20, pp. 1900–1902, Oct. 2003.

[35] F. L. Clerc, L. Collot, and M. Gross, "Numerical heterodyne holography with two-dimensional photodetector arrays," *arXiv:1112.5080 [physics]*, Dec. 2011.

[36] F. Joud, F. Laloë, M. Atlan, J. Hare, and M. Gross, "Imaging a vibrating object by Sideband Digital Holography," *Optics Express*, vol. 17, no. 4, p. 2774, Feb. 2009.

[37] P. Psota, V. Lédl, R. Doleček, J. Erhart, and V. Kopecký, "Measurement of piezoelectric transformer vibrations by digital holography," *IEEE Transactions on Ultrasonics, Ferroelectrics and Frequency Control*, vol. 59, no. 9, pp. 1962–1968, Sep. 2012.

[38] Lédl, P. Psota, R. Doleček, T. Vít, and J. Václavík, "Testing of a Recently Developed Digital Holographic Method for very Small Amplitude Measurements," 2013.

[39] N. Verrier and M. Atlan, "Absolute measurement of small-amplitude vibrations by time-averaged heterodyne holography with a dual local oscillator," *Opt Lett*, vol. 38, no. 5, pp. 739–741, Mar. 2013.

[40] D. N. Borza, "Mechanical vibration measurement by high-resolution time-averaged digital holography," *Measurement Science and Technology*, vol. 16, no. 9, p. 1853, 2005.

[41] C. S. Vikram, "A scheme for quantitative holographic vibration analysis from reconstructed irradiance data," *Journal of Modern Optics*, vol. 39, no. 10, pp. 1987–1989, 1992.

[42] P. Psota, V. Lédl, and R. Doleček, "High Dynamic Range Digital Holographic Method for Very Small Amplitude Measurement," in *Fringe 2013*, Springer, 2014, pp. 635–640.

[43] P. Psota, V. Lédl, R. Doleček, J. Václavík, and V. Kopecký, "Improved holographic method for vibration amplitude measurement from nano to microscale," in *11TH INTERNATIONAL CONFERENCE ON VIBRATION MEASUREMENTS BY LASER AND NONCONTACT TECHNIQUES-AIVELA 2014: Advances and Applications*, 2014, vol. 1600, pp. 228–236.

[44] K. A. Stetson and W. R. Brohinsky, "Fringe-shifting technique for numerical analysis of time-average holograms of vibrating objects," *J. Opt. Soc. Am. A*, vol. 5, no. 9, pp. 1472–1476, Sep. 1988.

[45] P. Psota, V. Lédl, P. Vojtíšek, J. Václavík, R. Doleček, and P. Mokrý, "Advanced time average holographic method for measurement in extensive vibration amplitude range with quantitative single-pixel analysis," 2015, vol. 9508, p. 95080N–95080N–9.

[46] J. Erhart, P. Pulpán, R. Doleček, P. Psota, and V. Lédl, "Disc piezoelectric ceramic transformers," *Ultrasonics, Ferroelectrics, and Frequency Control, IEEE Transactions on*, vol. 60, no. 8, pp. 1612–1618, 2013.

[47] J. Erhart, P. Pulpán, R. Doleček, P. Psota, and V. Lédl, "Disc piezoelectric ceramic transformers," in *Applications of Ferroelectrics held jointly with 2012 European Conference on the Applications of Polar Dielectrics and 2012 International Symp Piezoresponse Force Microscopy and Nanoscale Phenomena in Polar Materials (ISAF/ECAPD/PFM), 2012 Intl Symp*, 2012, pp. 1–4.

[48] V. Lédl, P. Psota, R. Doleček, J. Erhart, and V. Kopecký, "A digital holographic method for the measurement of piezoelectric transformer vibrations," in *Applications of Ferroelectrics (ISAF/PFM), 2011 International Symposium on and 2011 International Symposium on Piezoresponse Force Microscopy and Nanoscale Phenomena in Polar Materials*, 2011, pp. 1–4.

[49] P. Psota, V. Kopecký, V. Lédl, and R. Doleček, "Digital Holographic Method for Piezoelectric Transformers Vibration Analysis," *EPJ Web of Conferences*, vol. 48, p. 00021, 2013.

[50] P. Psota, V. Kopecký, R. Doleček, and V. Lédl, "Digital Holographic Method for Piezoelectric Transformers Vibration Analysis," in *Optics and Measurement International Conference Proceedings*, Liberec, 2012.

[51] P. Mokrý, P. Psota, K. Steiger, J. Václavík, R. Doleček, V. Lédl, and M. Šulc, "Noise suppression in curved glass shells using macro-fiber-composite actuators studied by the means of digital holography and acoustic measurements," *AIP Advances*, vol. 5, no. 2, p. 027132, Feb. 2015.

[52] P. Mokrý, K. Steiger, J. Václavík, P. Psota, R. Doleček, P. Martón, M. Kodejška, and others, "Noise shielding using active acoustic metamaterials with electronically tunable acoustic impedance."

[53] K. Nováková, P. Psota, R. Doleček, V. Lédl, P. Mokry, J. Václavík, P. Martón, and M. Černík, "Planar acoustic metamaterials with the active control of acoustic impedance using a piezoelectric composite actuator," in *Applications of Ferroelectric and Workshop on the Piezoresponse Force Microscopy (ISAF/PFM), 2013 IEEE International Symposium on the*, 2013, pp. 317–320.

[54] P. Mokrý, K. Steiger, J. Václavík, P. Psota, R. Doleček, P. Márton, M. Kodejška, and M. Černík, "Noise shielding using active acoustic metamaterials with electronically tunable acoustic impedance," in *INTERNOISE2014 Proceedings*, Melbourne, AUSTRALIA, 2014, pp. 1–9.

[55] P. Psota, V. Lédl, R. Doleček, P. Mokrý, and V. Kopecký, "Measurement of vibration mode structure for adaptive vibration suppression system by digital holography," in *Applications of Ferroelectric and Workshop on the Piezoresponse Force Microscopy (ISAF/PFM), 2013 IEEE International Symposium on the*, 2013, pp. 214–217.

[56] "Wiley: Fundamentals of Photonics, 2nd Edition - Bahaa E. A. Saleh, Malvin Carl Teich." [Online]. Available: http://eu.wiley.com/WileyCDA/WileyTitle/productCd-0471358320.html. [Accessed: 23-Nov-2015].

[57] Max Born & Emil Wolf, *Principles of Optics*. .

[58] J. W. Goodman, *Introduction to Fourier optics*, vol. 2. McGraw-hill New York, 1968.

[59] P. Hariharan, *Optical Holography: Principles, Techniques and Applications*. Cambridge University Press, 1996.

[60] G. Saxby, *Practical holography*. Taylor & Francis, 2003.

[61] T. Kreis, "Recent Advances in Holographic Strain and Stress Measurement," in *Imaging Methods for Novel Materials and Challenging Applications, Volume 3*, H. Jin, C. Sciammarella, C. Furlong, and S. Yoshida, Eds. New York, NY: Springer New York, 2013, pp. 17–27.

[62] P. K. Rastogi, *Holographic Interferometry: Principles and Methods*. Springer, 2013.

[63] E. Cuche, P. Marquet, and C. Depeursinge, "Spatial Filtering for Zero-Order and Twin-Image Elimination in Digital Off-Axis Holography," *Appl. Opt.*, vol. 39, no. 23, pp. 4070–4075, Aug. 2000.

[64] I. Yamaguchi, "Phase-Shifting Digital Holography," in *Digital Holography and Three-Dimensional Display*, Springer US, 2006, pp. 145–171.

[65] M. Abramowitz and I. A. Stegun, Eds., *Handbook of Mathematical Functions: with Formulas, Graphs, and Mathematical Tables*, 0009-Revised edition. New York: Dover Publications, 1965.

[66] D. N. Borza, "Full-field vibration amplitude recovery from high-resolution time-averaged speckle interferograms and digital holograms by regional inverting of the Bessel function," *Optics and Lasers in Engineering*, no. 8, pp. 747–770, 2006.

[67] D. Malacara, *Optical shop testing*, vol. 59. Wiley-Interscience, 2007.

[68] *Interferogram Analysis For Optical Testing, Second Edition*, 2 edition. Boca Raton, FL: CRC Press, 2005.

[69] P. J. de Groot and L. L. Deck, "New algorithms and error analysis for sinusoidal phase shifting interferometry," 2008, vol. 7063, p. 70630K–70630K–14.

[70] ISO/IEC Guide 98-3:2008, "Uncertainty of measurement - Part 3: Guide to the expression of uncertainty in measurement (GUM:1995)." 2008.

[71] V. Lédl, P. Psota, R. Doleček, J. Erhart, and V. Kopecký, "A digital holographic method for the measurement of piezoelectric transformer vibrations," in *Applications of Ferroelectrics (ISAF/PFM), 2011 International Symposium on and 2011 International Symposium on Piezoresponse Force Microscopy and Nanoscale Phenomena in Polar Materials*, 2011, pp. 1 –4.

[72] P. Psota, V. Lédl, R. Doleček, J. Václavík, and M. Šulc, "Comparison of digital holographic method for very small amplitudes measurement with single point laser interferometer and laser doppler vibrometer," in *Digital Holography and Three-Dimensional Imaging*, 2012, p. DSu5B–3.

[73] P. C. Gupta and K. Singh, "Holographic interferometry of non-sinusoidal vibrations," *Opto-electronics*, vol. 6, no. 4, pp. 305–311, Jul. 1974.

[74] N. Takai, M. Yamada, and T. Idogawa, "Holographic interferometry using a reference wave with a sinusoidally modulated amplitude," *Optics & Laser Technology*, vol. 8, no. 1, pp. 21–23, Feb. 1976.

[75] D. B. Neumann, C. F. Jacobson, and G. M. Brown, "Holographic technique for determining the phase of vibrating objects," *Appl Opt*, vol. 9, no. 6, pp. 1357–1362, Jun. 1970.

Author's list of publications

[1] P. Psota, V. Lédl, P. Vojtíšek, R. Doleček, and and P. Mokrý, "Advanced time average holographic method for measurement in extensive vibration amplitude range with quantitative single-pixel analysis," in SPIE Optics+ Optoelectronics, 2015, p. 95080N–95080N. *(1st place – Best Student Paper Award)*

[2] P. Psota, V. Lédl, P. Vojtíšek, R. Doleček, and V. Kopecký, "3D form inspection of grinded optical surfaces by digital holography," in Optics and Measurement Conference 2014, 2015, pp. 944218–944218. *(2nd place – Best Student Paper Award)*

[3] P. Mokrý, P. Psota, K. Steiger, J. Václavík, R. Doleček, V. Lédl, and M. Šulc, "Noise suppression in curved glass shells using macro-fiber-composite actuators studied by

the means of digital holography and acoustic measurements," AIP Advances, vol. 5, no. 2, p. 027132, 2015.

[4] P. Mokry, K. Steiger, P. Psota, R. Doleček, P. Vojtisek, and V. Lédl, "Digital holographic interferometry as an experimental instrumentation for measurements of macroscopic properties of polydomain ferroelectrics," in Optics and Measurement Conference 2014, 2015, p. 94420V–94420V.

[5] V. Lédl, P. Psota, P. Vojtíšek, R. Doleček, P. Mokrý, and M. Dlask, "Challenges in holographic measurement of aspheric and freeform optical components shape," in SPIE Optics+ Optoelectronics, 2015, p. 95080M–95080M.

[6] V. Lédl, P. Psota, P. Vojtíšek, R. Doleček, and P. Mokrý, "Holographic contouring and its limitations in nearly specularly reflecting surface measurement," in Optics and Measurement Conference 2014, 2015, p. 94420Q–94420Q.

[7] V. Lédl, P. Psota, R. Doleček, and T. Vít, "Digital holographic setups for phase object measurements in micro and macro scale," EPJ Web of Conferences, vol. 92, p. 01001, 2015.

[8] R. Doleček, P. Psota, V. Lédl, T. Vít, P. Dančová, and V. Kopecký, "Comparison of digital holographic interferometry and constant temperature anemometry for measurement of temperature field in fluid," in SPIE Optics+ Optoelectronics, 2015, p. 95080P–95080P.

[9] P. Psota, V. Lédl, R. Doleček, J. Václavík, and V. Kopecký, "Improved holographic method for vibration amplitude measurement from nano to microscale," in 11TH INTERNATIONAL CONFERENCE ON VIBRATION MEASUREMENTS BY LASER AND NONCONTACT TECHNIQUES-AIVELA 2014: Advances and Applications, 2014, vol. 1600, pp. 228–236.

[10] P. Psota, V. Lédl, and R. Doleček, "High Dynamic Range Digital Holographic Method for Very Small Amplitude Measurement," in Fringe 2013, Springer, 2014, pp. 635–640.

[11] V. Lédl, P. Psota, T. Vít, and R. Doleček, "Digital Holographic Setup for Measurement of Fast Developing Phenomenon in Wide Area," in Fringe 2013, Springer, 2014, pp. 577–580.

[12] R. Doleček, P. Psota, V. Lédl, T. Vít, and V. Kopecký, "Comparison of holographic setups used in heat and mass transfer measurement," EPJ Web of Conferences, vol. 67, p. 02021, 2014.

[13] T. Vít, V. Lédl, R. Doleček, and P. Psota, "The Possibility of Visualizing Temperature Fields Using Digital Holographic Interferometry," in Applied Mechanics and Materials, 2013, vol. 284, pp. 988–995.

[14] J. Vaclavík, R. Doleček, V. Lédl, and P. Psota, "Experimental study on SPDT machining of Gallium Phosphide," in SPIE Optifab, 2013, p. 88842H–88842H.

[15] P. Psota, V. Lédl, R. Doleček, P. Mokry, and V. Kopecký, "Measurement of vibration mode structure for adaptive vibration suppression system by digital holography," in Applications of Ferroelectric and Workshop on the Piezoresponse Force Microscopy (ISAF/PFM), 2013 IEEE International Symposium on the, 2013, pp. 214–217.

[16] P. Psota, V. Lédl, R. Doleček, and V. Kopecký, "Holographic Nano-scale Amplitude Measurement Method with Expanded Dynamic Range," in Digital Holography and Three-Dimensional Imaging, 2013, p. DTh5A–1.

[17] P. Psota, V. Kopecký, V. Lédl, and R. Doleček, "Digital Holographic Method for Piezoelectric Transformers Vibration Analysis," EPJ Web of Conferences, vol. 48, p. 00021, 2013.

[18] K. Nováková, P. Psota, R. Doleček, V. Lédl, P. Mokrý, J. Václavík, P. Martón, and M. Černík, "Planar acoustic metamaterials with the active control of acoustic impedance using a piezoelectric composite actuator," in Applications of Ferroelectric and Workshop on the Piezoresponse Force Microscopy (ISAF/PFM), 2013 IEEE International Symposium on the, 2013, pp. 317–320.

[19] R. Melich, P. Psota, V. Lédl, and J. Václavík, "Irregular surfaces-measurements and ZEMAX simulations," EPJ Web of Conferences, vol. 48, p. 00015, 2013.

[20] V. Lédl, P. Psota, J. Václavík, R. Doleček, and P. Vojtíšek, "Multiwavelength digital holography for polishing tool shape measurement," in SPIE Optifab, 2013, p. 88840E–88840E.

[21] J. Erhart, P. Pulpán, R. Doleček, P. Psota, and V. Lédl, "Disc piezoelectric ceramic transformers," Ultrasonics, Ferroelectrics, and Frequency Control, IEEE Transactions on, vol. 60, no. 8, pp. 1612–1618, 2013.

[22] R. Doleček, P. Psota, V. Lédl, T. Vít, J. Václavík, and V. Kopecký, "General temperature field measurement by digital holography," Applied optics, vol. 52, no. 1, pp. A319–A325, 2013.

[23] R. Doleček, V. Kopecký, P. Psota, and V. Lédl, "Digital Holographic setup for Measurement of Asymmetric Temperature Field and Tomographic Reconstruction," EPJ Web of Conferences, vol. 48, p. 00003, 2013.

[24] P. Psota, V. Lédl, R. Doleček, J. Václavík, and M. Šulc, "Comparison of digital holographic method for very small amplitudes measurement with single point laser interferometer and laser doppler vibrometer," in Digital Holography and Three-Dimensional Imaging, 2012, p. DSu5B–3.

[25] P. Psota, V. Lédl, R. Doleček, J. Erhart, and V. Kopecký, "Measurement of piezoelectric transformer vibrations by digital holography," Ultrasonics, Ferroelectrics, and Frequency Control, IEEE Transactions on, vol. 59, no. 9, pp. 1962–1968, 2012.

[26] V. Lédl, T. Vít, R. Doleček, and P. Psota, "Digital holografic interferometry used for identification of 2D temperature field," EPJ Web of Conferences, vol. 25, p. 02014, 2012.

[27] R. Doleček, P. Psota, V. Lédl, T. Vít, J. Václavík, and V. Kopecký, "Measurement of Asymmetric Temperature Field by Using Digital Holographic Multidirectional Interferometry," in Digital Holography and Three-Dimensional Imaging, 2012, p. DSu5B–2.

[28] P. Dancova, T. Vít, Z. Travnicek, V. Lédl, and P. Psota, "Methods of measurement of the temperature field in pulsatile fluid," ICHMT DIGITAL LIBRARY ONLINE, 2012.

[29] P. Psota, V. Lédl, P. Vojtíšek, Device to measure shape of optical surfaces, especially diffusion-reflective surfaces, Utility model nr. 27893

[30] V. Lédl, P. Psota, P. Vojtíšek, and J. Křížek, Expanded measurement range interefometer, Utility model nr. 27615